Winter 2017

An Experimental Study of the Wake of a Turbulent Boundary Layer Junction Flow

Nicholas Marino
University of New Hampshire, Durham

AN EXPERIMENTAL STUDY OF THE WAKE OF A TURBULENT BOUNDARY LAYER JUNCTION FLOW

BY

NICHOLAS MARINO

B.S., Mechanical Engineering, University of New Hampshire, 2016

THESIS

Submitted to the University of New Hampshire

in Partial Fulfillment of

the Requirements for the Degree of

Masters of Science

in

Mechanical Engineering

December, 2017

This thesis has been examined and approved in partial fulfillment of the requirements for the degree of Masters of Science in Mechanical Engineering by:

Thesis Director, Joseph C. Klewicki

Professor of Mechanical Engineering

Christopher M. White

Associate Professor of Mechanical Engineering

Gregory P. Chini

Professor of Mechanical Engineering

Original approval signatures are on file with the University of New Hampshire Graduate School.

ACKNOWLEDGEMENTS

Without the help of my fellow graduate students and local industries, the following experiment could not have been set up and measurements obtained. I would like to thank Drummond Biles for his assistance and time in machining parts. I would like to thank MACY INDUSTRY for manufacturing the airfoil body. I would like to thank FORM 3D SOLUTIONS for making the fairing. Lastly, I would like to give a special thanks to Spencer Zimmerman for all of his time and work in developing his hot-wire probe and time spent performing experiments with me and processing the data gathered by him and myself of which without him none of the following measurements would have been possible.

TABLE OF CONTENTS

LIST OF TABLES

LIST OF FIGURES

NOMENCLATURE

u_τ ……...Friction Velocity

U_∞……..Freestream Velocity

δ…….Boundary Layer Thickness: also written as δ_{99} or boundary layer height

H ……Airfoil Height

T ……Airfoil Thickness

C ……Airfoil Cord Length

Re_θ…….Reynolds Number with respect to Momentum Thickness: non-dimensional scaling parameter, ratio between inertia forces and viscous forces, in terms of Momentum Thickness

ρ…….Density

v…….Kinematic Viscosity

δ^*……Displacement Thickness: the distance by which the external potential flow is displaced outwards due to the decrease in velocity in the boundary layer

θ…….Momentum Thickness: the distance by which the boundary should be displaced to compensate for the reduction in momentum on account of the boundary layer formation

τ_w……...Wall Shear Stress

d …… Outer Diameter of Preston Tube

Δp_p…….Pressure Difference: difference between Preston tube pressure and static pressure

TKE ……Turbulent Kinetic Energy: root mean square (rms) velocity fluctuations

E ……Enstrophy: the square of vorticity

ABSTRACT

AN EXPERIMENTAL STUDY OF THE WAKE OF A TURBULENT BOUNDARY LAYER JUNCTION FLOW

by

Nicholas Marino

University of New Hampshire, December, 2017

An experimental study of the wake of a turbulent boundary layer junction flow was performed using a 3:2 elliptical nose and NACA 0020 tail airfoil in the Flow Physics Facility at the University of New Hampshire. An eight-wire enstrophy hot-wire probe was used to measure all three components of velocity and vorticity at four downstream measurement planes from 1 cord length to 33 cord lengths behind the airfoil. In addition, a simple fairing was added to the airfoil, and the same experiments were repeated. The friction velocity was measured afterward by a Preston tube experiment at the same measurement locations. The incoming flow had a momentum thickness Reynolds number of $\mathrm{Re}_\theta = 19600$.

It was found that the streamwise velocity statistics in the near measurement planes matched previous junction flow observations. The other velocity statistics supported the conclusions and knowledge in the near planes. The vorticity variance measurements showed little variation from the undisturbed boundary layer leading to the conclusion that large-scale motions are primarily responsible for the non-equilibrium aspects of the flow. The downstream

measurements clarified the recovery process towards the undisturbed boundary layer. The final measurement plane showed that aspects of the flow had fully recovered, while others had not. The Reynold stress showed that the turbulent structure of the flow had not recovered but remained persistently different from the undisturbed case. The airfoil with the fairing supported the observations of the airfoil case. Differences were seen between the airfoil and the airfoil with the fairing, but due to the coarse measurement plane, no conclusions were made.

CHAPTER 1: INTRODUCTION

1.1 Overview

In 1904, Prandlt [1] introduced his boundary layer theory describing the interaction of a viscous fluid with a solid boundary. He stated that the effect of friction from the solid boundary on the fluid caused the fluid adjacent to the solid boundary to stick to it; this describes his no-slip condition. He continued in saying that the frictional effects were only experienced in a thin region, the boundary layer, near the solid boundary while the remainder of the flow was effectively inviscid and unaffected by the presence of the wall. As the Reynolds number increases, the boundary layer transitions from a laminar flow to a turbulent flow. As the Reynolds number continues to increase in the turbulent regime, the statistical properties of the wall-flows continue to vary and the underlying instantaneous mechanism of momentum and energy transfer change accordingly. Many practical applications, including US Navy vehicles, operate within the high Reynolds number turbulent regime, and therefore, a considerable amount of research has been performed studying wall-bounded flows with most effort devoted to the so-called canonical wall flows. These flows include fully developed pipe flow and channel flow, along with the zero-pressure gradient boundary layer. Central aspects of our understanding of these flows pertain to the dependence of their statistics and spectral properties on Reynolds

number [2]. Much less is known regarding the so-called non-equilibrium wall flows and their dynamical structure.

Non-equilibrium flows arise when an imposed forcing effect modifies the unperturbed canonical flow in such a way that the local momentum transport and turbulent properties lose connection with the local wall shear stress. Broadly speaking, forcing effects of interest include heterogeneous surface roughness, streamwise pressure gradients, and imposed lateral strain rates. Such perturbations are commonplace in many naval vessels and aircraft applications, see figure 1.1.1. The present study focuses on turbulent boundary layer junction flow. Here lateral strain rates caused by an airfoil drive a canonical boundary layer flow into a non-equilibrium state.

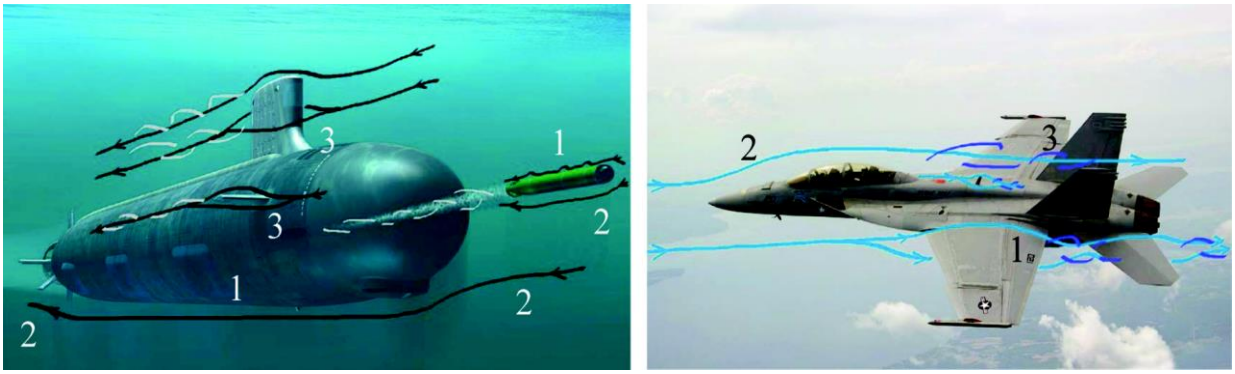

Figure 1.1.1: High Reynolds number non-equilibrium flow phenomena: 1. Heterogenous roughness. 2. Stream-wise pressure gradients. 3. Junction Flows (a) Virginia class submarine, (b) F/A-18E Super Hornet.

1.2 Turbulent Boundary Layer Junction Flow

Junction flows occur when the incoming boundary layer encounters another object normal to the surface upon which the boundary layer is developing. The presence of the object creates an adverse pressure gradient experienced by the approaching flow, and this causes the incoming boundary layer to separate fore of the protruding body. (The coordinate system used going forward will consider the positive x-direction the streamwise direction. The y-direction will be the wall-normal direction with the origin at the wall. The z-direction will be the spanwise

direction in which zero will be the centerline of the tunnel and airfoil. Positive z is to the right looking in the positive x-direction.) The spanwise pressure gradient then causes the fluid to move around the object while simultaneously the spanwise vorticity is stretched along the object. In the case of a streamlined body, the skewing and stretching around the body is greater causing larger lateral strain rates. The flow then advects these effects downstream creating a horseshoe-like shape [4]. Figure 1.2.1 from Fleming shows this process and the aptly named horseshoe vortex. The horseshoe vortex has been an important aspect of aerodynamics dating back to Prandtl's

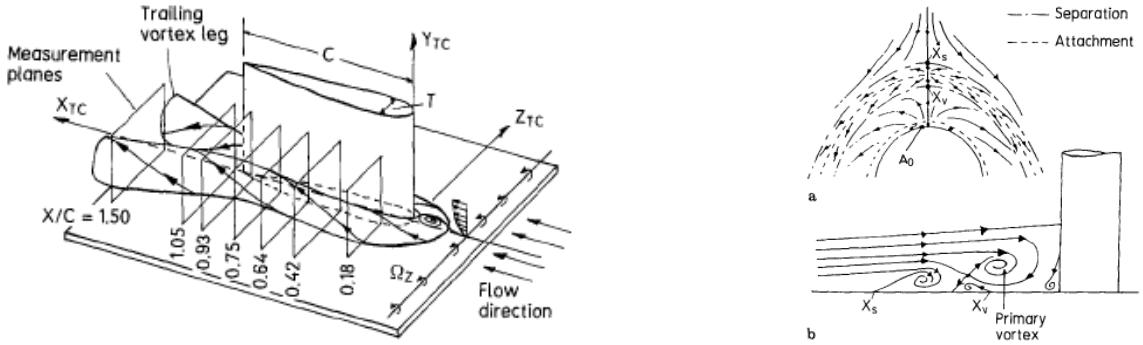

Figure 1.2.1: Turbulent Junction Flow Wing Body Visualization [3]

lifting line theory for a finite wing. He replaced the finite wing with a bound vortex filament, however, because of Helmholtz's theorem a vortex filament cannot end in a fluid. Therefore, the two vortices trail from the wing tips to infinity creating the horseshoe-like shape [5].

The horseshoe vortex in a junction flow has the same rotation as the incoming boundary layer and therefore takes the high-speed freestream flow and brings it close to the wall which causes an increase in heat transfer and drag. One such example is the scouring around bridge piers due to the presence of a horseshoe vortex. Similarly, the wing-fuselage junctions on modern-day aircraft cause about 10% of the total drag. This can also lead to buffet impairing the aerodynamic performance of the aircraft [6]. These areas are of high interest to engineers leading to the need to understand the physics involved in such flows. This has been a topic of research

over the last couple decades with attempts to fully understand the flow as well find ways to mitigate undesirable effects.

1.3 Literature Review

There have been numerous studies of turbulent junction flows. These studies have primarily been performed using simple geometric shapes such as cylinders, as well as more complex geometries including various airfoil configurations. Dickinson in 1986 presented a junction flow study with a NACA 0020 airfoil and the so-called Rood airfoil. He found that the Rood airfoil produces larger crossflow velocities due to the more blunt nose allowing the trailing horseshoe vortex to be identified more easily. The Rood airfoil combines a NACA 0020 tail with a 3:2 elliptical nose and has become a standard test case [7]. Gand et al. [6] list various experiments performed as well as what was of interest in each study including whether the horseshoe vortex and corner separation were observed. The Reynolds number with respect to the moment thickness, Re_θ, was also given for each experiment. Momentum thickness is the distance by which the boundary layer should be displaced to compensate for the reduction in the momentum of the fluid on account of the boundary layer. The largest Reynolds number in the list of experiments was $\mathrm{Re}_\theta = 8200$. They then performed some modeling looking at the corner separation. More recently, a large eddy simulation was performed by Ryu et al. [8] at a $\mathrm{Re}_\theta = 5940$ and they compared their results to the experiments performed by Simpsons, Olcmen, Fleming, and Devenport. These studies have incoming boundary layer Reynolds numbers up to $\mathrm{Re}_\theta = 8200$ and are focused on the flow around the object to the trailing edge separation.

Simpson, Olcmen, and Fleming [9] performed one of the most comprehensive experimental studies. Through their combined experiments they gathered data from incoming boundary layers with Reynolds numbers of $500 < \mathrm{Re}_\theta < 23000$ for a Rood airfoil. Some

examples of the perturbations from the airfoils are shown in table 1.3.1. The body height, maximum thickness, and incoming boundary layer height are presented. The perturbation effect is related to the airfoil height compared to boundary layer height. Therefore, the ratio of the boundary layer height to airfoil height is computed. The ratio of the maximum thickness to the airfoil height is also given. This data has been used to understand the physics of the flow and compare observations to numerical models. The primary focus of these studies was the nose separated region and the junction vortex around the side of the airfoil as well as comparing the effects of different in-flow boundary layers [9].

Table 1.3.1: Airfoil Perturbation					
Re_θ	H	T	δ	δ/H	T/H
5940 [9]	22.9	7.17	3.91	0.170742	0.3131
23200 [9]	22.9	7.17	13.42	0.586026	0.3131
6300 [7]	22.9	7.17	3.68	0.160699	0.3131

Fleming et al. [7] compared the findings of previous work with their own. In addition, they focused on the downstream wake development. This is of particular interest because to the author's knowledge they compiled the farthest downstream wake measurements in the literature. Measurements of this study where aquired with an incoming boundary layer of $Re_\theta = 6300$. They were taken along the spanwise extent of the body, and out to 11.56 cord lengths downstream. The wake entered an adverse pressure gradient six cord lengths downstream of the body. Only the streamwise mean velocity and velocity variance were measured starting at three cord lengths downstream. Owing to its relevance, this study will be referenced throughout this thesis.

Devenport et al. [10] investigated how the addition of a simple fairing affects the flow around a Rood airfoil. Their fairing was a simple fillet with a radius equal to 0.53 of the wing

thickness wrapped circumferentially around the airfoil. They found that the fillet does not eliminate the separation at the leading-edge but increases the effective radius of the nose.

The studies just discussed provide great insight into turbulent boundary layer junction flows and generated a wide range of data to compare to numerical models. However, there is still a need for continued research to provide experimental data to validate models and gain a greater understanding of the underlying physics. The present study builds on this previous work. The incoming boundary layer has a Reynolds number $\mathrm{Re}_\theta = 19600$, and wake measurements were then taken out to 33 cord lengths downstream the body. To the author's knowledge, this provides the most extensive documentation of the Rood body wake to date. In addition, a custom-made eight-wire enstrophy sensor was used to acquire wake statistics for all three velocity components. The present study will also look at a simple fairing case to compare with Devenport et al. [10].

1.4 Aims of the Present Study

The current study uses a Rood airfoil with a removable fairing to compare to previous studies. The experiments were performed in the University of New Hampshire Flow Physics Facility (described in detail in the next section) which allowed for wake measurements out to 33 cord lengths behind the body giving the furthermost wake study done for turbulent junction flows. An eight-wire enstrophy sensor was used to measure the three components of the mean and fluctuating velocity including the Reynolds stress and other velocity correlations. In addition, the three components of time-resolved vorticity were measured. The vorticity measurements were, however, only obtained in the first two measurement planes for the airfoil and the first measurement plane for the airfoil with the fairing. The combination of the long fetch afforded by the FPF and measurements by the enstrophy probe give the most comprehensive study to date of the downstream wake of a turbulent boundary layer Rood airfoil junction flow.

This study focuses on the similarities of the near wake to measurements from previous similar experiments as well as the downstream development of the velocity statistics. Profiles are plotted for each statistic for the given spanwise measurement location as well as the downstream location. These statistics include the mean velocities, variances of the fluctuations, turbulent shear stress, and turbulence kinetic energy. Where vorticity measurements are available, their statistical behaviors will also be discussed. The downstream evolution of the power spectra of the three velocity components will be characterized relative to the unperturbed boundary layer. The airfoil with the fairing will then be compared to the airfoil without the fairing examining the differences in their statistics at the various downstream locations. Finally, downstream development of the Reynolds stress and velocity correlations will be discussed. For completeness, additional data plots are compiled in the appendix.

CHAPTER 2: EXPERIMENT

2.1 Facility

The turbulent boundary layer junction flow experiment was performed at the University of New Hampshire (UNH) Flow Physics Facility (FPF). The FPF is, to the author's knowledge, the largest boundary layer wind tunnel in the world. It measures approximately 2.8m in height (varies to maintain a zero-pressure gradient in the streamwise direction), 6m wide, and 72m in length. The tunnel is an open circuit pressure driven wind tunnel in which two 300kW fans create a lower pressure in the plenum at the rear of the tunnel to draw the atmospheric air in at the inlet and exits out through the fans (Figure 2.1.1). The flow enters at the left of figure 2.1.1 through a turbulence management section where the flow is tripped to be turbulent on the floor and walls and exits after the low-pressure plenum on the right of the figure. The large flow development fetch allows for high Reynolds number flows at low speeds in which the boundary

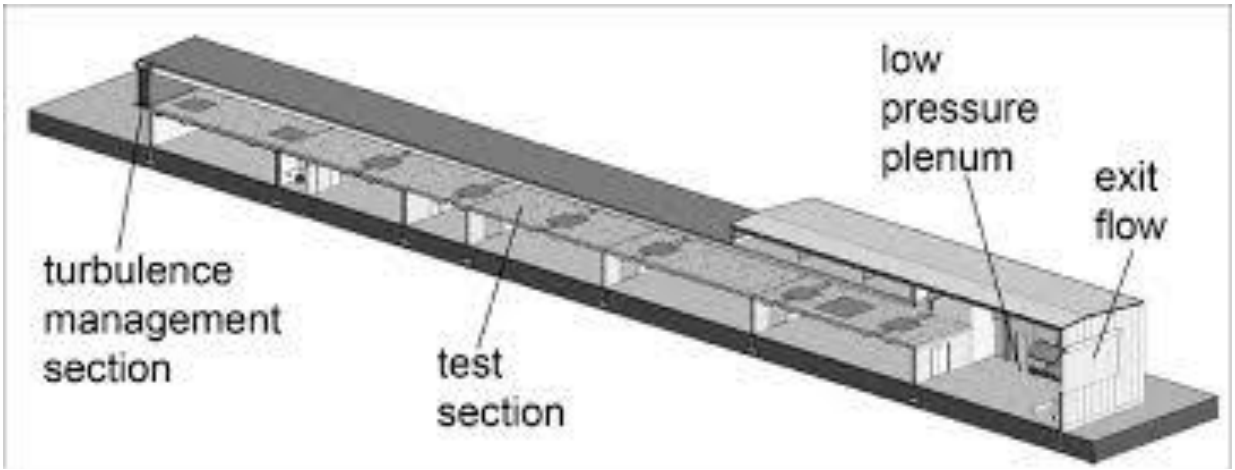

Figure 2.1.1: UNH Flow Physics Facility cut away [11]

layer height towards the rear of the tunnel can reach a δ_{99} of approximately one meter. Vincenti et al. [11] show the constancy of U_∞ as a function of downstream fetch with approximately a 3% increase in the last three meters for higher velocities and Preston tube-based friction velocity estimates in the spanwise direction with an overall variation of less than 0.5% across the span. For a comprehensive review of the FPF, see Vincenti et al [10].

2.2 Instrumentation

An eight-wire enstrophy sensor that simultaneously measures three components of velocity and three components of vorticity was used. Hot-wire sensors allow fluctuations in velocity and vorticity to be measured with good spatial and temporal resolution. The probe used was developed and implemented by S. Zimmerman at the University of Melbourne [12]. The

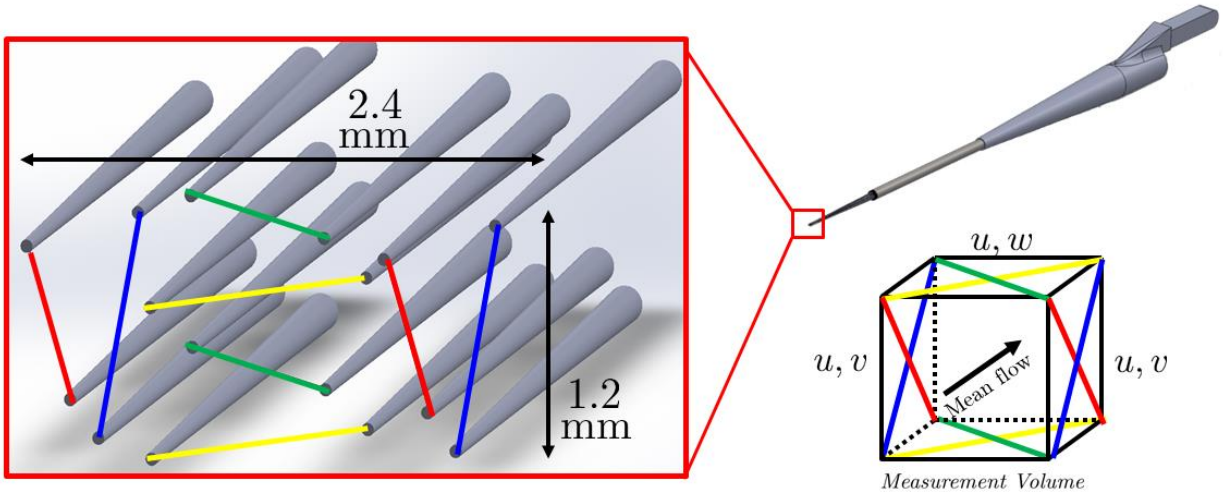

Figure 2.2.1: 8-wire enstrophy model showing wire design and where each component of velocity is measured

probe was tailored for boundary layer measurements at higher Reynolds number and was sufficiently tested. The probe is comprised of four x-wire arrays shown in Figure 2.2.1. Each wire was operated by the custom-built Melbourne University Constant Temperature Anemometer with the output routed through an Alligator Technologies USBPGF-S1 programmable analog low pass filter and then data acquired using a Data Translation DT9836

15-bit A/D board. The temperature was recorded along with each data point by a custom-built thermocouple, and the ambient pressure was recorded manually throughout the experiment. The probe has a size of less than ten viscous units for the measurements taken in the FPF. A viscous unit is defined by the kinematic viscosity, ν, and the friction velocity, u_τ. A single viscous unit is the smallest motion in the flow. Having a probe size on the order of less than ten viscous units allows for the resolution of the smaller motions of the flow. For a full review of the probe design, processing, and testing, see Zimmerman [12]. The combined small size of the probe and large size of the FPF afford the measurements presented in this study to be some of the highest

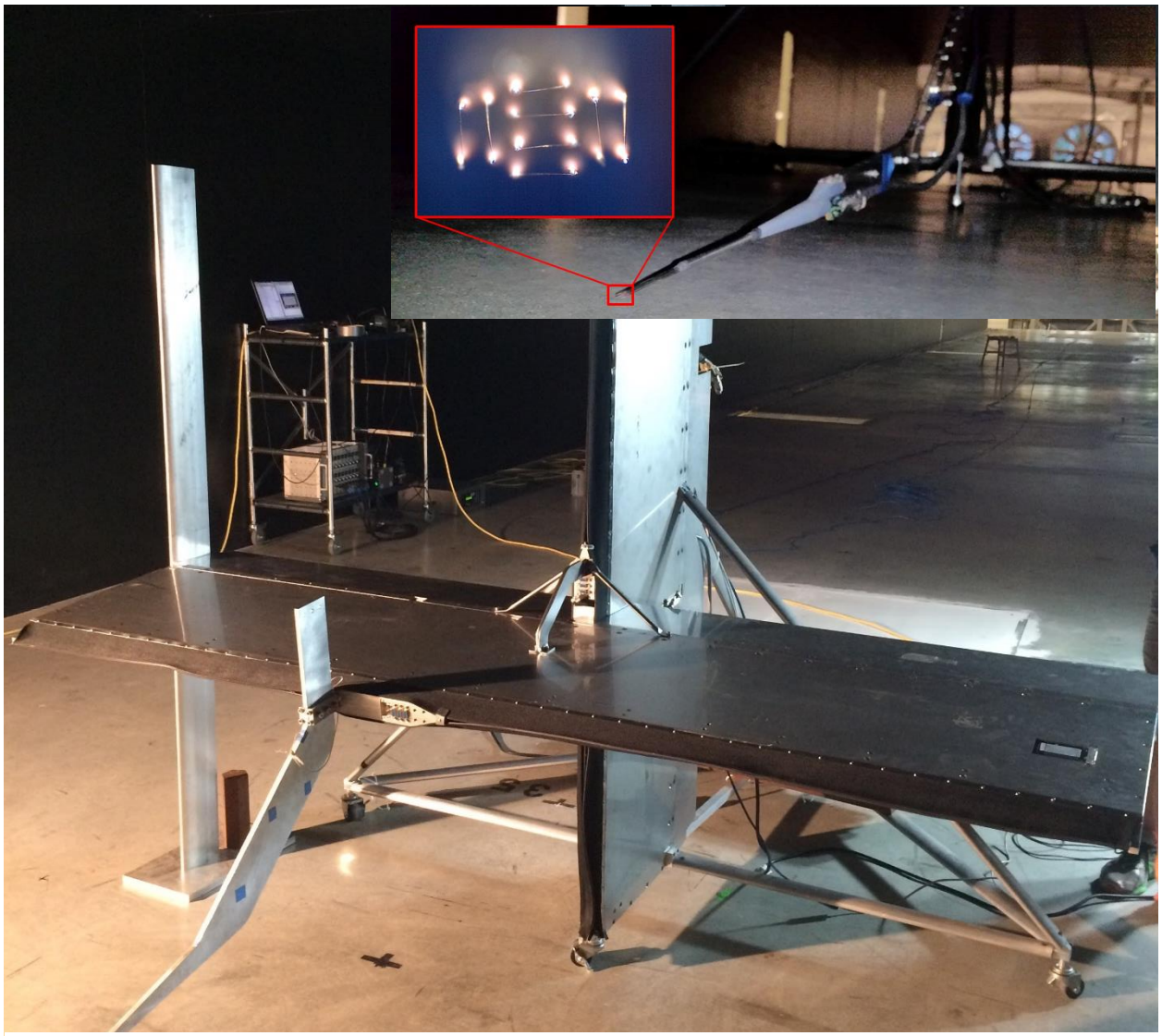

Figure 2.2.2: Custom built 2D traverse and mounted hot-wire probe in UNH FPF

resolution, highest Reynolds number measurements of vorticity fluctuations in existence. Unfortunately, the probe experienced a wire breakage, and therefore capabilities to measure the vorticity were lost after the second measurement location. The three components of velocity were maintained throughout the experiment allowing the measurement of the mean and fluctuating velocities along with the Reynolds stress and other velocity correlations.

The probe was mounted on a sting arm connected to a computer controlled custom built two-axis traverse shown in figure 2.2.2. This is the first experiment performed with the spanwise axis of the traverse. Modifications to the original single axis were needed to ensure proper performance. These modifications included a larger stepper motor combined with a new pulley system to efficiently lift the spanwise addition with little vibrations, a stabilizing side wing to restrict the spanwise section from rotating about the vertical axis, and additional supports to make the spanwise section level. Care was taken to ensure that each of the electrical components was connected through different electric circuits in the FPF to avoid interference and cross-communication between the two traverse motors. Previous hot-wire probes were then used to check the functionality of the traverse as well as find the appropriate operation speeds to minimize vibration of the probe to best avoid breaking wires during the actual experiments. In addition, to check the level of the spanwise section, each spanwise measurement location was independently recorded and compared to a reference height. The offset in the wall-normal direction was then implemented into the traverse code to ensure each spanwise point was level. This was done at each measurement location.

2.3 Junction Body

The junction body used was the well-documented 3:2 semi-elliptical nose with a NACA 0020 airfoil tail that melds at the maximum thickness [7]. This body is known as the Rood airfoil. The streamline curvature of the body with consideration of the no-slip condition provides a lateral straining of interest but without separation at the aft of the body. The body is referred to as the airfoil for the remainder of this thesis. The airfoil specifications were based on the specific experimental case. The boundary layer thickness δ_{99} at x = 30m in the FPF is approximately 0.4m thick, to ensure the entire boundary layer was consider δ_{99} was over estimated to be 0.5m in the following calculations. The airfoil therefore was made to have a height H = 0.5m to ensure the entirety of the boundary layer interacted with the body. The thickness was then determined by $T = \frac{1}{2}\delta_{99}$ to be 0.25m. The thickness was then used to satisfy the chosen airfoil shape which led to an overall cord length 1.051m. The airfoil was custom manufactured out of 16-gauge aluminum. The top and bottom were water jet cut into the correct shape, an internal frame then connected the two together, and finally a sheet was wrapped around to enclose the shape shown in figure 2.3.1. In addition to the airfoil, a simple fairing was added for a second group of experiments. The fairing had a height of two inches. The fairing was 3-D printed in two pieces and melded together using acetone. It was then sanded to a smooth surface

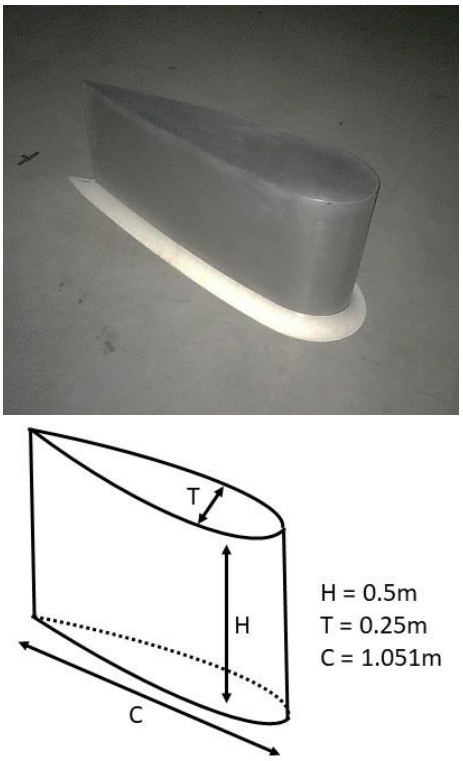

Figure 2.3.1: (a) NACA 0020 airfoil with 3:2 elliptical nose with simple fairing (b) airfoil sketch with dimensions

finish to meld with the airfoil body. Experiments were performed with and without the fairing on the airfoil.

2.4 Experimental Setup

The airfoil was placed at x = 30.6 m from the entrance to the test section. This was chosen to allow for significant boundary layer growth prior to the airfoil. A summary of the undisturbed boundary layer properties at the body is given in table 2.4.1. This also allowed for a significant length remaining in the test section to investigate the wake recovery. The incoming boundary layer was found to have a δ_{99} = 0.379m and would remain steady throughout an experiment but would vary somewhat during a different experiment owing to day-to-day variations in atmospheric conditions.

Table 2.4.1: Boundary Layer Properties at airfoil

U_∞	δ_{99}	u_τ	ν	Re_θ
6.47	0.379m	0.229	1.443 x 10^{-5}	19600

The undisturbed boundary layer is presented in figure 2.4.2. The streamwise velocity mean and variance, along with the wall-normal velocity variance and spanwise velocity variance are presented. They are inner-normalized based on Klewicki [2]. This will specifically be discussed in section 3.1. The mean is represented by a capital letter U, and the fluctuating velocity is represented by the lower-case letter u, v, and w. The overbar denotes that the values are time averaged. The figures show the aspects of 2-D turbulent boundary layer flows. These include the log region in the streamwise mean, the step-like shape in the streamwise variance, the peak in the wall-normal variance, and the two distinct slopes of the spanwise variance.

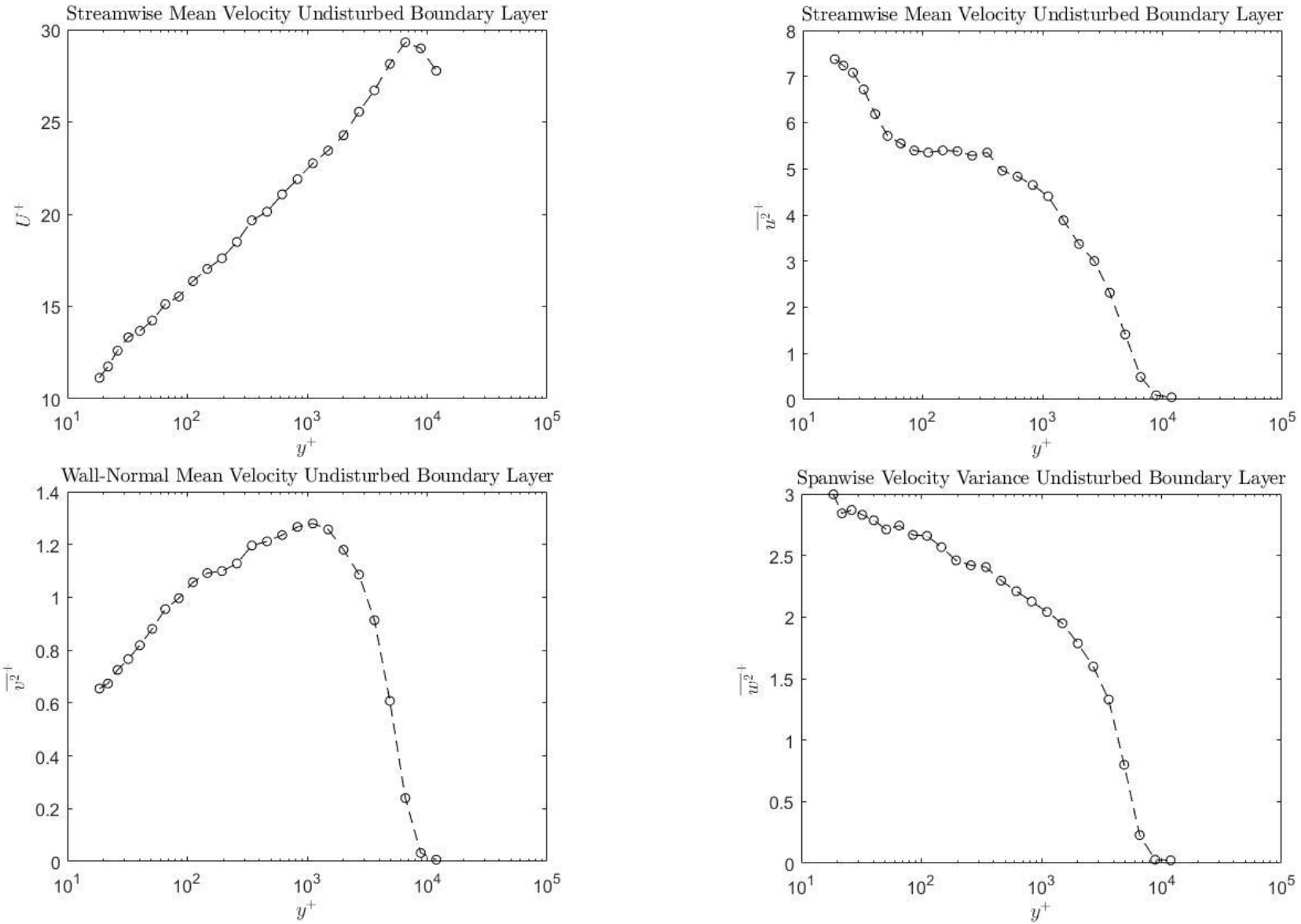

Figure 2.4.1: Inner-normalized undisturbed zero pressure gradient turbulent boundary layer (a) Streamwise Mean (b) Streamwise Variance (c) Wall-Normal Variance (d) Spanwise Variance

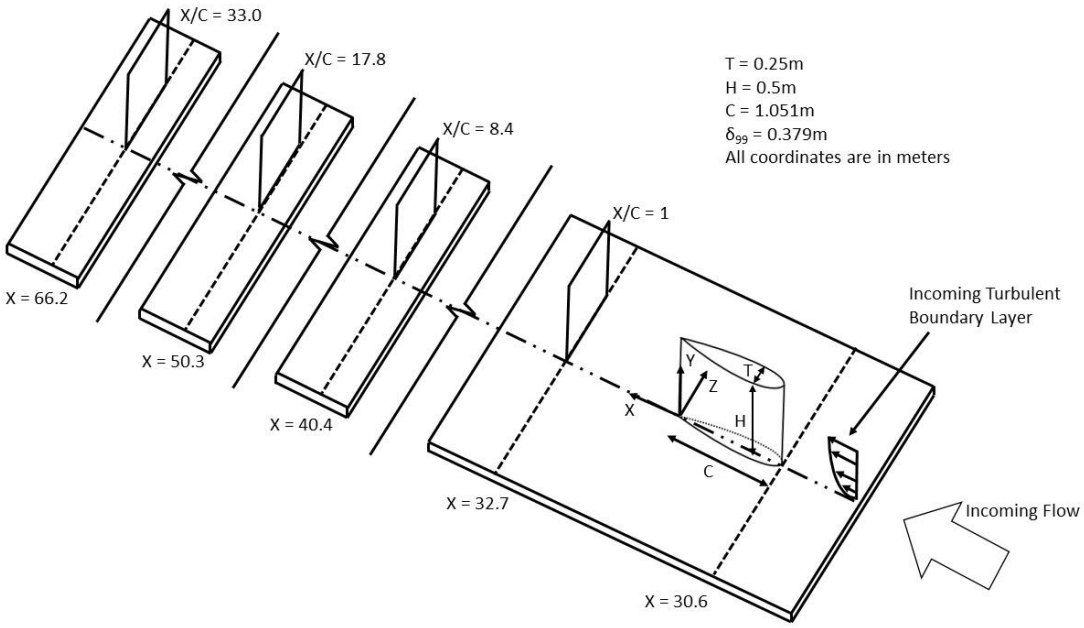

Figure 2.4.2: Sketch of airfoil, incoming undisturbed boundary layer, coordinate system, and measurement plane

Figure 2.4.3 shows the coordinate system and the measurement planes that are used throughout. The x-coordinate is positive moving from the entrance of the tunnel to the exit in the streamwise direction. The y-coordinate is in the wall-normal direction with the origin at the wall. The z-coordinate is in the spanwise direction in which the zero point is the centerline of the tunnel which corresponds to the centerline of the airfoil. Positive z is to the right when looking in the positive streamwise direction. The airfoil is symmetric, and therefore measurements were only taken in the positive spanwise direction. Each measurement plane was made

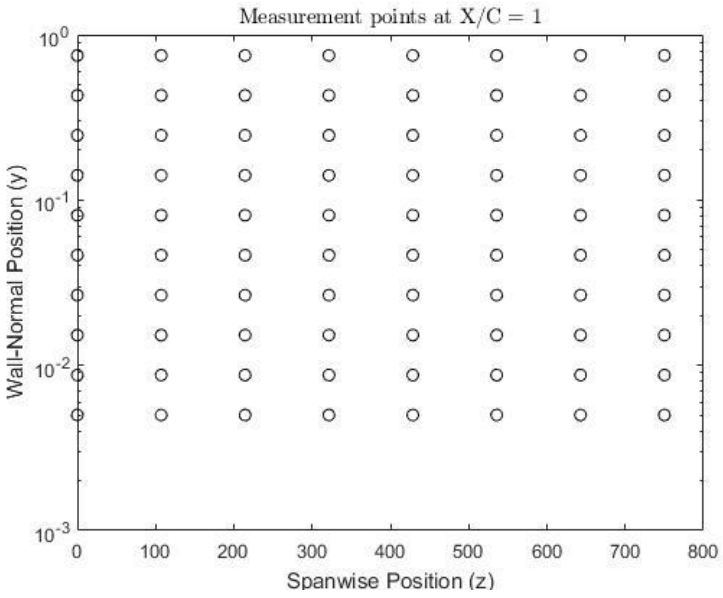

Figure 2.4.3: Example measurement plane at x/c = 1

up of eight spanwise measurements at ten different wall-normal positions creating an eighty-point plane. The planes varied from 0.75m to 1.4m in the spanwise direction at each downstream location while they varied from 0.75m to 0.8m in the wall-normal direction at each downstream location. Figure 2.4.3 shows an example of a measurement plane at X/C = 1.

The measurement planes are located at x = 32.7, 40.4, 50.3, and 66.2m from the tunnel entrance. The location of the planes is normalized by the cord length of the airfoil with the airfoil tail being X/C = 0. The planes are therefore at X/C = 1, 8.4, 17.8, and 33 cord lengths respectively.

Each measurement was taken for 1 minute at 15 kHz. The measurements were taken between sunrise and sunset to minimize temperature drift from atmospheric changes. Pre and post calibrations were taken according to Zimmerman's [12] processing to correct for the existing temperature drift as well as 2-D calibration at each measurement location for the probe itself. The final experimental setup is presented in figure 2.4.4.

Figure 2.4.4: Final experiment setup including: airfoil, 2D traverse, hot-wire probe, and computer system in the UNH FPF

2.5 Preston Tube Experiment

In order to make a comparison to the equilibrium undisturbed boundary layer case, it is beneficial to have measurements of the friction velocity. The friction velocity, u_τ, is a characteristic velocity for canonical (equilibrium) flows. [2]. Estimates of friction velocity can be obtained by velocity profiles finely spaced near the wall, using a Clauser plot for canonical flows, or using a Preston tube experiment. A Preston tube is needed because the probe is not small enough to get into the viscous sublayer. Therefore, the Preston tube experiment was performed to obtain estimates of the friction velocity. A Preston tube is simply a pitot tube that is placed on the floor of the tunnel. This Pitot pressure is then referenced to the local static pressure. The boundary layer approximations show that the pressure gradient in the wall-normal direction is zero. This allows the static pressure measurement to be taken at any point above the Preston tube. For simplicity in the experiment, the static port of a Pitot-static tube was connected to the pressure transducer along with the Preston tube. The Pitot-static tube was located in the freestream. Since the FPF has no significant variability in the spanwise direction, (see FPF description), the Pitot-static tube was set to the side to avoid any flow interaction from the stand on the Preston tube. The Preston tube was aligned using a laser at each spanwise measurement location corresponding to those taken with the hot-wire. Using Patel's [13] calibration we can solve for the wall shear stress and thus the friction velocity. Patel found a general relationship below:

$$\frac{\tau_w d^2}{4\rho v^2} = F\left(\frac{\Delta p_p d^2}{4\rho v^2}\right), \tag{2.1}$$

where d = outer diameter of Preston tube and Δp_p = pressure difference

Using this relationship, he developed a series of equations depending on the differential pressure between the static pressure and the Preston tube pressure. There are three equations used to find the wall shear stress. First, he defines two variables shown below:

$$x^* = log_{10}(\frac{\Delta p_p d^2}{4\rho\nu^2}) \qquad y^* = log_{10}(\frac{\tau_w d^2}{4\rho\nu^2}) \tag{2.2}$$

The equation used depends on a range of y^*. The equations are as follow

For $3.5 < y^* < 5.3$

$$x^* = y^* + 2log_{10}(1.95y^* + 4.10) \tag{2.3}$$

For $1.5 < y^* < 3.5$

$$y^* = 0.8287 - 0.1381x^* + 0.1437x^{*2} - 0.0060x^{*3} \tag{2.4}$$

For $y^* < 1.5$

$$y^* = \frac{1}{2}x^* + 0.037 \tag{2.5}$$

Once y^* is obtained, the wall shear stress can be calculated, and therefore estimates of the friction velocity as well. Numerous equilibrium cases were run to compare to previous friction velocity measurements in the FPF to check for accuracy in the present experiments at downstream locations of x = 34, 50, 66. The previous friction velocity measurements being compared are from Zimmerman's hot-wire boundary layer data found using a Clauser plot [12]. It was expected that the Preston tube results would have a difference as they depend on capturing the lower portion of the logarithmic region. Since the boundary layer is so large, small diameter Preston tubes are not as accurate in the FPF. Therefore, the largest diameter Preston tube was used for the primary measurement and a correction factor was added. It was found that with a correction factor of 0.945 that the friction velocity at all locations was within 2% of S.

Zimmerman's values as well as showing good agreement between the various sized Preston tubes with the largest being the most accurate. The three Preston tube diameters used were 0.00635m, 0.008001m, and 0.0127m. The final friction velocity results are presented in Table 2.5.1 and Table 2.5.2. Error from the changing environmental conditions effecting the flow cannot be measured.

Table 2.5.1: Friction velocity for Airfoil									
Airfoil u_τ									
Spanwise (Z/T)	0	0.428	0.857	1.285	1.714	2.143	2.571	3	TBL
X/C = 1	0.259	0.259	0.244	0.224	0.239	0.245	0.235	0.232	0.229
Spanwise (Z/T)	0	0.571	1.143	1.714	2.286	2.857	3.429	4	
X/C = 8.4	0.253	0.252	0.244	0.234	0.231	0.226	0.226	0.231	
Spanwise (Z/T)	0	0.686	1.371	2.057	2.743	3.429	4.114	4.8	TBL
X/C = 17.8	0.247	0.246	0.242	0.229	0.230	0.225	0.225	0.225	0.225
Spanwise (Z/T)	0	0.8	1.6	2.4	3.2	4.0	4.8	5.6	TBL
X/C = 33	0.241	0.238	0.234	0.230	0.228	0.224	0.223	0.220	0.223

Table 2.5.2: Friction velocity for Airfoil with Fairing									
Airfoil with Fairing u_τ									
Spanwise (Z/T)	0	0.429	0.857	1.286	1.714	2.143	2.571	3	TBL
X/C = 1	0.266	0.265	0.254	0.227	0.236	0.239	0.230	0.236	0.229
Spanwise (Z/T)	0	0.571	1.143	1.714	2.286	2.857	3.429	4	
X/C = 8.4	0.255	0.251	0.246	0.239	0.229	0.231	0.226	0.237	
Spanwise (Z/T)	0	0.686	1.371	2.057	2.743	3.429	4.114	4.8	TBL
X/C = 17.8	0.252	0.250	0.243	0.236	0.227	0.231	0.238	0.233	0.225
Spanwise (Z/T)	0	0.8	1.6	2.4	3.2	4.0	4.8	5.6	TBL
X/C = 33	0.239	0.237	0.234	0.227	0.224	0.221	0.221	0.222	0.223

2.6 Uncertainty

The absolute uncertainty of multi-element hot-wire measurements is difficult to estimate, S. Zimmerman (private conversation). This stems from several factors. These include the changing environmental conditions of the FPF along with the many components of the calibration process. This makes it impossible for an uncertainty percentage for each contribution to be calculated and for error bars to be shown on plots. However, it was recommended by Zimmerman, that one can get an overall estimate of the uncertainty by looking at measurement results which do not agree with what is known to occur physically, to within the accuracy of the experiment, pertaining to the two-dimensionality of the undisturbed boundary layer. Two of these measurements are the turbulent shear stress of $\overline{uw}$ and $\overline{vw}$ for the zero-pressure gradient turbulent boundary layer. These values should be very close to zero at all wall-normal positions. Figure 2.6.1 shows measured values of these quantities at the three downstream locations where they are available from the canonical flow. The values are time averaged which is denoted by the overbar. The turbulent shear stress $\overline{uw}$ varies significantly near the wall and then is negative. It only reaches zero at the far edge of the boundary layer. The turbulent shear stress $\overline{vw}$ is always positive and only reaches zero at the far edge of the boundary layer. Zimmerman et al. [12] discuss the agreement of statistics with that of direct numerical simulations (DNS) of the Navier Stokes equations. It has been found that the mean streamwise velocity, variances of the fluctuations, turbulent shear stress $\overline{uv}$, turbulence kinetic energy, vorticity fluctuations, and spectra exhibit very good agreement with DNS. Therefore, in the discussion of the present results, observations will be made with this in mind, and the uncertainty of each measurement will be considered.

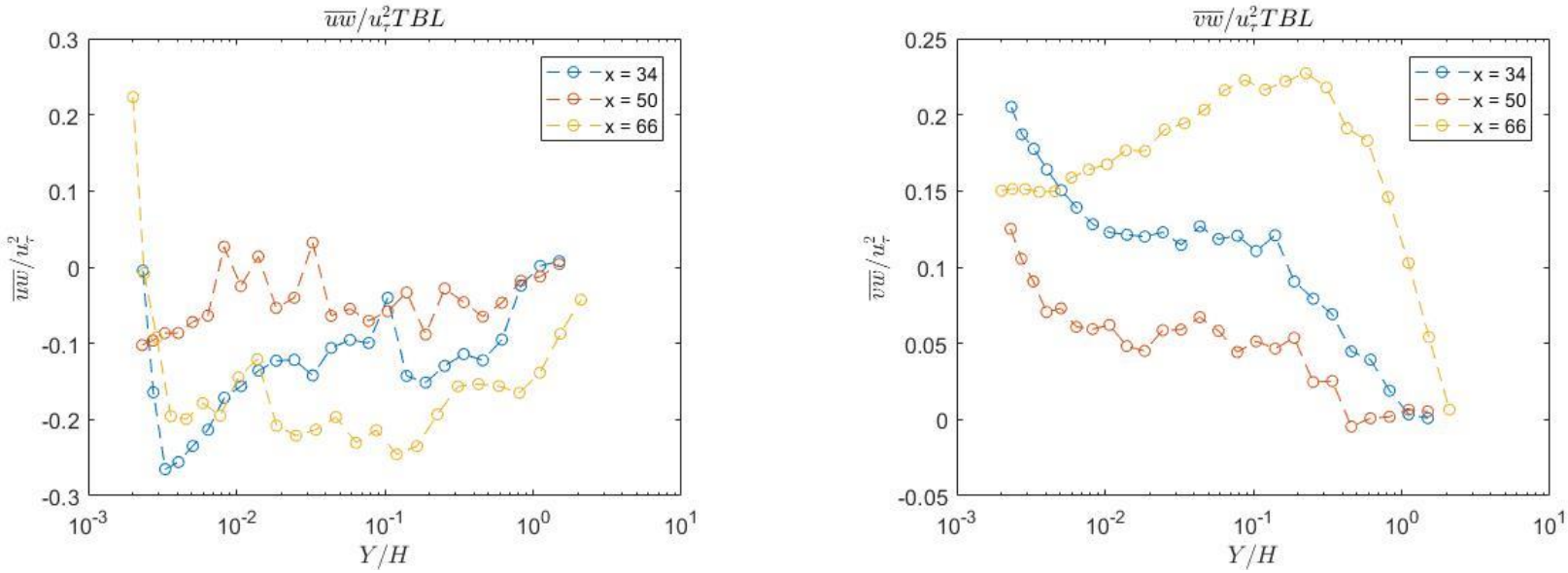

Figure 2.6.1 Inner-normalized undisturbed zero pressure gradient turbulent boundary layer (a) Reynolds Stress $\overline{uw}$ (b) Reynolds Stress $\overline{vw}$

CHAPTER 3: RESULTS

Experiments were performed with a freestream velocity U_∞ = 6.5 ± 0.3 m/s with an incoming boundary layer height of roughly 0.38m. Data was obtained from the four measurment planes at X/C = 1, 8.4, 17.8, 33 downstream of the airfoil for both the airfoil with and without a fairing. The origin of this coordinate system is at the downstream end of the airfoil. The following results will show a given variable of intrest at a particular measurement plane. The spanwise location of the measurements are given by z/T or the spanwise location normalized by the thickness of the airfoil. The wall-normal locations are normalized by the height of the airfoil Y/H. Some color maps are presented to show the wake and the remainder of the data will be presented as wall-normal profiles at a given spanwise-location.

3.1 Normalizations

Boundary layers have various characteristic scales associated with them. Normalizations using these different scales aid in interpreting the underlying physics. There are two primary normalizations. Inner normalization reflects the dynamics and characteristics of the flow in which the primary interaction is with the wall, particularly the wall shear stress. A characteristic velocity can be created known as the friction velocity leading to $u_\tau = \sqrt{\tau_w/\rho}$ where τ_w is the wall shear stress and ρ is the fluid density. Boundary layer dynamics transport (on average) high-momentum fluid toward the wall, resulting in an increased wall shear stress relative to a laminar

flow. Therefore, the friction velocity serves as an ideal velocity scale to normalize flow variables of interest. Therefore, in the present study, the friction velocity will be used for inner-normalization. The second normalization is the so-called outer normalization associated with the bulk motions of the flow. Typically, the characteristic length scale used is the boundary layer height, but because of the non-equilibrium nature of the flow, the height of the airfoil is used for the outer normalization. The velocity, as is typically done, will be normalized by the freestream velocity. Consistently, previous experimental studies such as Fleming et al. [7] used the airfoil thickness and freestream velocity to normalize the results.

3.2 Friction Velocity Dependence

The friction velocity is used to normalize the statistics as discussed above. Since the flow is modified by the airfoil to create non-equilibrium conditions, the friction velocity is modified in comparison to the undisturbed case. As the friction velocity is used to normalize the statistical profiles, it is important first to examine how the friction velocity changes in the wake of the airfoil. Figure 3.2.1 shows friction velocity estimates derived from shear stress beneath each measurement plane. This figure presents the undisturbed case, the airfoil case, and the case of the airfoil with the fairing. Error bars are added to indicate the 2% error discussed in section 2.5.

The X/C = 1 results near z/T = 0 indicate a large increase in the friction velocity relative to the undisturbed boundary layer. The friction velocity at z = 1.3 is equivalent to the undisturbed case. The values then get slightly larger again before coming back to the undisturbed case. The remaining three planes all show the same trend. The friction velocity near z/T = 0 have larger values. The friction velocity then decreases as z/T increases. X/C = 8.4 does not have an undisturbed case for comparison. At X/C = 17.8 the friction velocity is equal to the undisturbed

case at roughly z = 2. At X/C = 33 the friction velocity is equal to the undisturbed case at roughly z = 4.

The larger friction velocity estimates reflect an increase of freestream momentum flux into the wall. The friction velocity estimates near z = 0 are large. The relative difference between the friction velocity estimates to the undisturbed case decreases at each downstream measurement plane. The spanwise location at which the friction velocity becomes equivalent to the undisturbed case is farther from the centerline at each downstream location. These findings give insight into how to interpret the statistical results normalized by the friction velocity. The spreading of the wake is observed as well as the increase wall momentum flux caused by the junction flow. Lastly, it is apparent that the friction velocity does not make a full recovery in the last measurement plane.

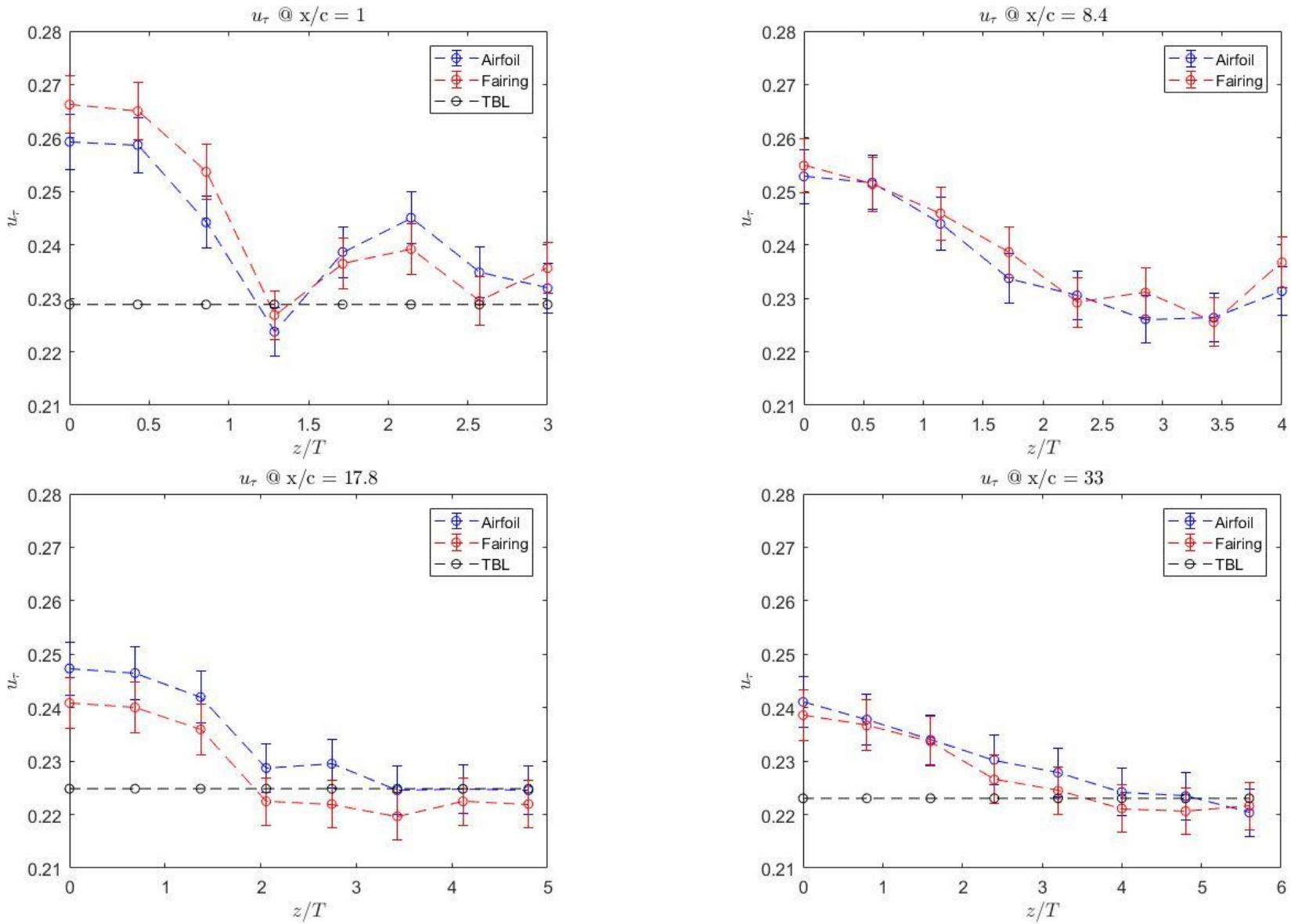

Figure 3.2.1: Preston tube base friction velocity estimates at (a) X/C = 1 (b) X/C = 8.4 (c) X/C = 17.8 (d) X/C = 33 for the airfoil case, the airfoil with fairing case, and undisturbed turbulent boundary layer case (TBL)

3.3 Comparison to Similar Previous Experiments

Fleming et al. [7] presents wake data of the streamwise mean and velocity variance for planes of x/C = 1.50 to 11.56, where x/C = 1 is at the trailing edge of the airfoil. However, planes x/C = 9.14, 11.56 were taken in an adverse pressure gradient. Therefore, the focus will be on the noted planes from the Fleming et al. study as compared to X/C = 1, 8.4 from the present study where X/C = 0 is at the trailing edge of the airfoil in the present case. Figure 3.3.1 shows color countors for the streamwise mean and velocity variance normalized by the freestream velocity at X/C = 1 and 8.4. The discrete data were linearly interpolated to generate smooth color variations on the image. The airfoil is oriented to the left of each figure where z/T = 0 is the centerline of the airfoil and tunnel. The apparent effect of the horseshoe vortex can be observed at X/C = 1 by looking at the peak in velocity variance. The peak is between z/T = 1 to 1.5. The influence of the vortex on the mean streamwise velocity can be observed at the same location. Contour plots of streamwise mean and velocity variance from Fleming et al.[7] at x/C = 1.50 agree with the present study. Their x/C = 3 measurement plane shows that the signature from the junction moves outward to a larger z/T. The present study X/C = 1 fits in between these two planes. It can be deduced that the vortex is located at a similar position in both experiments, as the peak in the velocity variance is at z/T = 1 to 1.5 in both cases. The mean velocity distortion pattern occurs at the same location as well. In all of the near plane contours for both studies, one can observe the deficit by z/T = 0 behind the airfoil as one would expect from having a body in the flow.

Observing the remaining Fleming et al. [7] data planes, the distortion of the mean velocity spreads outwards away from the airfoil and diffuses upward away from the wall. The present study at X/C = 8.4 shows the same process. The strong peak in the velocity variance in Fleming et al. [7] rapidly diminishes with downstream distance. Turbulence is transported

throughout the boundary layer in a similar manner to the mean velocity. The present measurements at X/C = 8.4 exhibit results consistent with this. The comparison to Fleming et al. [7] substantiates that the present study has the same characteristic flow features. This will allow for further analysis to build off past experiments, expanding the understanding of the flow through the addition of added measured quantities, as well as downstream measurement locations in a zero-pressure gradient turbulent boundary layer flow.

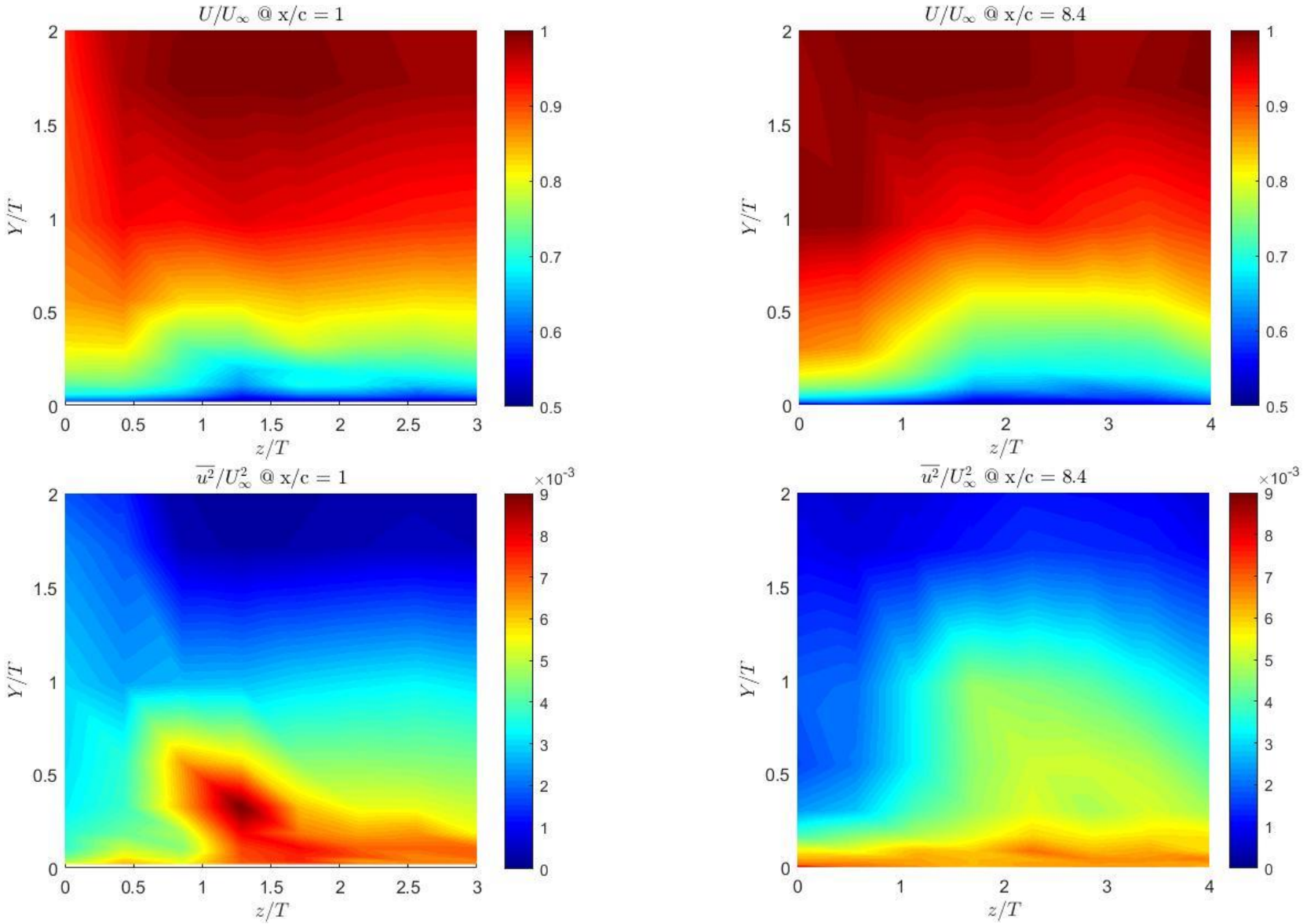

Figure 3.3.1: Streamwise Velocity Contours (a) U/U_∞ X/C = 1 (b) U/U_∞ X/C = 8.4 (c) $\overline{u}^2/U_\infty$ X/C = 1 (d) $\overline{u}^2/U_\infty$ X/C = 8.4

3.4 Downstream Development of Velocity Statistics

The downstream development of the mean streamwise velocity, velocity variance, and turbulent kinetic energy are now presented and described. Presentation of the data is such that at each measurement location downstream of the airfoil, wall-normal profiles are presented for eight different spanwise locations within the measurement plane. For the measurements at X/C = 1, 17.8, and 33 the corresponding profiles of 2-D undisturbed turbulent boundary layer flow acquired at the same measurement location are provided. The velocity statistics were normalized using the friction velocity and freestream velocity, and the y-location was normalized by H. When significant, differences between normalizations are noted and described.

The normalized streamwise mean velocity profiles are shown at the four downstream measurement planes in figure 3.4.1 and figure 3.4.2. The normalization by friction velocity shows a considerable variability at plane X/C = 1 for locations Y/H > 0.1. This variability decreases with downstream distance. However, in comparison to the undisturbed case, X/C = 1 is both above and below the undisturbed case while at X/C = 17.8 they are all below. A kink in the profiles at X/C = 17.8 for both normalizations is observed but disappears in the X/C = 33 plane. Interestingly, now the profiles are above the undisturbed case. The normalization by the freestream velocity shows a slightly different trend. The profiles at X/C = 1 are spread out closer to the wall and converge farther from the wall. The profiles slowly converge with increasing downstream distance, but by X/C = 33 the profiles $0 \leq Z/T \leq 3.2$ are slightly below the undisturbed case while the profiles for $Z/T \geq 3.2$ are on or slightly above the undisturbed case.

Both normalizations show that the profiles tend to converge with increasing downstream distance. However, at X/C = 17.8 both normalizations are above the undisturbed case, at X/C = 33, the freestream normalization falls approximately on the undisturbed case. The friction

velocity normalization is below the undisturbed case leading to an offset when normalized by a higher friction velocity. This, however, is not entirely consistent with the friction velocity data. Some of the profiles are different even when the friction velocity is equivalent to the undisturbed case. This suggests that the flow dynamics are different and it is not a consequence of the normalization. Moreover, since at X/C = 33 the profiles do not converge on the undisturbed case, this suggests that the flow is either still developing or it has found a new equilibrium state.

The downstream development of the root mean squared (rms) profiles of the velocity fluctuations hint at how the turbulence evolves downstream of the airfoil. Figure 3.4.3 shows profiles of the streamwise variance at the different downstream planes. At X/C = 1 a large spread can be seen. The profiles at $z/T \leq 0.857$ are below the undisturbed case while the profiles at $z/T \geq 1.286$ are above the undisturbed case. At z/T = 1.286 one can observe a significant peak at $Y/H \approx 0.2$ that can be associated with the horseshoe vortex. As the flow develops downstream, the peak disappears, and the profiles begin to converge with the inner z/T profiles increasing in value while the outer z/T profiles lessen in value. X/C = 33 shows a significant variability between profiles as well as being lower than the undisturbed case. The normalization by the freestream shows the same trends in figure 3.4.4. It has the same peak at X/C = 1, but the spacing between profiles is less than the friction velocity normalization. The spacing does converge, but unlike the friction velocity case, they converge around the undisturbed case. The differences between the two normalizations are similar to the mean streamwise velocity, a consequence of differences in the friction velocity, but also due to differences in the flow dynamics compared to the undisturbed flow.

The profiles of the wall-normal variance normalized by the friction velocity are shown in figure 3.4.5. At X/C = 1 there are two distinct peaks at locations z/T = 1.286 and z/T = 0.857 at

Y/H ≈ 0.2. These peaks are likely caused by the upwash and downwash regions caused by the horseshoe vortex. The other profiles lack a distinct peak but are greater than the undisturbed case. At X/C = 8.4 the peaks disappear, but a substantial deficit is seen at $z/T \leq 1.143$ in relation to the other profiles. At X/C = 17.8 most profiles converge close to the undisturbed case, but $z/T \leq 1.3714$ falls below the undisturbed case. At X/C = 33 the profiles are below the undisturbed case, most notably under the peak of the undisturbed case at Y/H ≈ 0.2.

Overall, the wall-normal velocity variance again shows evidence of effects of the horseshoe vortex in particular distinct peaks at X/C = 1 and for z/T = 1.286 and z/T = 0.857. Those peaks diminish as the flow evolves downstream. Instead of a peak, there is now, however, a deficit at inner spanwise locations. The deficit remains as the profiles recover close to the undisturbed case. The inner normalized profiles fall below the undisturbed case while the outer normalizations in Figure 3.4.6 fall approximately on the undisturbed case. Except at X/C = 33, the outer normalization is still greater than the inner normalization, but both are below the undisturbed case at Y/H ≈ 0.2. Even at X/C = 33, the flow does not fully recover to the undisturbed case.

The wall-normal profiles of the spanwise velocity variance, shown in figure 3.4.7, have a crest that is probably associated with the horseshoe vortex at X/C = 1. The profiles $z/T < 1.286$ are lower than the undisturbed case, while the profiles $z/T \geq 1.286$ are higher than the undisturbed case. As the flow evolves downstream, the spanwise profiles converge, and the flow recovers towards the undisturbed case. The difference here is that all the profiles are less than the undisturbed case. The freestream normalization shown in figure 3.4.8 shows quantitatively similar results. The spanwise variance is likely influenced by the horseshoe vortex, but in a different way compared to the other velocity components. In particular, turbulence is higher and

modified over a broader wall-normal range. Again, as the flow evolves downstream, the spanwise profiles tend to converge and recover towards the undisturbed case.

Lastly, the downstream evolution of the turbulent kinetic energy (TKE) was evaluated. Turbulent kinetic energy is calculated in the following manner: $TKE = {}^{1}/_{2}\,(\bar{u}^2 + \bar{v}^2 + \bar{w}^2)$. Figure 3.4.9 shows the TKE normalized by the friction velocity at the different downstream measurement planes. At X/C = 1 the peak at z/T = 1.286 is likely a signature of the horseshoe vortex. The profiles at z/T ≤ 1.286 have lower TKE while the profiles at z/T > 1.286 have higher TKE compared to the undisturbed case. The peak is diminished, and the spanwise profiles closest to the centerline remain with lower TKE values while those farther away begin to converge close to the undisturbed case. This remains true for each downstream location, but the differences between the profiles decreases at each location. At X/C = 33 the profiles are below the undisturbed case. The profiles normalized by the freestream velocity shown in figure 3.4.10 exhibit similar qualitative features. However, at X/C = 33 the profiles shows general agreement with the undisturbed case except that z/T ≤ 0.8 are significantly lower while the remaining profiles are higher compared to the undisturbed case. Thus, the friction velocity again expands the profiles and offsets the final measurement plane for the same reasoning as described earlier. The TKE profiles at X/C = 1 demonstrate the effects of the junction flow. The increase in TKE likely due to the horseshoe vortex demonstrate the injection of turbulent energy by the airfoil. Downstream of the airfoil, the additional TKE is dissipated and the flow recovers towards the undisturbed case.

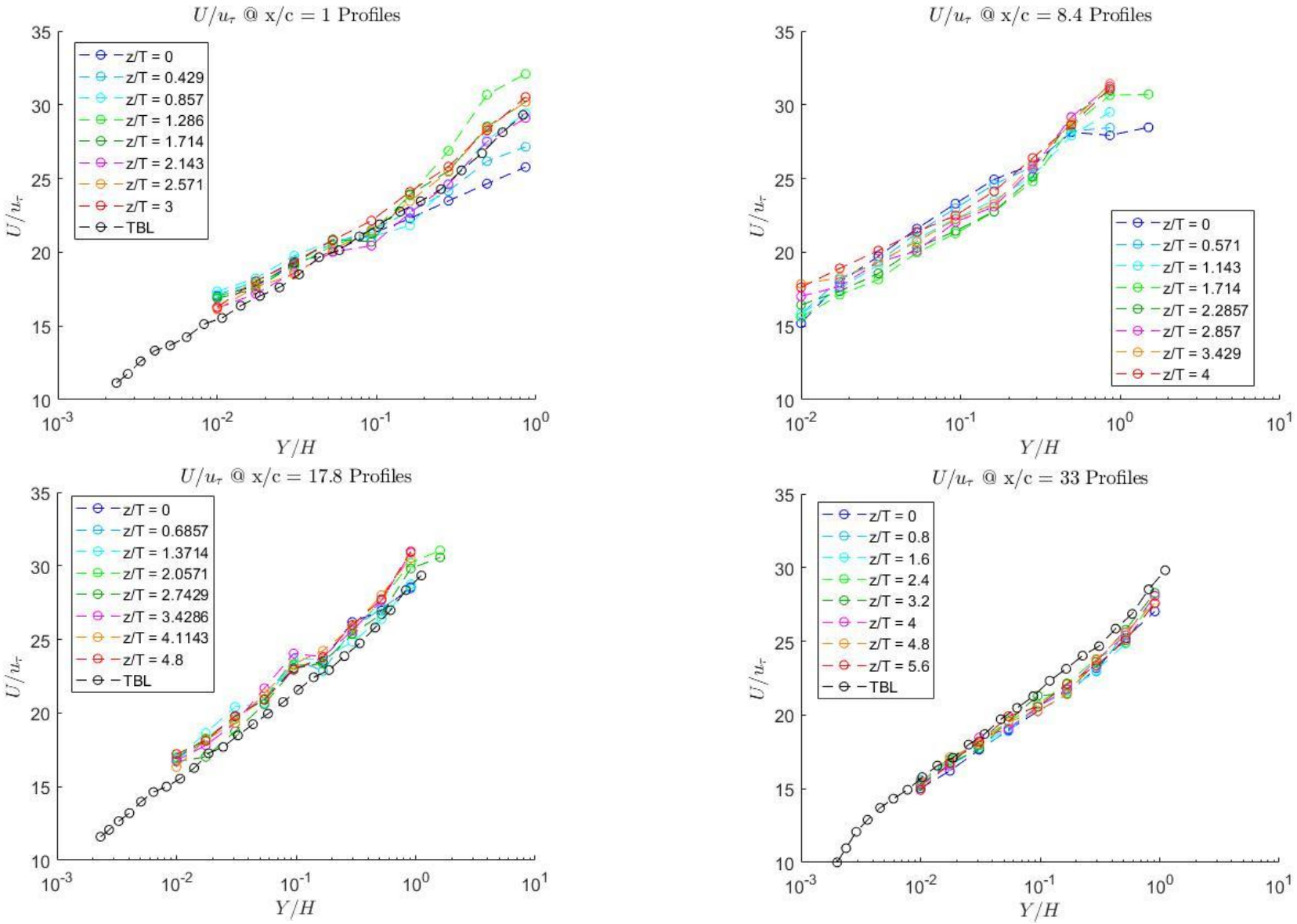

Figure 3.4.1: Streamwise mean velocity profiles normalized by u_τ at (a) X/C = 1 (b) X/C = 8.4 (c) X/C = 17.8 (d) X/C = 33.0 at spanwise locations z/T and undisturbed turbulent boundary layer (TBL)

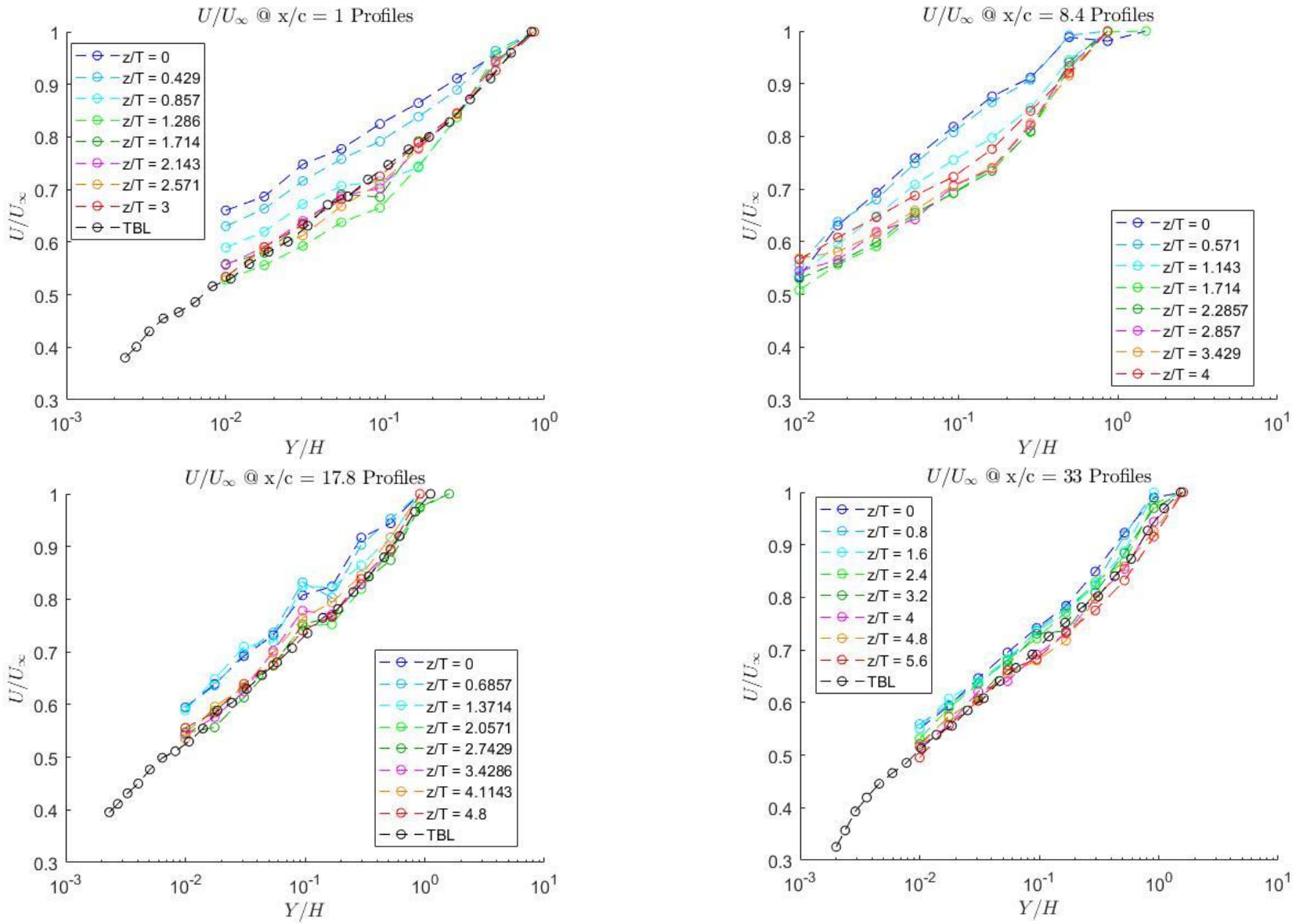

Figure 3.4.2: Streamwise mean velocity profiles normalized by U_∞ at (a) X/C = 1 (b) X/C = 8.4 (c) X/C = 17.8 (d) X/C = 33.0 at spanwise locations z/T and undisturbed turbulent boundary layer (TBL)

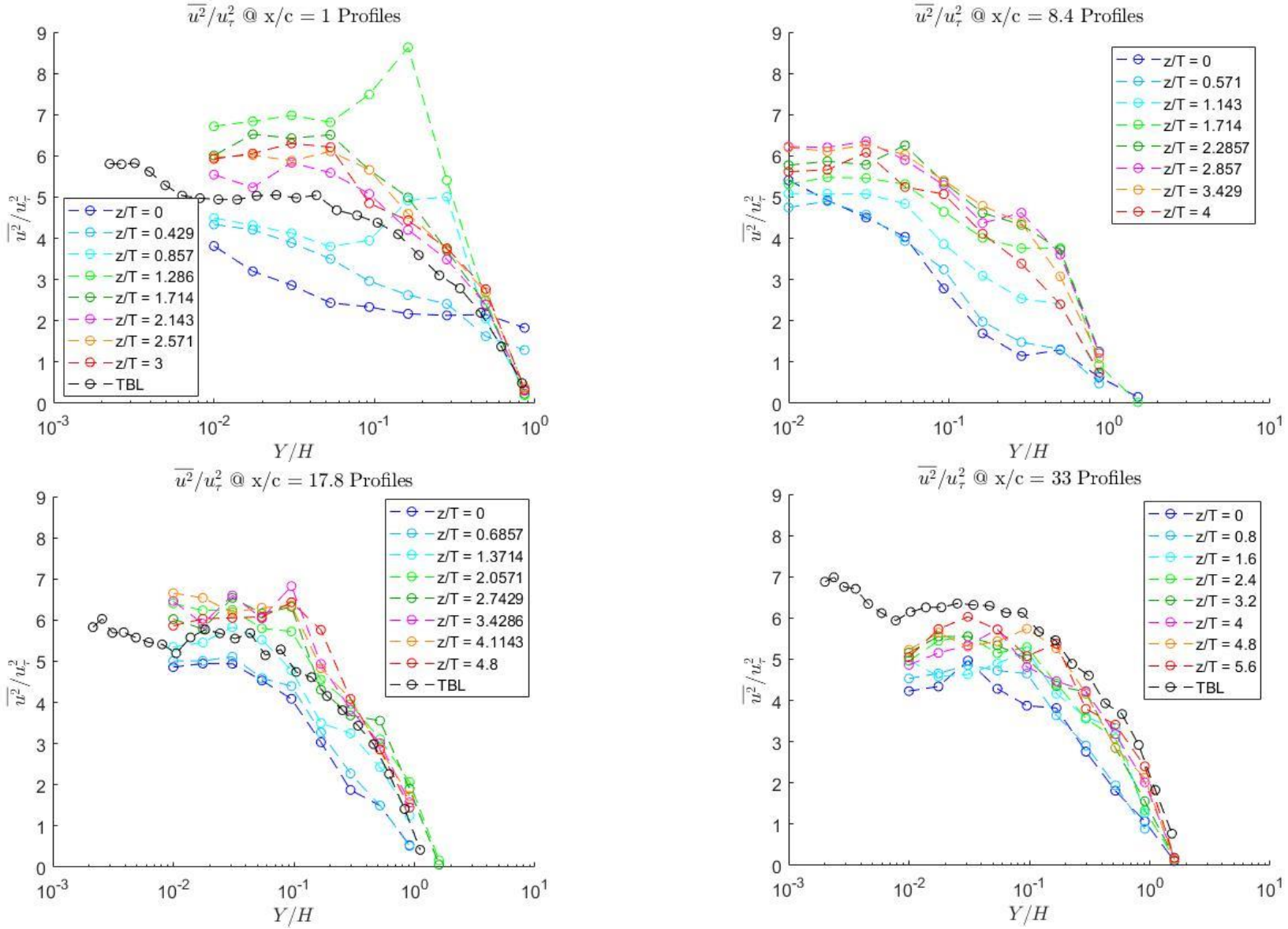

Figure 3.4.3: Streamwise velocity variance profiles normalized by u_τ at (a) X/C = 1 (b) X/C = 8.4 (c) X/C = 17.8 (d) X/C = 33.0 at spanwise locations z/T and undisturbed turbulent boundary layer (TBL)

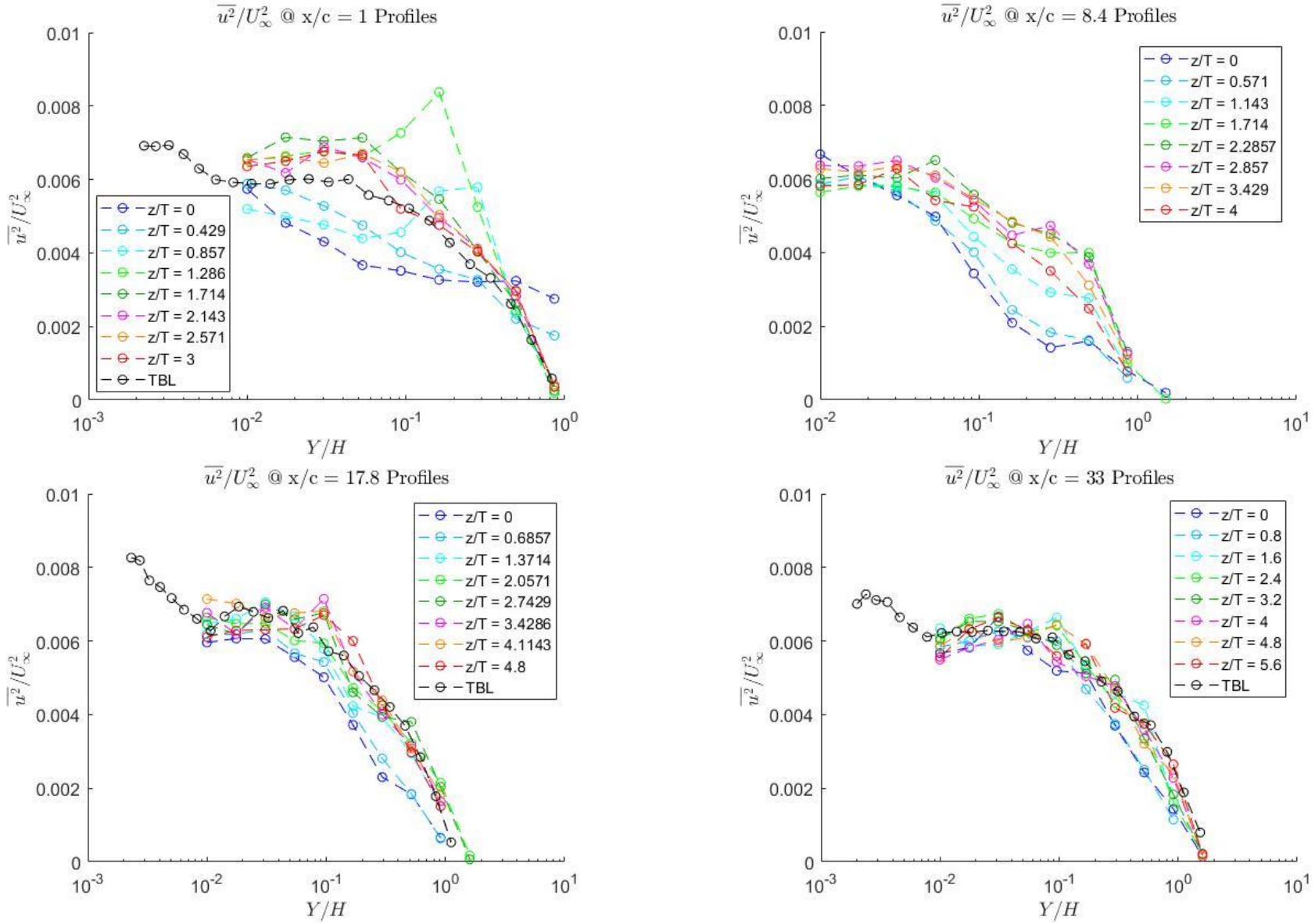

Figure 3.4.4: Streamwise velocity variance profiles normalized by U_∞ at (a) X/C = 1 (b) X/C = 8.4 (c) X/C = 17.8 (d) X/C = 33.0 at spanwise locations z/T and undisturbed turbulent boundary layer (TBL)

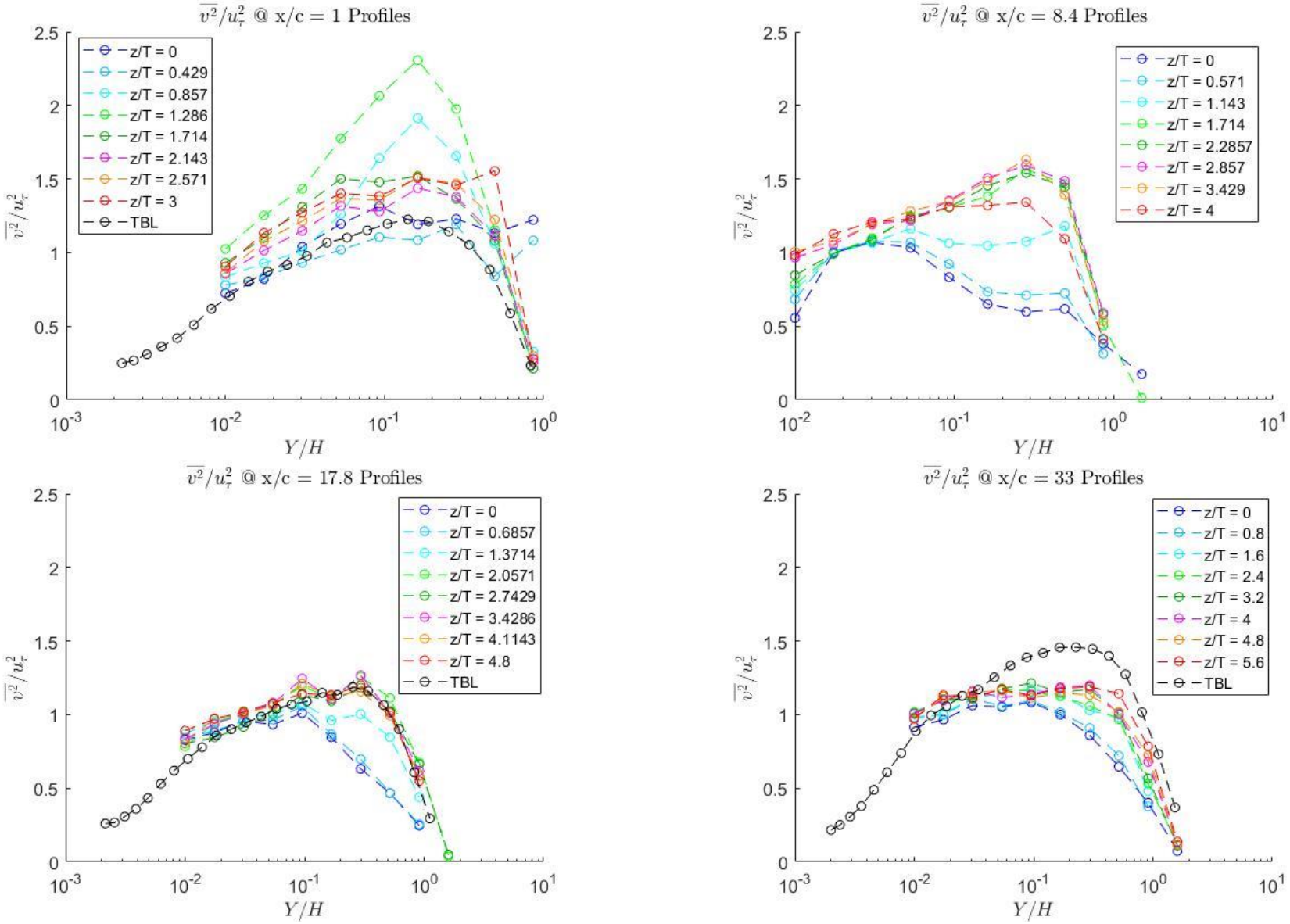

Figure 3.4.5: Wall-normal velocity variance profiles normalized by u_τ at (a) X/C = 1 (b) X/C = 8.4 (c) X/C = 17.8 (d) X/C = 33.0 at spanwise locations z/T and undisturbed turbulent boundary layer (TBL)

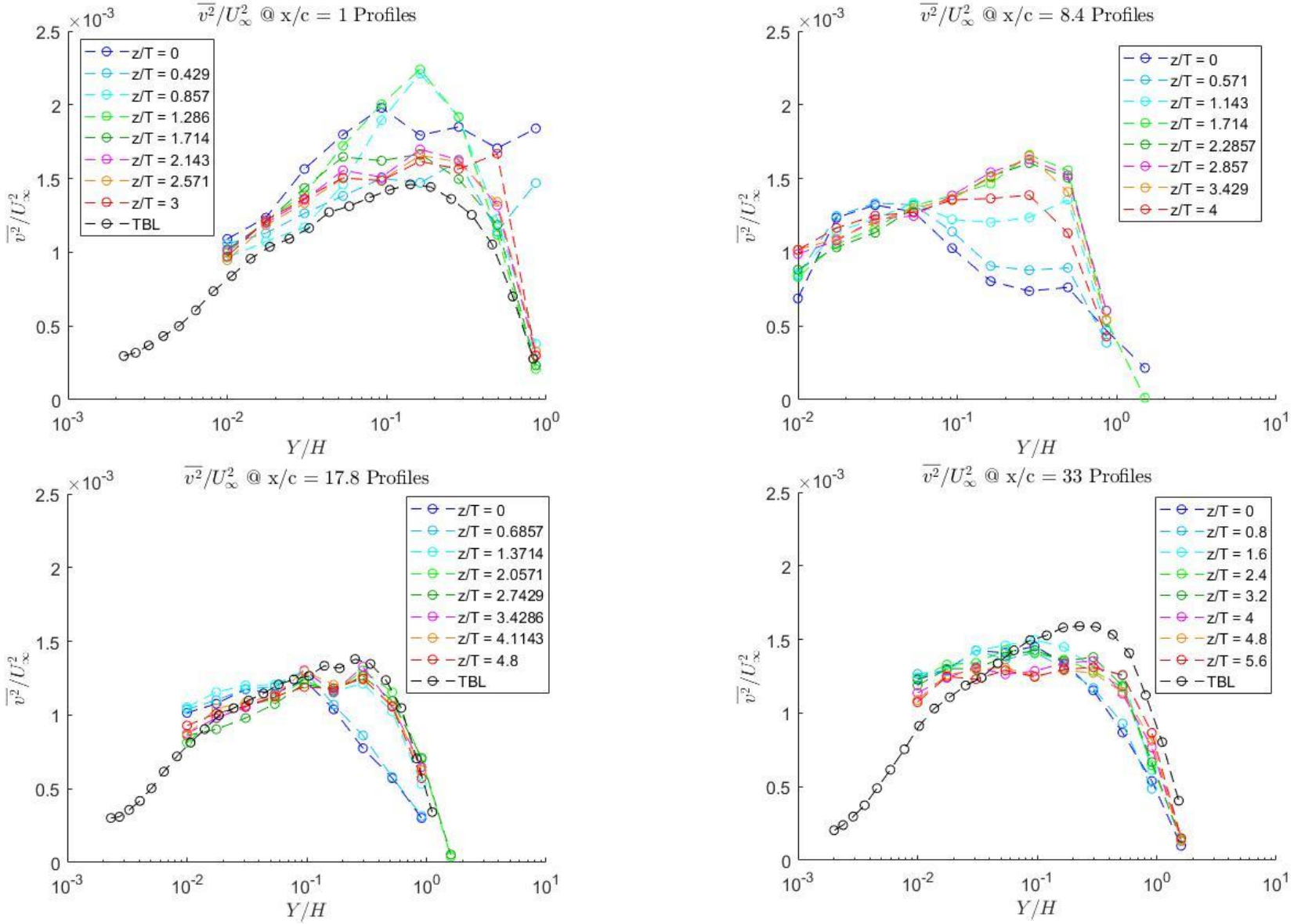

Figure 3.4.6: Wall-normal velocity variance profiles normalized by U_∞ at (a) X/C = 1 (b) X/C = 8.4 (c) X/C = 17.8 (d) X/C = 33.0 at spanwise locations z/T and undisturbed turbulent boundary layer (TBL)

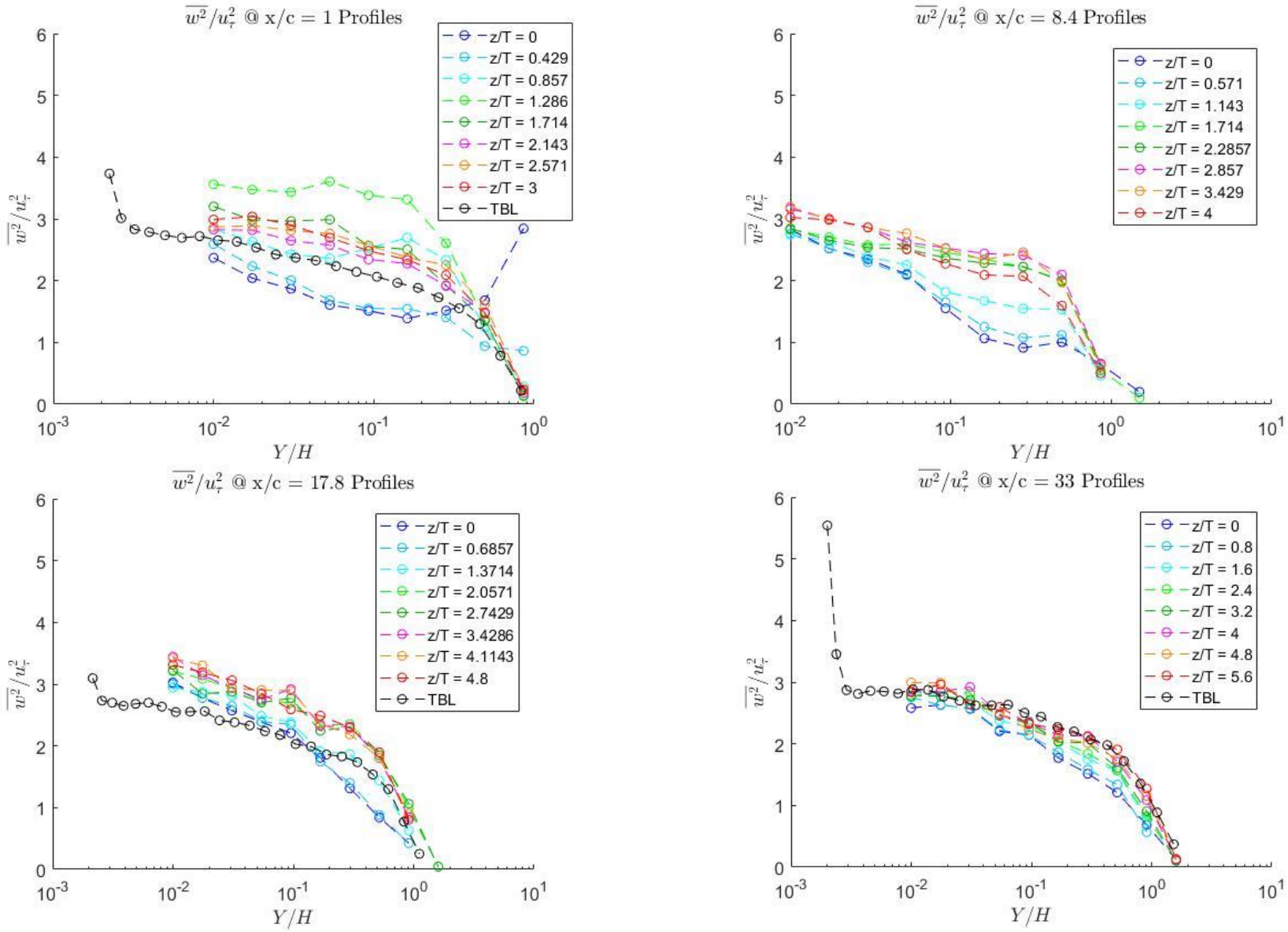

Figure 3.4.7: Spanwise velocity variance profiles normalized by u_τ at (a) X/C = 1 (b) X/C = 8.4 (c) X/C = 17.8 (d) X/C = 33.0 at spanwise locations z/T and undisturbed turbulent boundary layer (TBL)

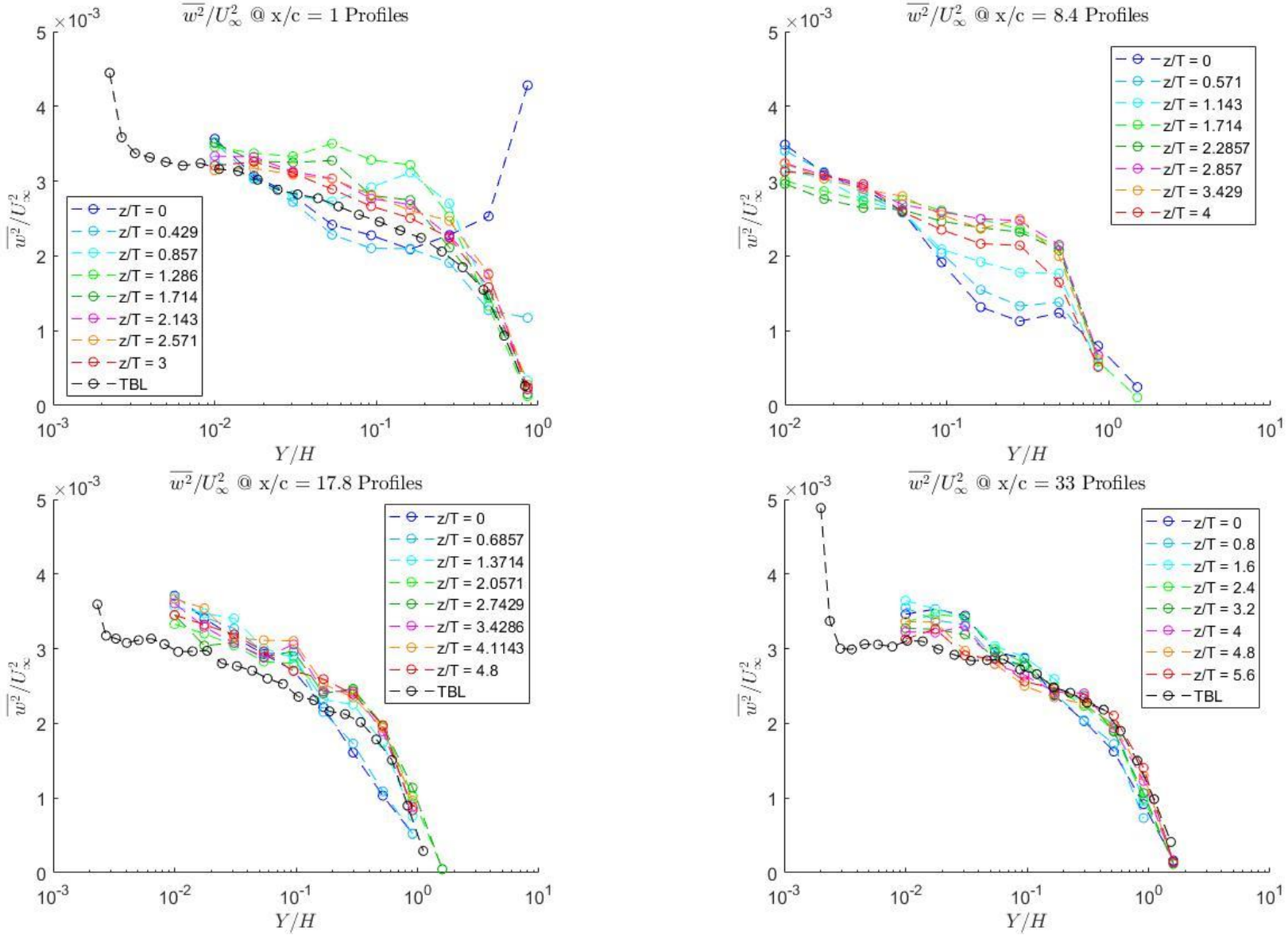

Figure 3.4.8: Spanwise velocity variance profiles normalized by U_∞ at (a) X/C = 1 (b) X/C = 8.4 (c) X/C = 17.8 (d) X/C = 33.0 at spanwise locations z/T and undisturbed turbulent boundary layer (TBL)

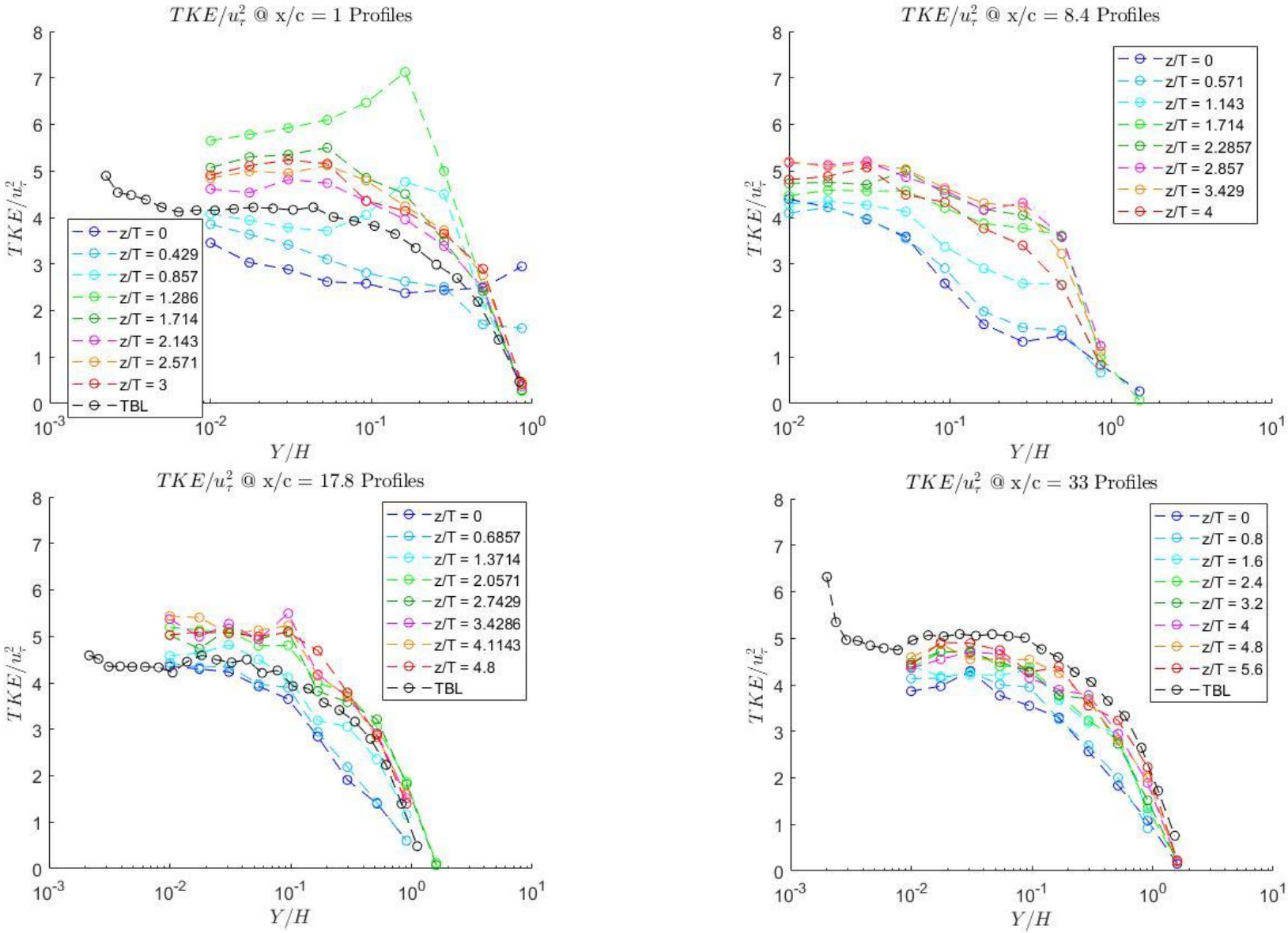

Figure 3.4.9: Turbulent kinetic energy profiles normalized by u_τ at (a) X/C = 1 (b) X/C = 8.4 (c) X/C = 17.8 (d) X/C = 33.0 at spanwise locations z/T and undisturbed turbulent boundary layer (TBL)

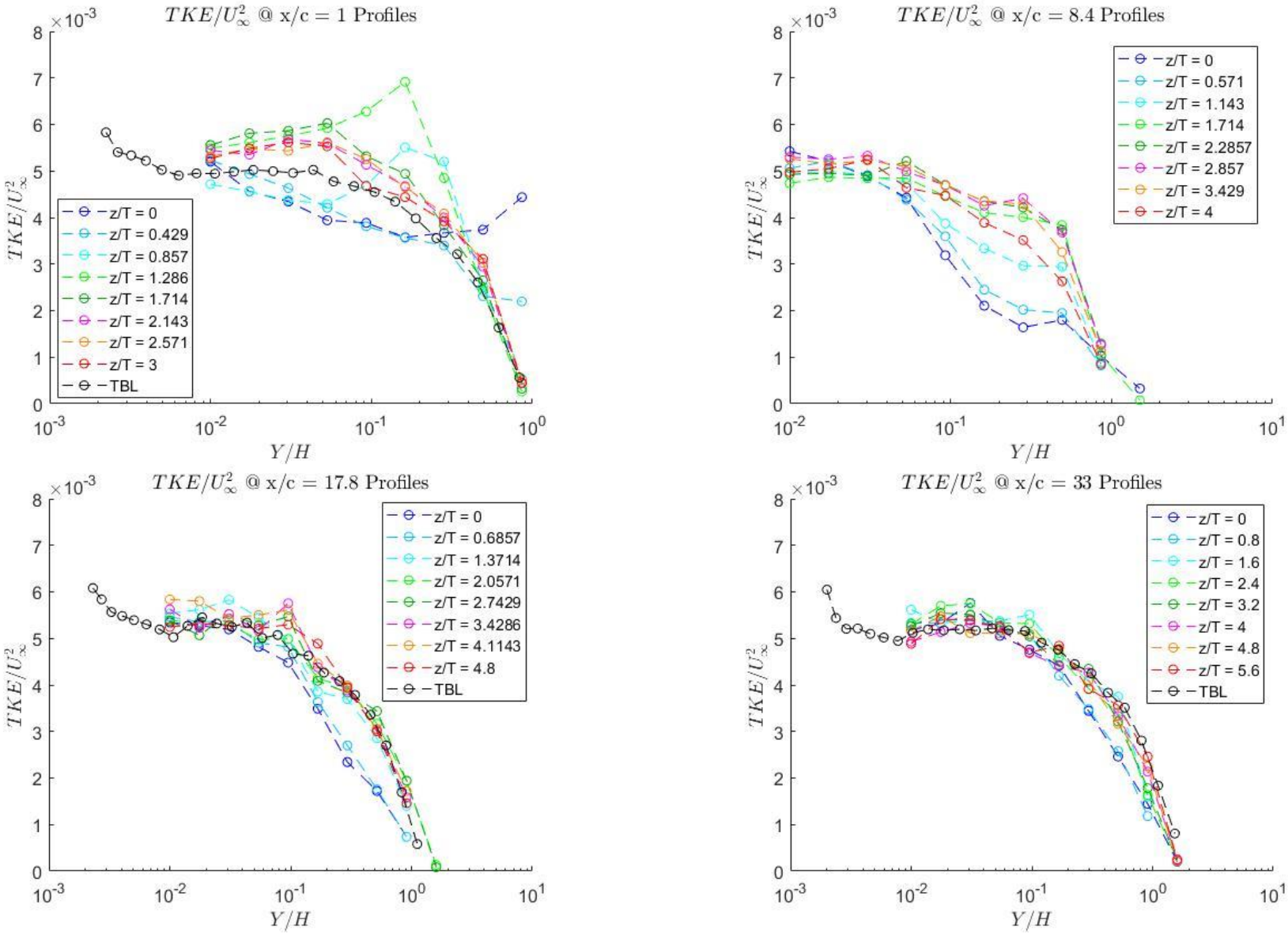

Figure 3.4.10: Turbulent kinetic energy profiles normalized by U_∞ at (a) X/C = 1 (b) X/C = 8.4 (c) X/C = 17.8 (d) X/C = 33.0 at spanwise locations z/T and undisturbed turbulent boundary layer (TBL)

3.5 Downstream Reynolds Shear Stress Development

Wall-normal profiles of the Reynolds shear stress profiles for $\overline{uv}$, $\overline{uw}$, and $\overline{vw}$ normalized by the friction velocity and freestream velocity, are plotted at four measurement planes downstream of the airfoil and at eight spanwise positions at each plane. The uncertainity in the measured values of $\overline{uw}$ and $\overline{vw}$ is relevant here, and thus must be taken in interpreting these profiles. The error bounds associated with $\overline{uw}$ and $\overline{vw}$ will be highlighted in each figure to ensure that observations made are significantly different. The $\overline{uv}$ statistics, therefore, will be the primary interest of the discussion while $\overline{uw}$ and $\overline{vw}$ will only be used to supplement the understanding of $\overline{uv}$.

Figure 3.5.1 shows profiles of the $\overline{uv}$ Reynolds stress at the four measurement planes. Notable observation are that at X/C = 1 there is a negative peak at z/T = 1.286 and Y/H ≈ 0.1. In addition, the values are higher than the undisturbed case for z/T < 1.286. At X/C = 8.4 the peak diminishes and the profiles begin to converge. In this plane, the profiles at z/T < 1.143 are higher than the rest of the profiles. At X/C = 17.8 the profiles have converged together but are all significantly lower than the undisturbed case. At X/C = 33 the profiles remain converged, but the difference relative to the undisturbed case increases. The plots normalized by the freestream shown in figure 3.5.2 show qualitatively similar results.

The $\overline{vw}$ Reynolds stress shown in figure 3.5.3 displays values that exceed the error associated with the undisturbed case as indicated by profiles that fall outside the yellow box. The normalization by the freestream in figure 3.5.4 qualitatively shows similar results. The $\overline{uw}$ Reynolds stress, shown in figure 3.5.5 and figure 3.5.6, also display values that exceed the error

associated with the measurement. Again at X/C = 33, the profiles converge. The significant difference compared to the error for $\overline{uw}$ is not as great as the $\overline{vw}$ but is still observed.

The Reynolds stress represents how mean momentum is transferred by the turbulent motions. The $\overline{uv}$ Reynolds stress provides a measure of how streamwise momentum is transported in the wall-normal direction, $\overline{uw}$ provides a measure of how the streamwise momentum is transported in the spanwise direction, and $\overline{vw}$ provides a measure of the turbulent transport of the spanwise or wall-normal momentum. A negative $\overline{uv}$ Reynolds stress means that high (relative to the mean) streamwise momentum (+u) is being moved toward the wall (-v) or, conversely, that low (relative to the mean) streamwise momentum (-u) is being moved away from the wall (+v). Similary, positive $\overline{uw}$ value means high (relative to the mean) streamwise momentum (+u) is being moved away from the centerline (+w) or, conversely, that low (relative to the mean) streamwise momentum (-u) is being moved towards the centerline (-w). Reynolds stress profiles clearly indicate that the the junction flow strongly modifies the Reynolds stress at X/C = 1, and its influence remains at X/C = 33. This, despite the fact that the turbulent kinetic energy for the freestream normalization shows almost a complete recovery.

The normalization of the Reynolds stress by the friction velocity presents an interesting potential connection. The $\overline{vw}$ Reynolds stress has an estimated peak value of -0.2. The $\overline{uw}$ Reynolds stress has an estimated peak of 0.3. The magnitude of each combined is 0.5, which is roughly the difference between the $\overline{uv}$ Reynolds stress peak and the undisturbed case. Thus, the $\overline{uw}$ and $\overline{vw}$ magnitudes closely match the difference in magnitude between the $\overline{uv}$ profiles and the $\overline{uv}$ undisturbed case. This suggests that the increased wall-ward transport of momentum is offset by spanwise transport in the developing wake.

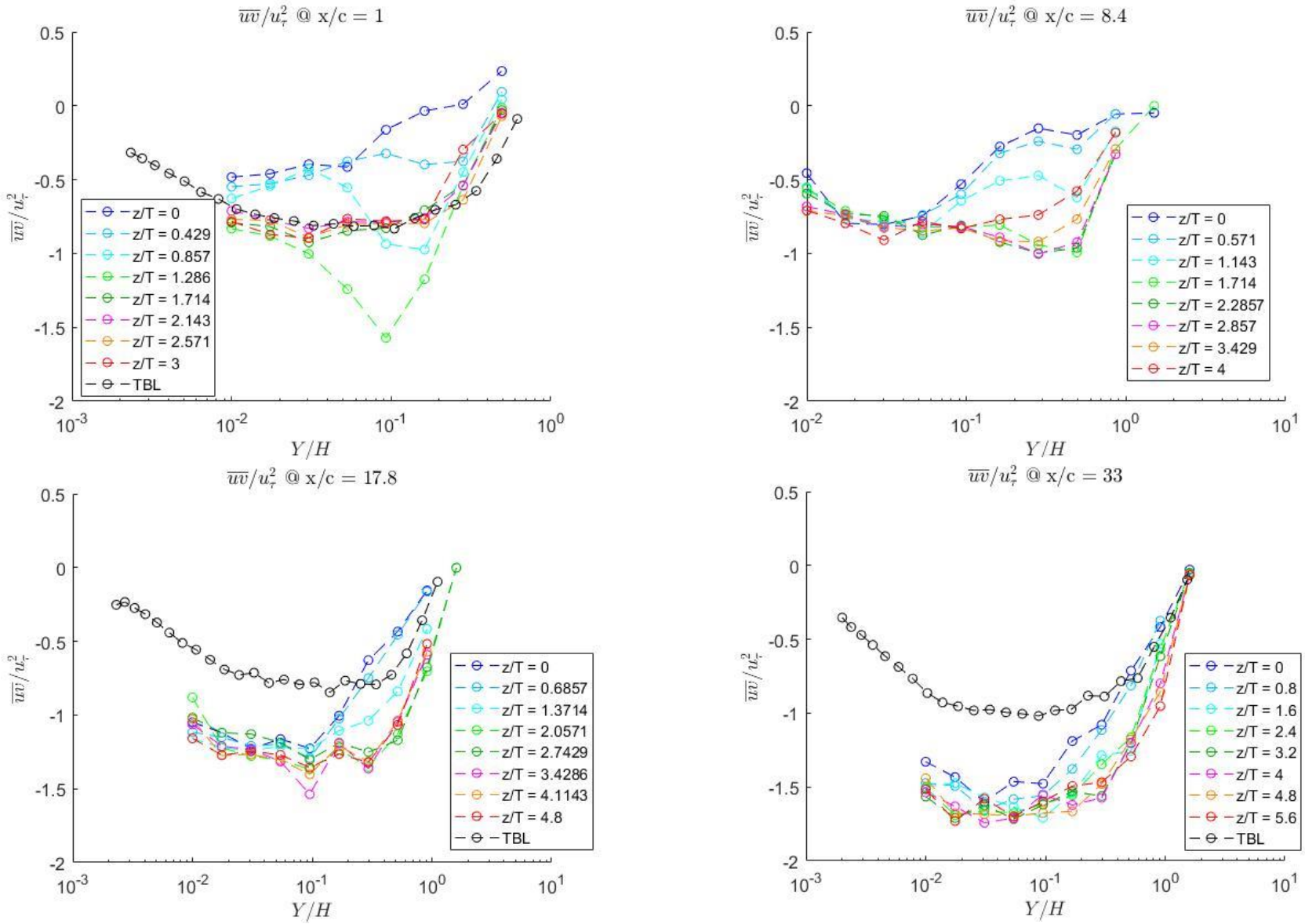

Figure 3.5.1: Reynolds stress $\overline{uv}$ normalized by u_τ at (a) X/C = 1 (b) X/C = 8.4 (c) X/C = 17.8 (d) X/C = 33.0 at spanwise locations z/T and undisturbed turbulent boundary layer (TBL)

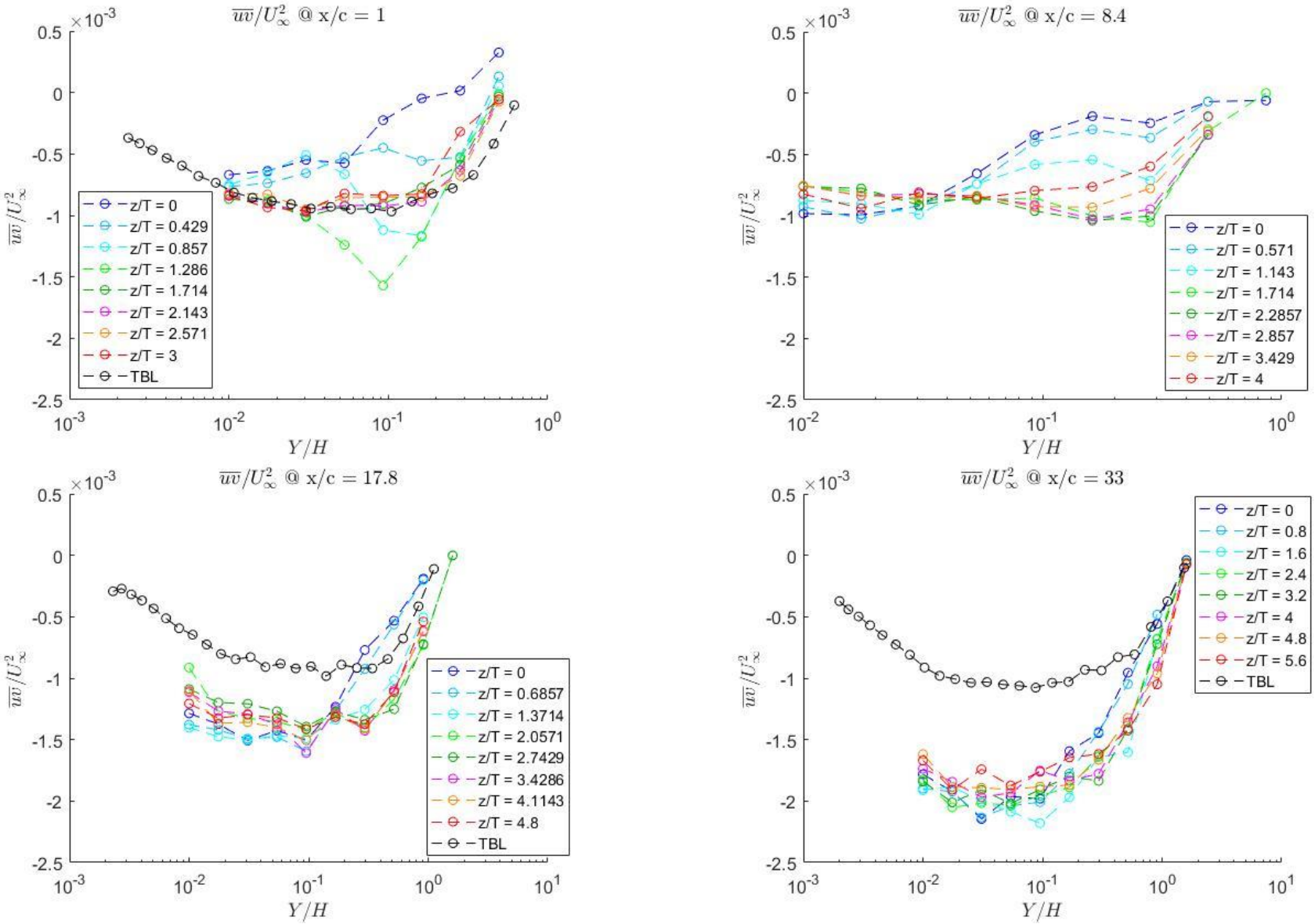

Figure 3.5.2: Reynolds stress $\overline{uv}$ normalized by U_∞ at (a) X/C = 1 (b) X/C = 8.4 (c) X/C = 17.8 (d) X/C = 33.0 at spanwise locations z/T and undisturbed turbulent boundary layer (TBL)

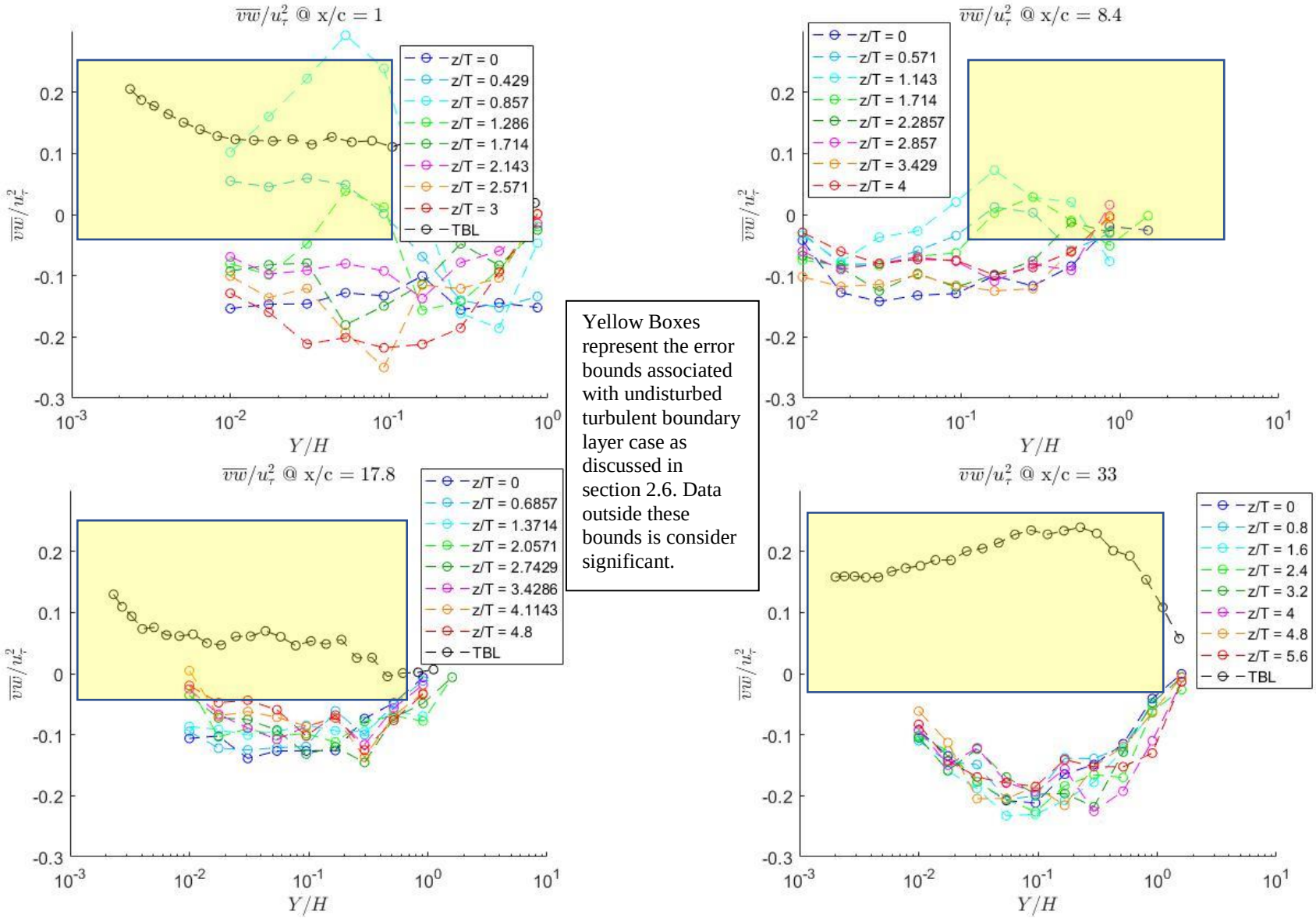

Yellow Boxes represent the error bounds associated with undisturbed turbulent boundary layer case as discussed in section 2.6. Data outside these bounds is consider significant.

Figure 3.5.3: Reynolds stress $\overline{vw}$ normalized by u_τ at (a) X/C = 1 (b) X/C = 8.4 (c) X/C = 17.8 (d) X/C = 33.0 at spanwise locations z/T and undisturbed turbulent boundary layer (TBL)

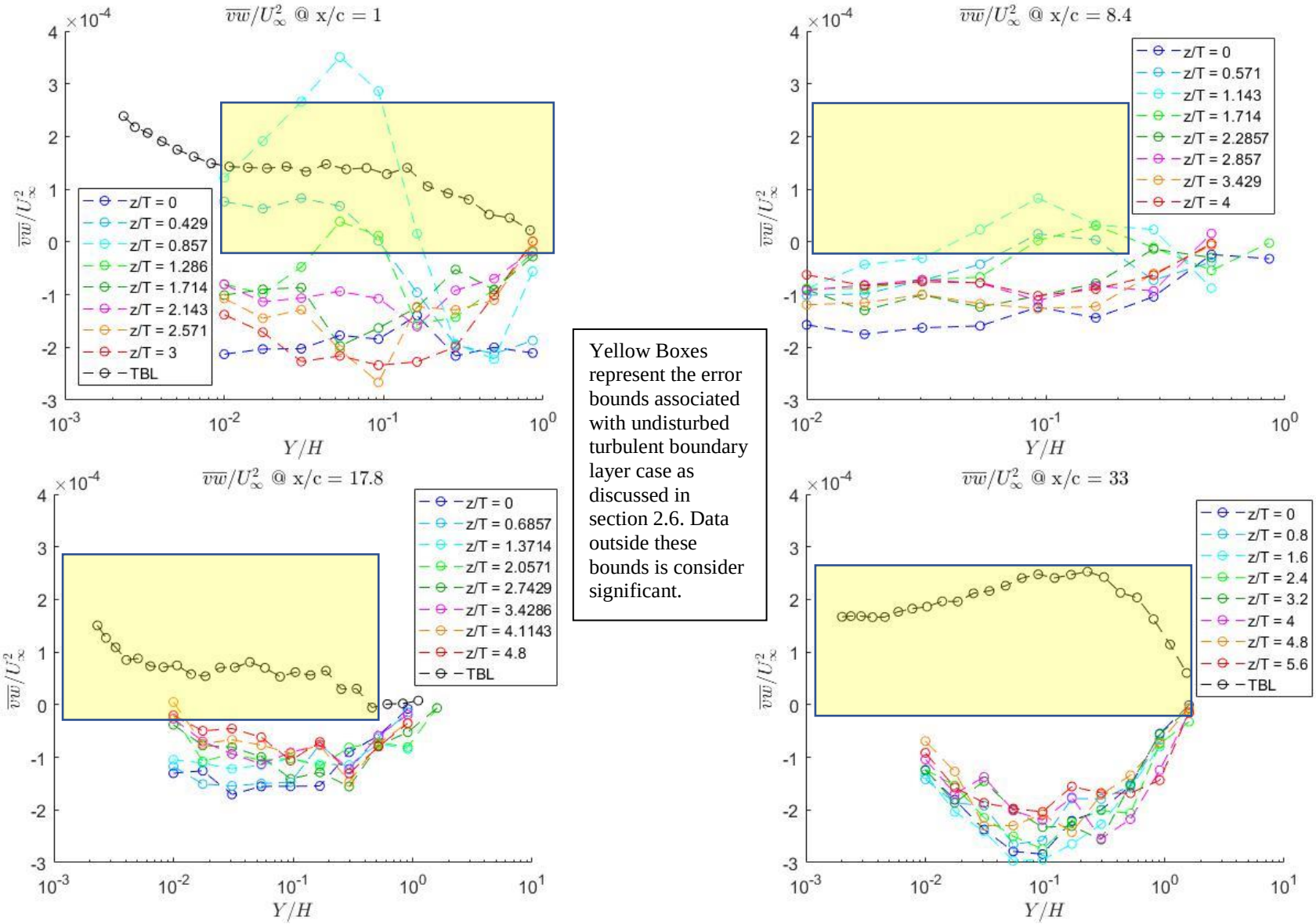

Yellow Boxes represent the error bounds associated with undisturbed turbulent boundary layer case as discussed in section 2.6. Data outside these bounds is consider significant.

Figure 3.5.4: Reynolds stress $\overline{vw}$ normalized by U_∞ at (a) X/C = 1 (b) X/C = 8.4 (c) X/C = 17.8 (d) X/C = 33.0 at spanwise locations z/T and undisturbed turbulent boundary layer (TBL)

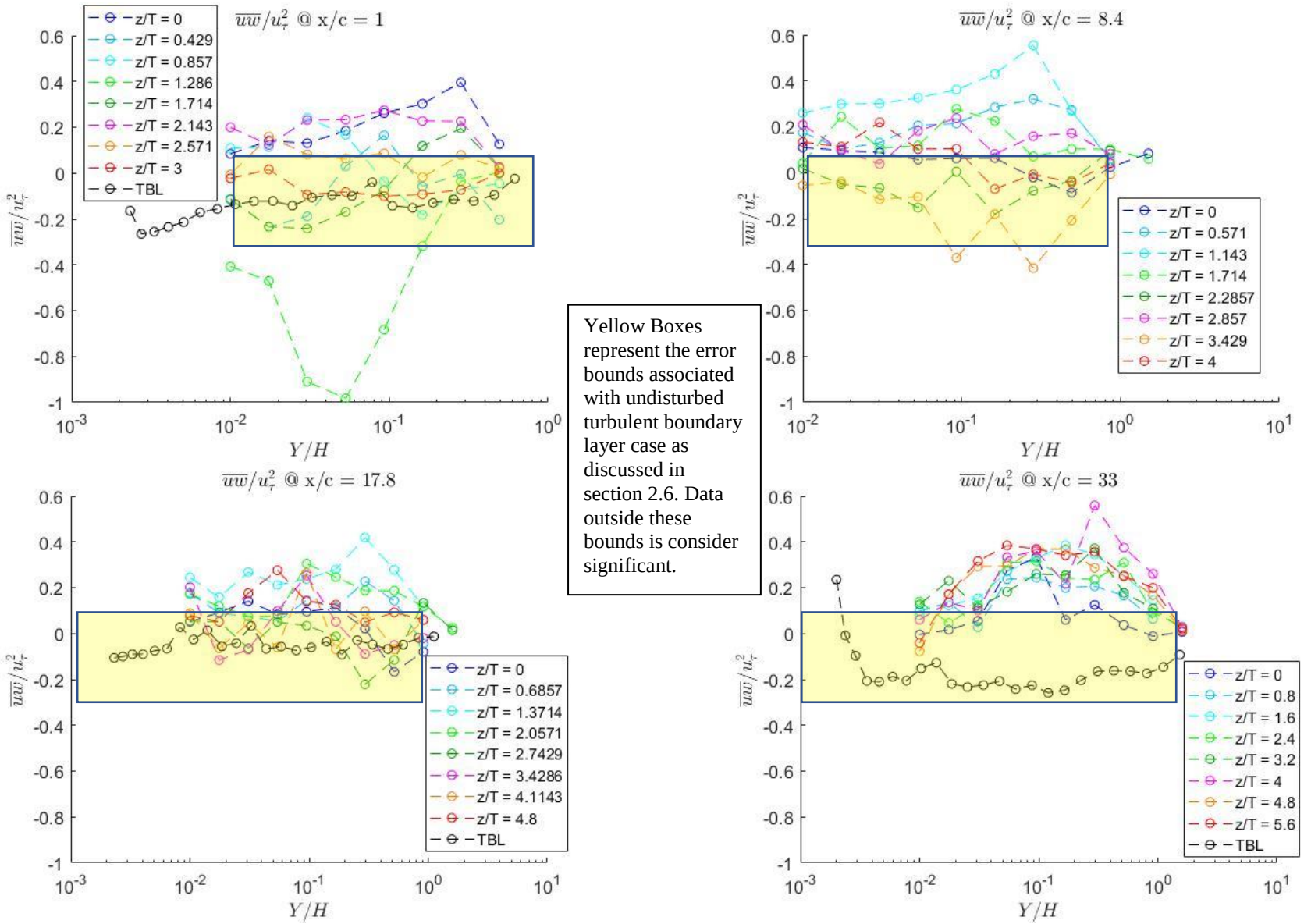

Yellow Boxes represent the error bounds associated with undisturbed turbulent boundary layer case as discussed in section 2.6. Data outside these bounds is consider significant.

Figure 3.5.5: Reynolds stress $\overline{uw}$ normalized by u_τ at (a) X/C = 1 (b) X/C = 8.4 (c) X/C = 17.8 (d) X/C = 33.0 at spanwise locations z/T and undisturbed turbulent boundary layer (TBL)

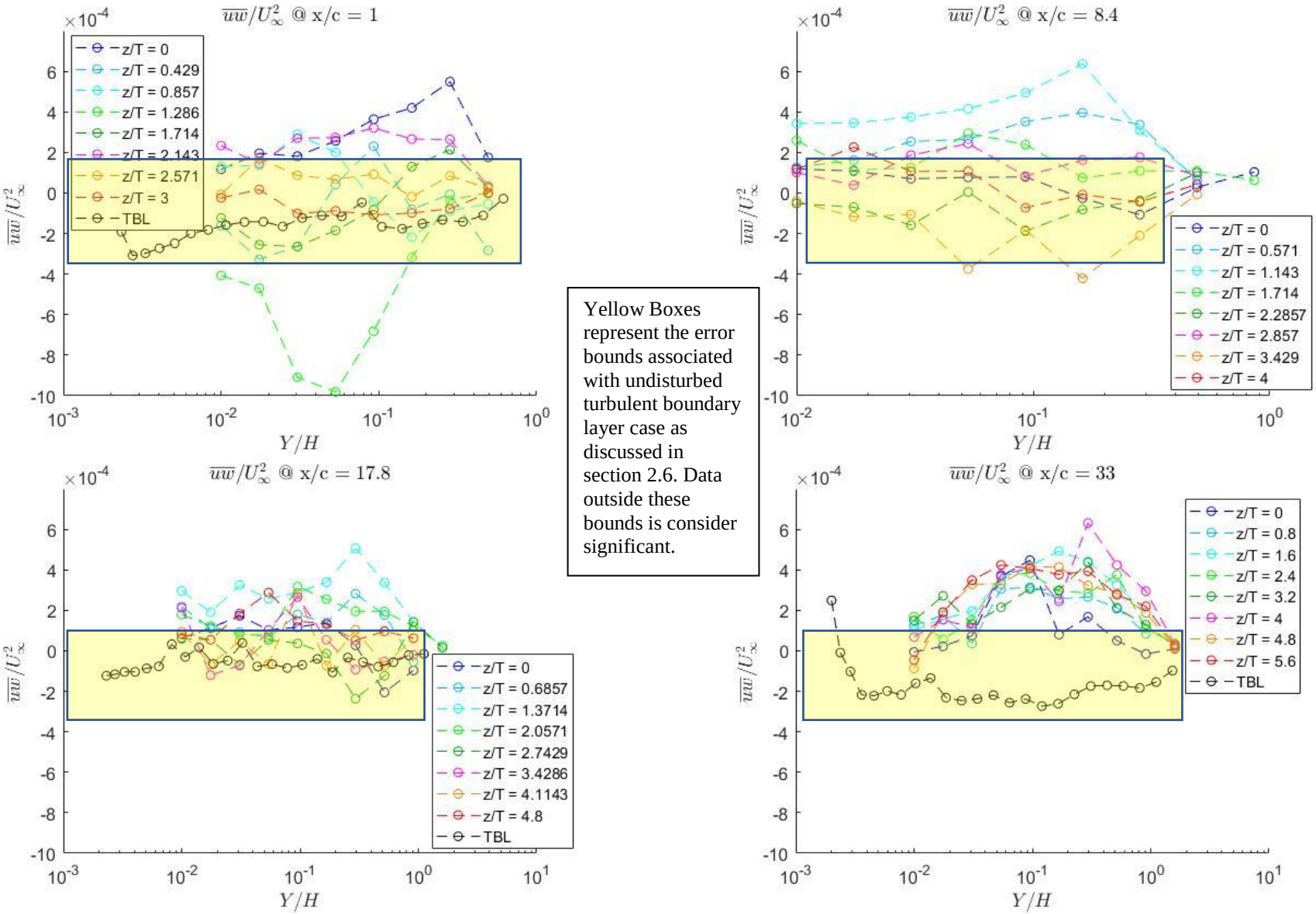

Yellow Boxes represent the error bounds associated with undisturbed turbulent boundary layer case as discussed in section 2.6. Data outside these bounds is consider significant.

Figure 3.5.6: Reynolds stress $\overline{uw}$ normalized by U_∞ at (a) X/C = 1 (b) X/C = 8.4 (c) X/C = 17.8 (d) X/C = 33.0 at spanwise locations z/T and undisturbed turbulent boundary layer (TBL)

3.6 Vorticity Measurements

Vorticity measurements were acquired only at the first two downstream measurement planes of X/C = 1 and 8.4. The vorticity variance was computed for all three components and normalized by kinematic viscosity and friction velocity, as well as by the freestream velocity and airfoil height. Wall-normal profiles of the vorticity variances, and enstrophy (i.e., square of the vorticity) were compared to the undisturbed turbulent boundary layer at X/C = 1. Figure 3.6.1 and 3.6.2 shows the inner normalized and outer normalized wall-normal profiles of the fluctuating vorticity for the eight spanwise locations.

The x-vorticity variance at X/C = 1 and for Y/H < 0.2 is distributed around the undisturbed case. Above Y/H ≈ 0.2, the profiles are above the undisturbed case. The points furthest from the wall for z/T ≤ 0.429, clearly are non-zero, which may be a signature of the to the wake over the top of the airfoil. The y-vorticity variance, z-vorticity variance, and enstrophy all show qualitatively similar results to the x-vorticity variance. At X/C = 8.4, the first point closest to the wall, and for the spanwise locations z/T ≤ 1.143, the vorticity variances and enstrophy are much larger than the profiles z/T > 1.143. The profiles, however, quickly converge with the other profiles within one wall-normal measurement. With increasing Y/H, the profiles remain grouped together but have a non-zero value at the freestream. This is true for all the vorticity variances and the enstrophy.

The outer normalized profiles have different trends, compared to the inner-normalized profiles at X/C = 1. Here the profiles are lower than the undisturbed case until Y/H ≈ 0. They then become greater than the undisturbed case. The spanwise profiles for z/T ≤ 0.429 have non-zero values at the freestream. The profiles are closely spaced, and no distinguishing features

between them can be seen. This is qualitatively similar for all the vorticity variance components and the enstrophy.

In general, the differences in the profiles of the vorticity variance are small between the junction flow and the undisturbed case. Owing to this lack of difference, it is most likely that large turbulent scales are primarily responsible for the non-equilibrium behaviors of the junction flow boundary layer development. A complete vorticity study successfully completed at all measurement planes would give further insight into this. Figure 3.6.3 and figure 3.6.4 show the inner and outer normalization of at X/C = 1 for the fairing case respectively. These are similar to the airfoil case.

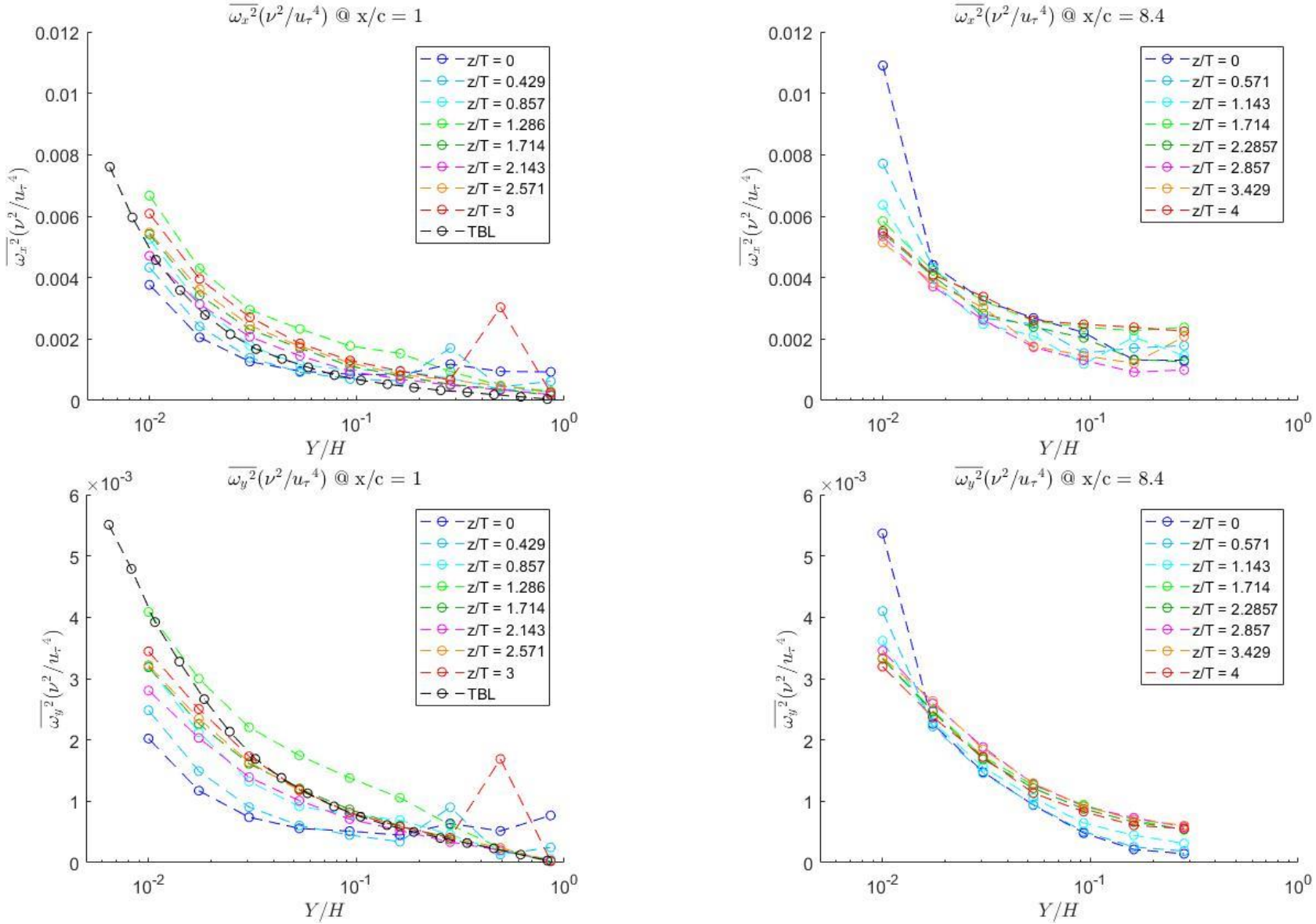

Figure 3.6.1: Inner normalized (a) X-Vorticity Variance X/C = 1(b) X-Vorticity Variance X/C = 8.4 (c) Y-Vorticity Variance X/C = 1 (d) Y-Vorticity Variance X/C = 8.4 at spanwise locations z/T and undisturbed turbulent boundary layer (TBL)

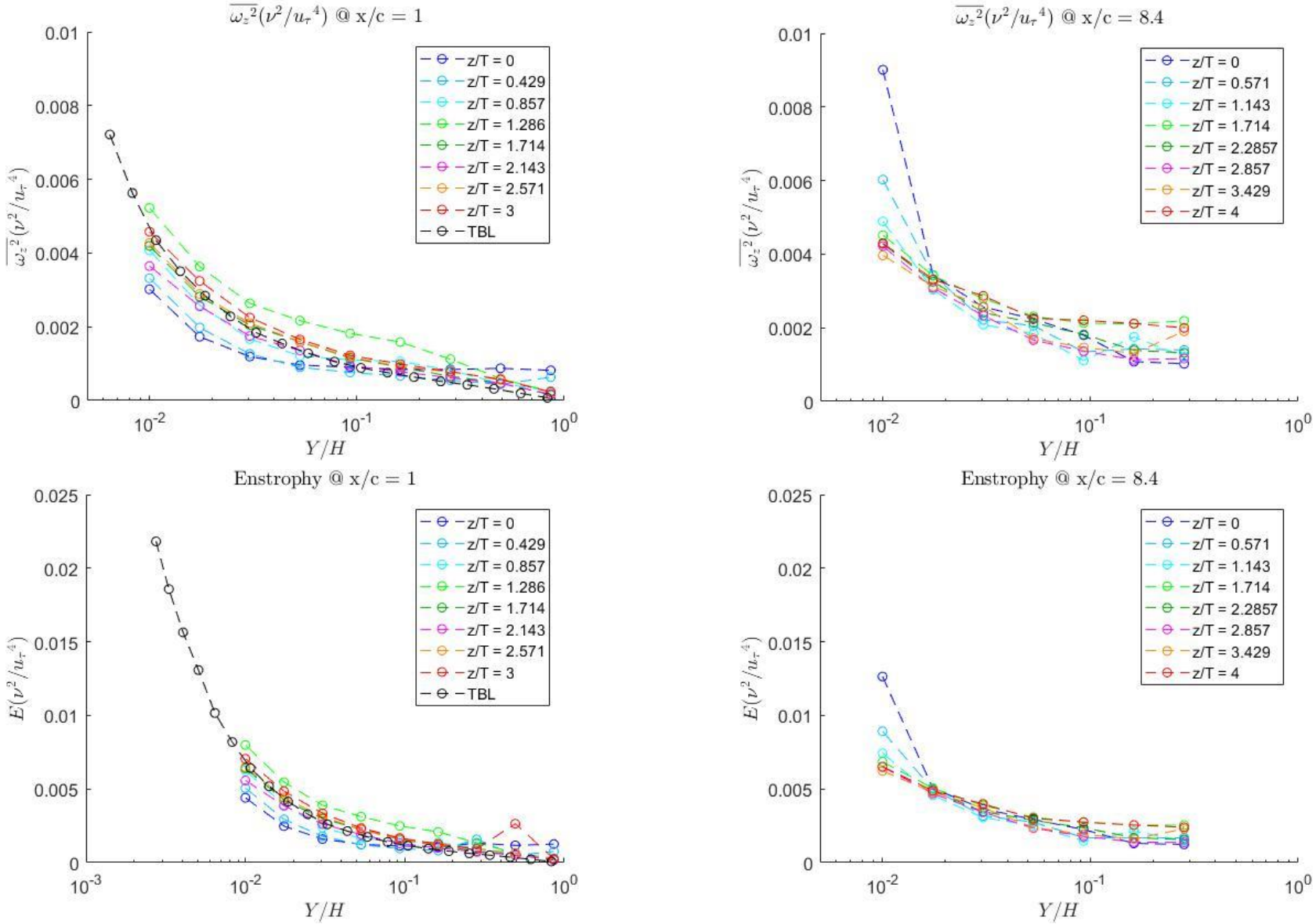

Figure 3.6.1: Inner normalized (e) Z-Vorticity Variance X/C = 1(f) Z-Vorticity Variance X/C = 8.4 (g) Enstrophy X/C = 1 (h) Enstrophy X/C = 8.4 at spanwise locations z/T and undisturbed turbulent boundary layer (TBL)

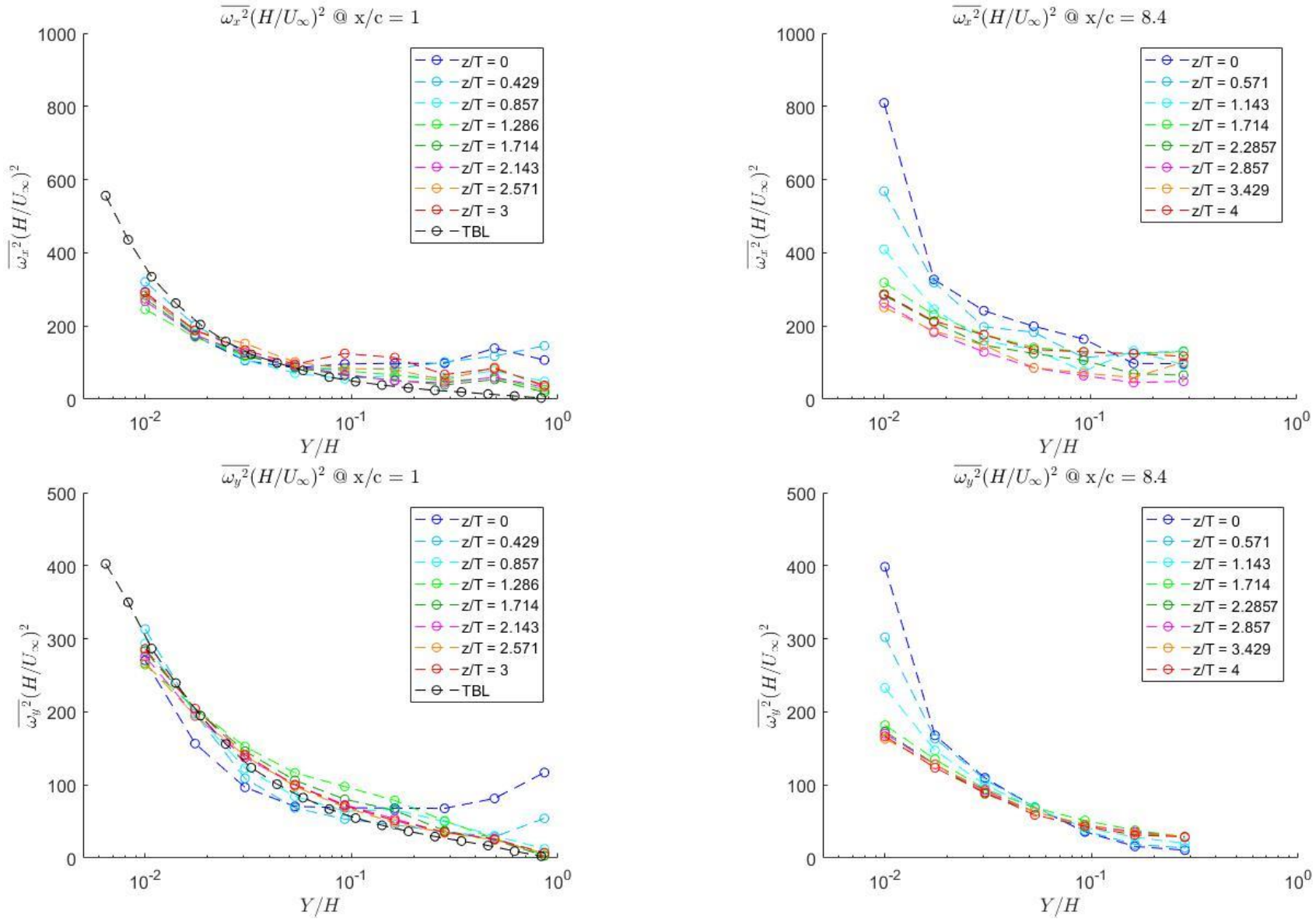

Figure 3.6.2: Outer normalized (a) X-Vorticity Variance X/C = 1(b) X-Vorticity Variance X/C = 8.4 (c) Y-Vorticity Variance X/C = 1 (d) Y-Vorticity Variance X/C = 8.4 at spanwise locations z/T and undisturbed turbulent boundary layer (TBL)

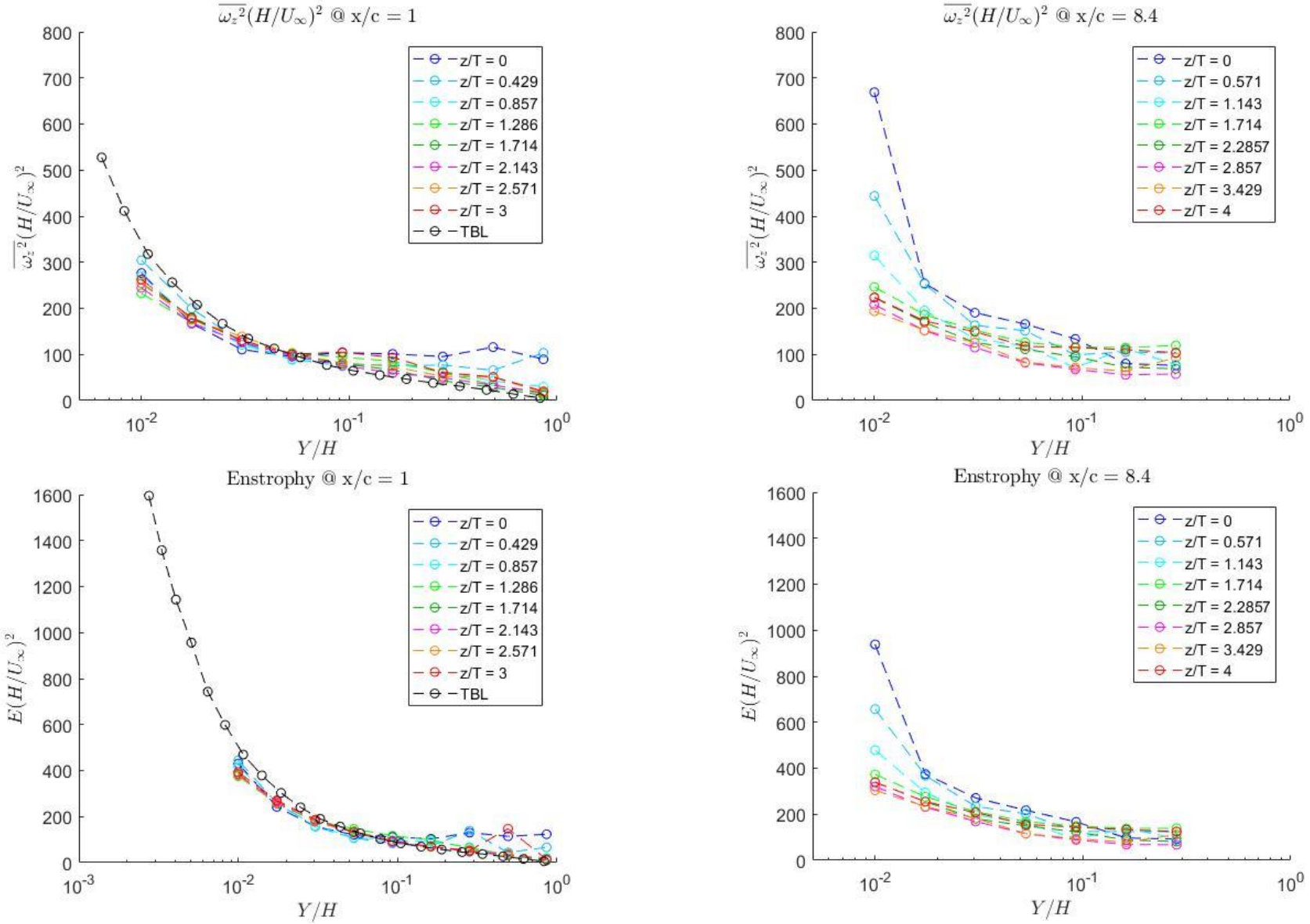

Figure 3.6.2: Outer normalized (e) Z-Vorticity Variance X/C = 1(f) Z-Vorticity Variance X/C = 8.4 (g) Enstrophy X/C = 1 (h) Enstrophy X/C = 8.4 at spanwise locations z/T and undisturbed turbulent boundary layer (TBL)

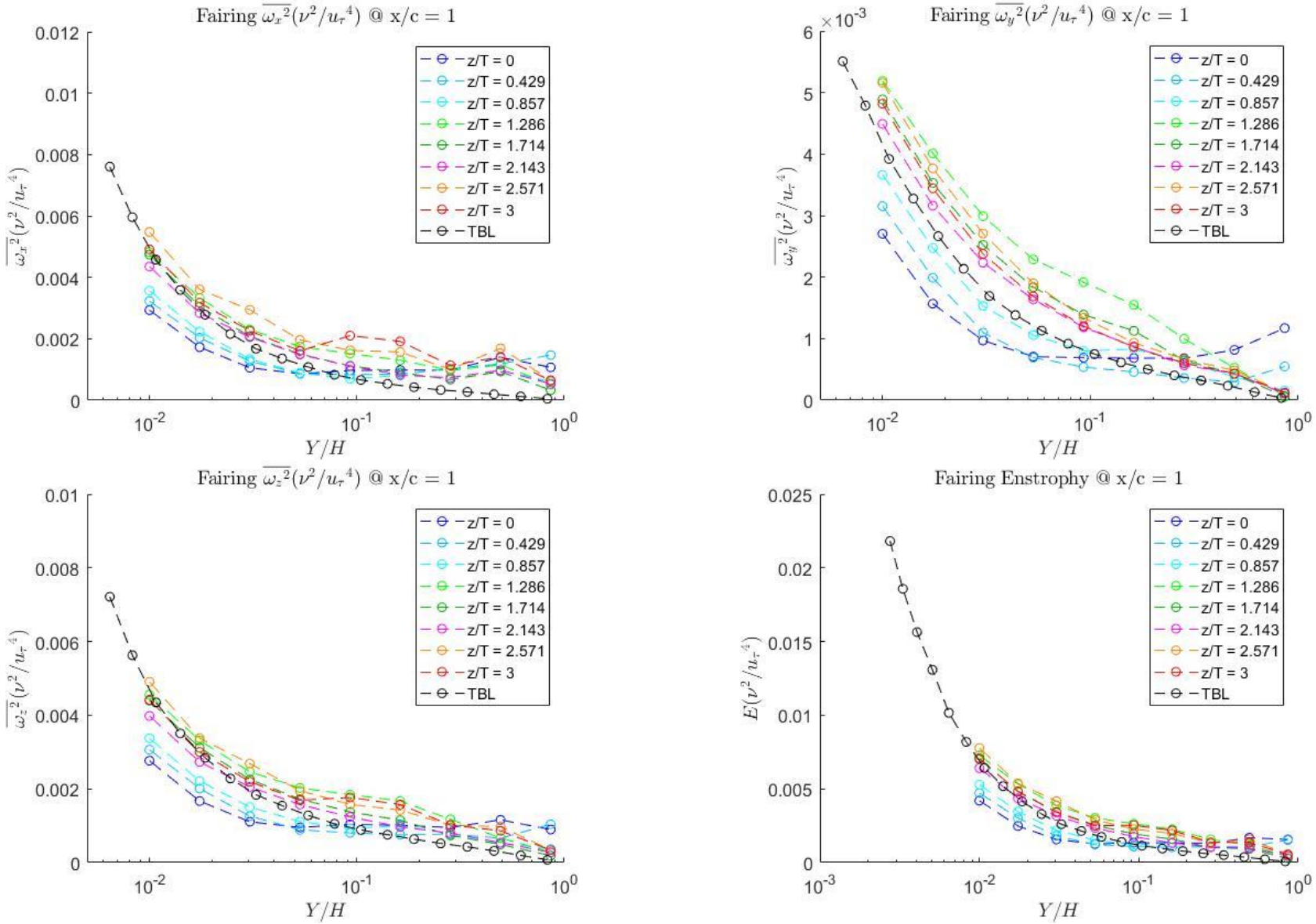

Figure 3.6.3: Fairing inner normalized (a) X-Vorticity Variance X/C = 1 (b) Y-Vorticity Variance X/C = 1 (c) Z-Vorticity Variance X/C = 1 (d) Enstrophy X/C = 1 at spanwise locations z/T and undisturbed turbulent boundary layer (TBL)

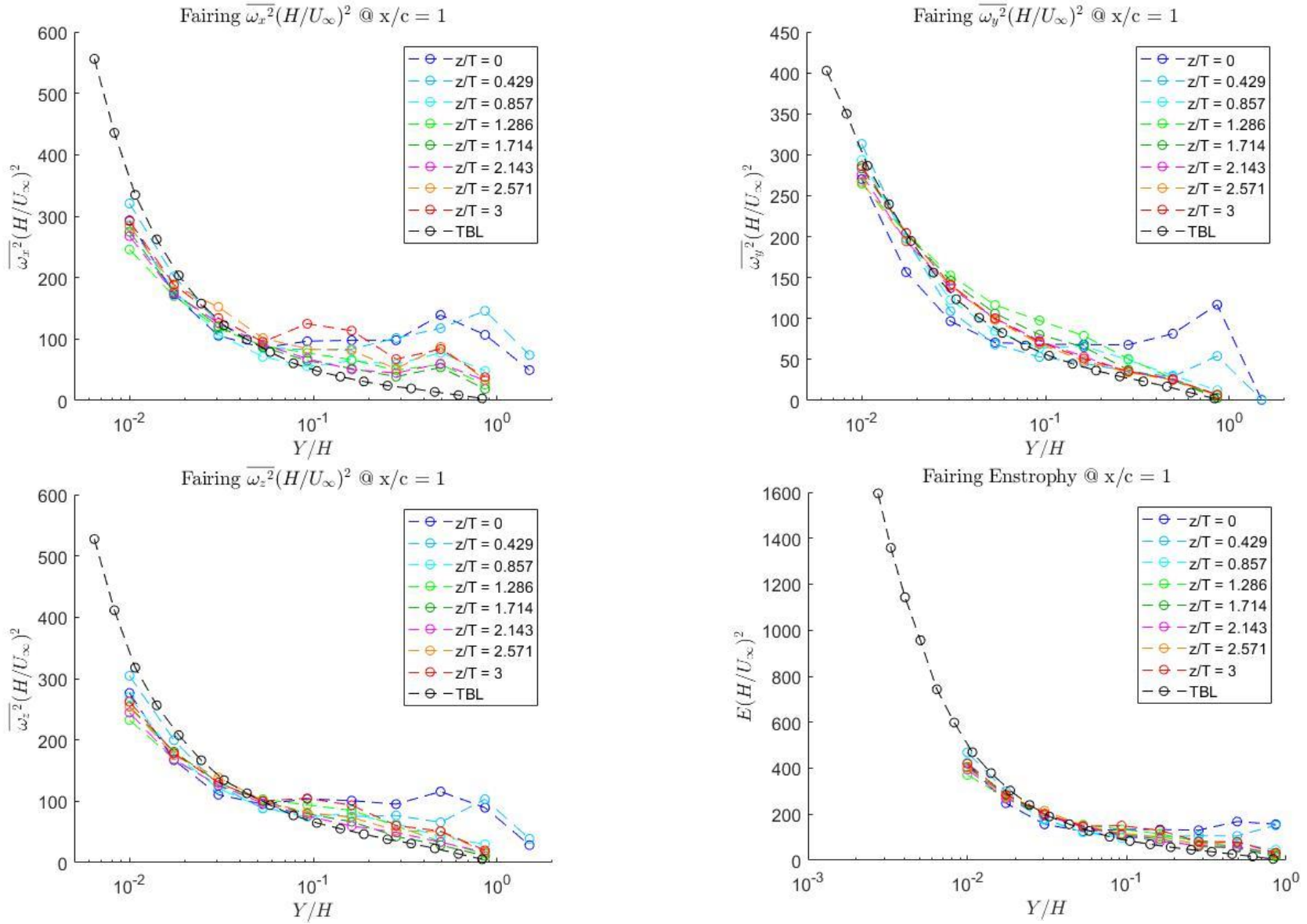

Figure 3.6.4: Fairing inner normalized (a) X-Vorticity Variance X/C = 1 (b) Y-Vorticity Variance X/C = 1 (c) Z-Vorticity Variance X/C = 1 (d) Enstrophy X/C =1 at spanwise locations z/T and undisturbed turbulent boundary layer (TBL)

3.7 Spectral Observations

Spectra were calculated at z/T = 0 for the four measurement planes and for all wall-normal positions. The spectra were calculated using a Hanning window with 50% overlap with ensemble averaging. The spectra were then processed by a custom smoothing function to eliminate peaks. The spectra were then normalized by the airfoil height, H, and friction velocity, u_τ. Measurement planes X/C = 1, 17.8, 33 will be discussed while X/C = 8.4 is provided in the appendix. The spectra are compared to the undisturbed case to evaluate the effect of the airfoil.

The streamwise velocity spectra are shown in figure 3.7.1, 3.7.2 and 3.7.3 for X/C = 1, 17.8 and 33 respectively. The spectra at X/C =1 are qualitatively similar to the undisturbed case. Subtle but notable differences are that near the wall, the airfoil spectra fall below undisturbed spectra at low frequency. Moving further from the wall, there appears to be a cross-over in the spectra at Y > 0.4298m. At X/C = 17.8 some low frequency variability exists most notably at Y = 0.0477m and 0.1473m. At Y = 0.4551m the airfoil case is lower than the undisturbed case for all frequencies. At X/C = 33 there is some variability but nothing notable except at Y = 0.4551m where again, the airfoil case is lower than the undisturbed case for all frequencies.

The wall-normal velocity spectra at X/C = 1, 17.8, and 33 are shown in figure 3.7.4, 3.7.5 and 3.7.6. There is no significant variability at X/C = 1 until Y = 0.1411m and 0.2463m where the airfoil case is higher at low frequencies. At Y = 0.4298m the airfoil case is higher for all frequencies. At X/C = 17.8 there is low frequency variability throughout in which the airfoil case tends to be higher than the undisturbed case. At Y = 0.1473m and 0.4551m, the airfoil case is lower for almost all frequencies. At X/C = 33 the low-frequency variability remains with the airfoil case being larger than the undisturbed case. For Y ≥ 0.1473m the low frequency

variability is less significant and close to the undisturbed case. The high frequencies also show some variability with the airfoil case being lower than the undisturbed case.

The spanwise velocity spectra at X/C = 1, 17.8, and 33 are shown in figure 3.7.7, 3.7.8 and 3.7.9. There is low frequency variability at X/C = 1, most notably at Y = 0.0152m and 0.0463m where the airfoil case is below the undisturbed case. At Y = 0.1411m the low frequencies for the airfoil case are below the undisturbed case, but at high frequencies, the airfoil case is above the undisturbed case. At Y = 0.4298m the airfoil case is above the undisturbed case for all frequencies. At X/C = 17.8 there exist some low frequency variability between the airfoil and undisturbed case. At Y = 0.4551m the airfoil case is lower at all frequencies. X/C = 33 has similar qualitative results to X/C = 17.8. The locations not noted are similar to the undisturbed case for all three velocity spectra.

The spectra indicate that the low frequency motions are modified by the boundary layer interaction with the airfoil. The streamwise spectra show less energy at low frequencies and more energy at higher frequencies. This is recovered downstream to match the undisturbed case. The wall-normal spectra at X/C = 1 is only affected at wall-normal positions above y = 0.15m in which the low frequencies have higher energy. The development downstream shows a shift in which the low frequencies have more energy and the high frequencies have less energy, compared to the undisturbed case. The spanwise spectra show little differences, and those that do exist are at low frequencies. The final wall-normal position for each velocity spectra is significantly modified. The energy at all the frequencies is either higher or lower than the undisturbed case. This is close to the height of the airfoil in which the wake effects could be modifying the flow.

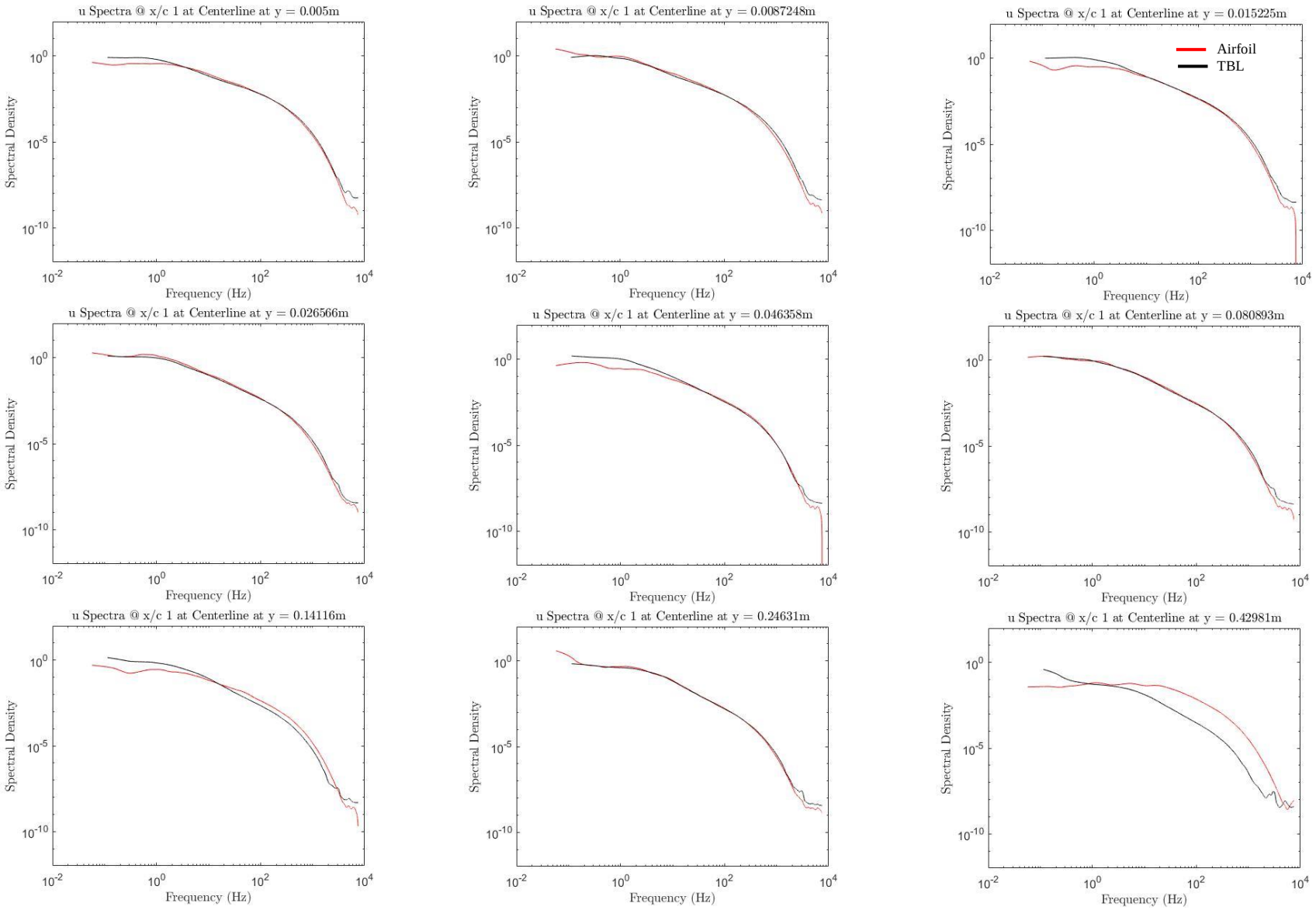

Figure 3.7.1: Streamwise velocity spectra normalized H/u_τ^3 at the centerline at X/C = 1 for airfoil and undisturbed turbulent boundary layer (TBL)

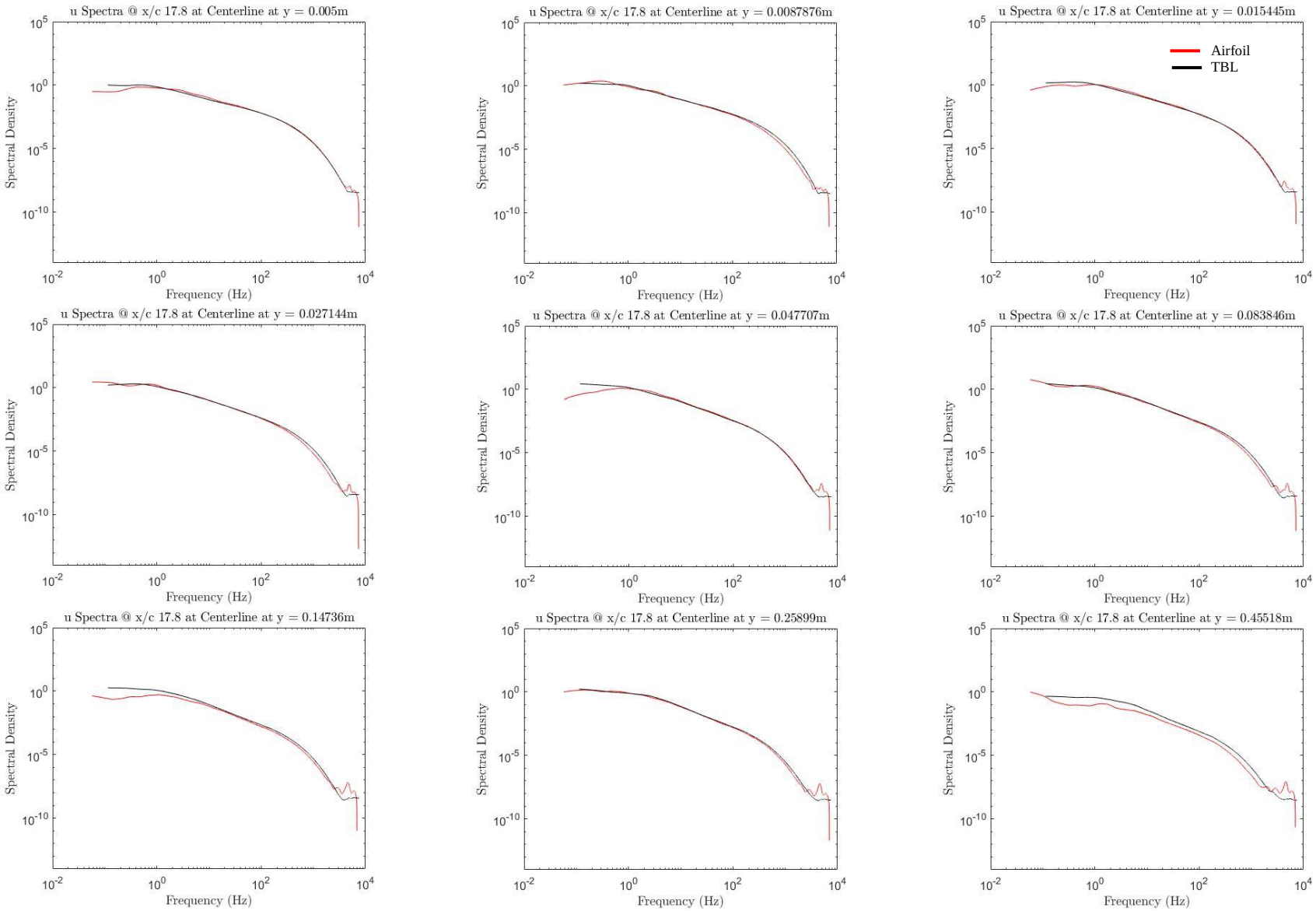

Figure 3.7.2: Streamwise velocity spectra normalized H/u_τ^3 at the centerline at X/C = 17.8 for airfoil and undisturbed turbulent boundary layer (TBL)

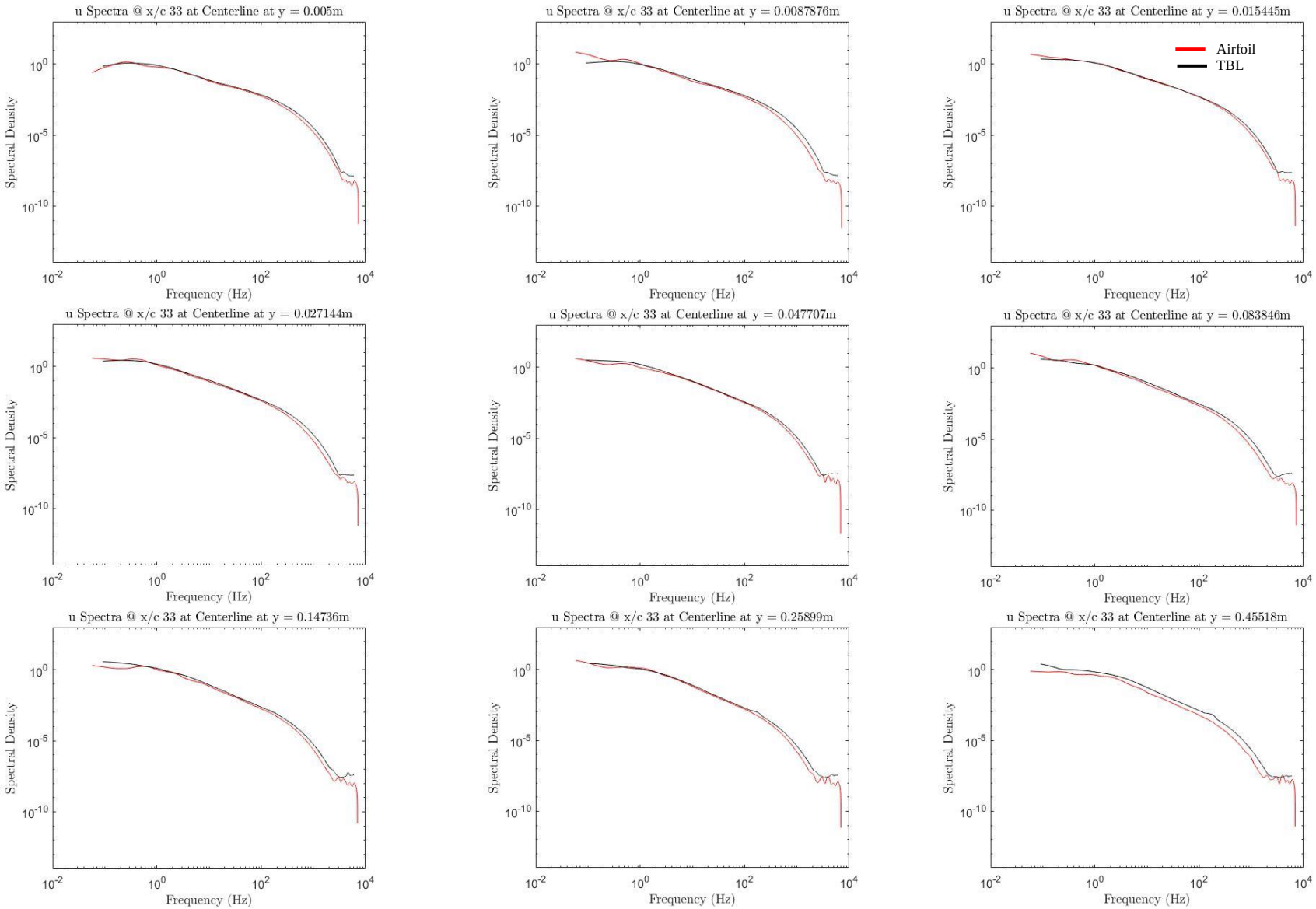

Figure 3.7.3: Streamwise velocity spectra normalized H/u_τ^3 at the centerline at X/C = 33 for airfoil and undisturbed turbulent boundary layer (TBL)

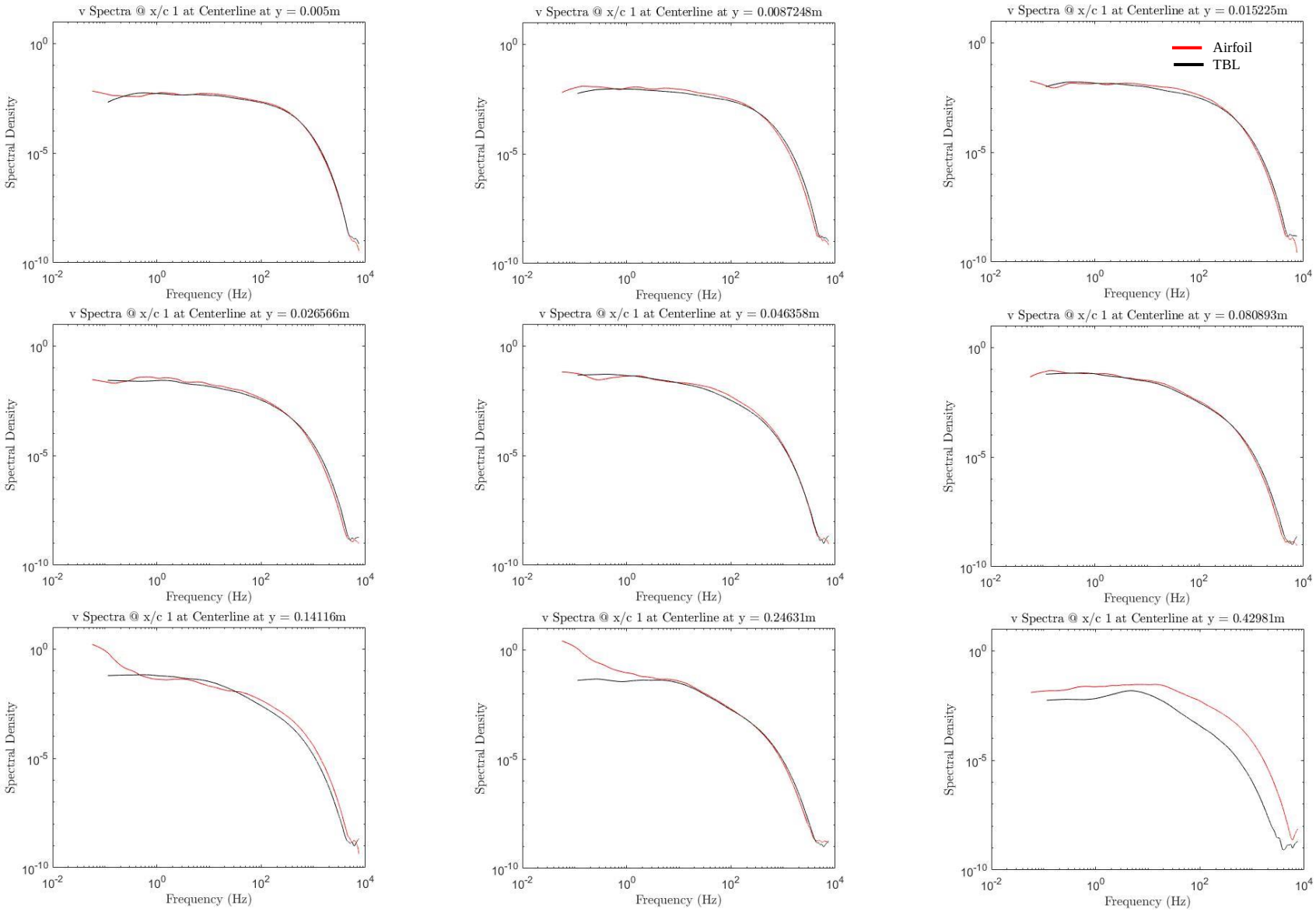

Figure 3.7.4: Wall-normal velocity spectra normalized H/u_τ^3 at the centerline at X/C = 1 for airfoil and undisturbed turbulent boundary layer (TBL)

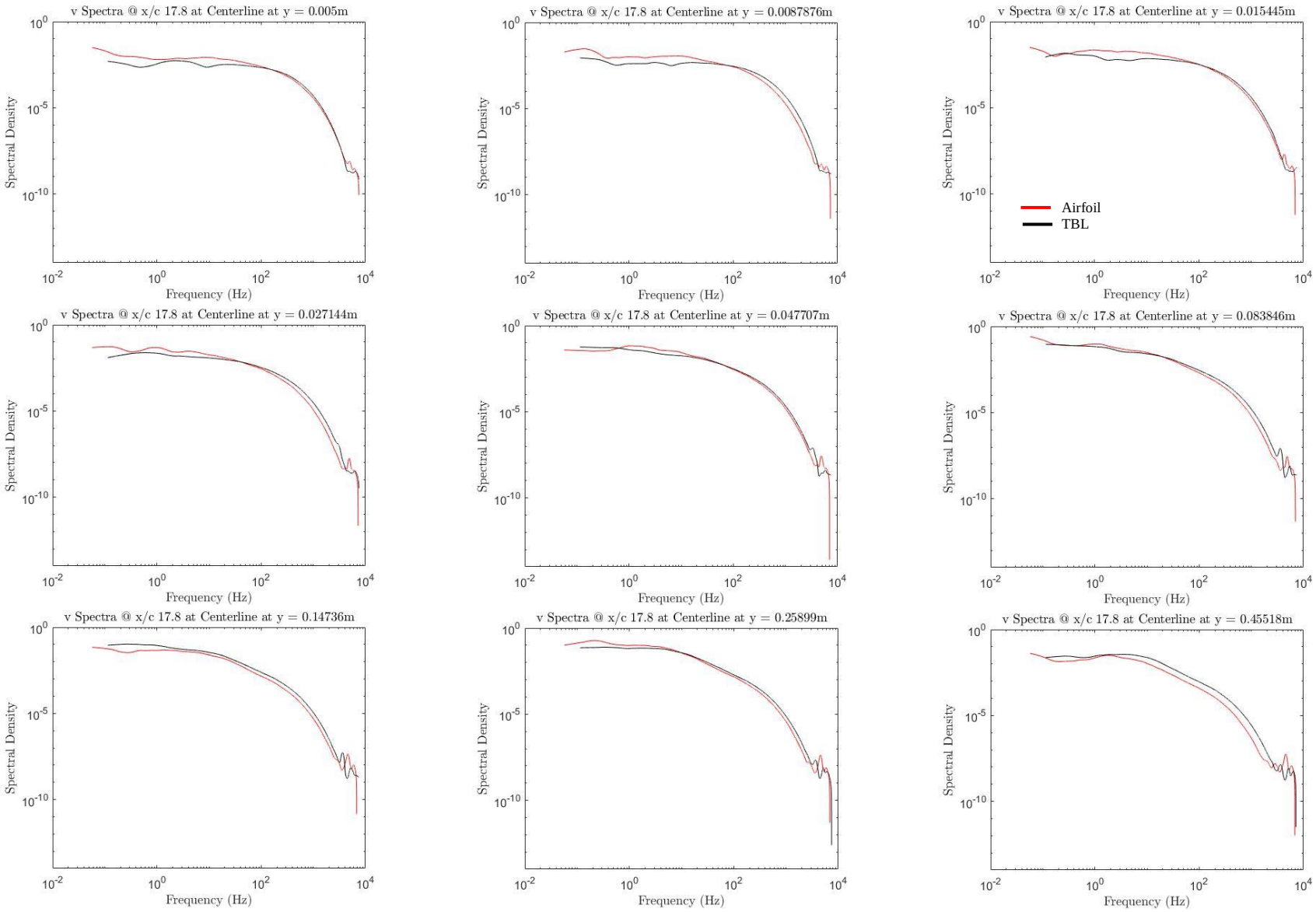

Figure 3.7.5: Wall-normal velocity spectra normalized H/u_τ^3 at the centerline at X/C = 17.8 for airfoil and undisturbed turbulent boundary layer (TBL)

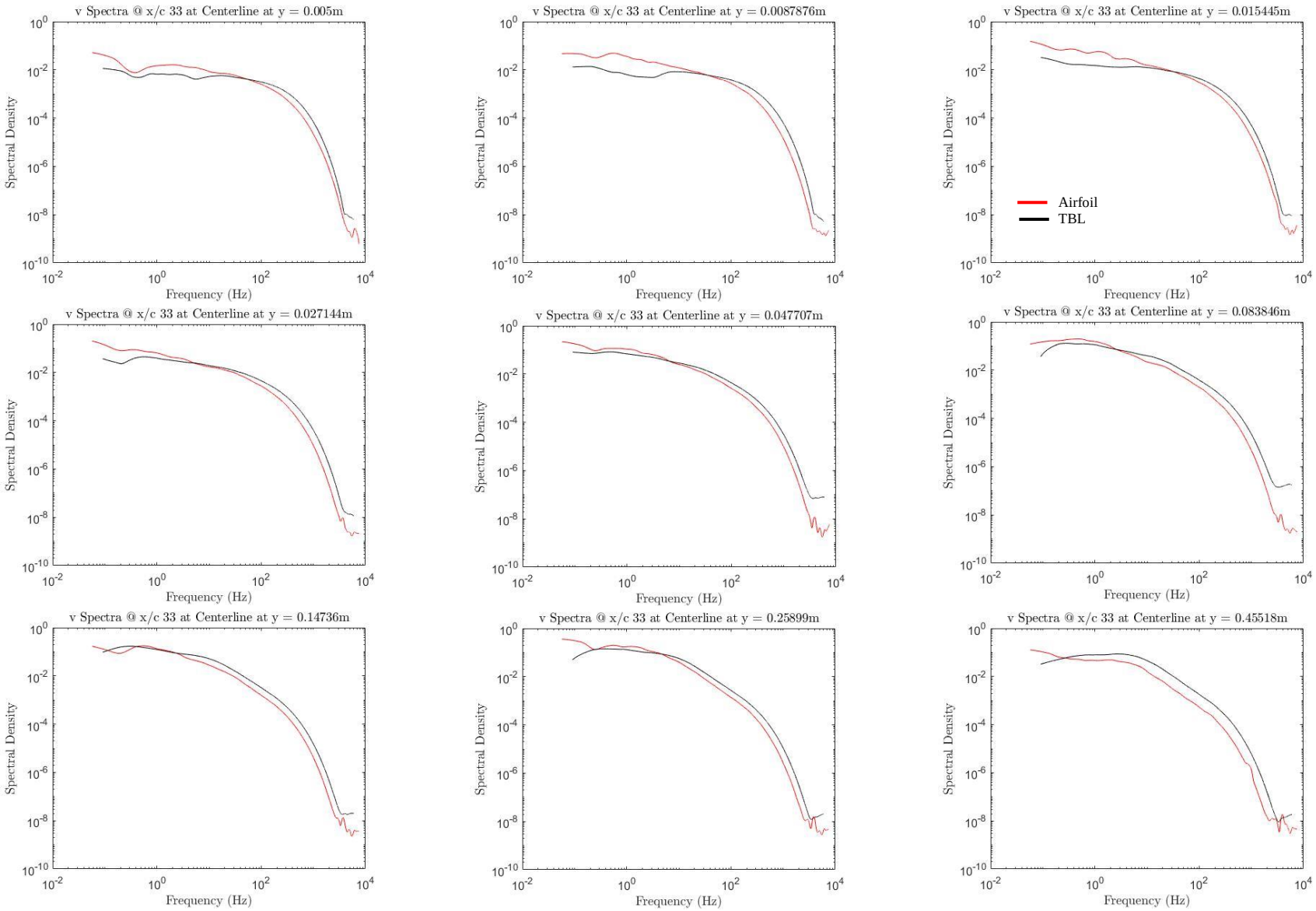

Figure 3.7.6: Wall-normal velocity spectra normalized H/u_τ^3 at the centerline at X/C = 33 for airfoil and undisturbed turbulent boundary layer (TBL)

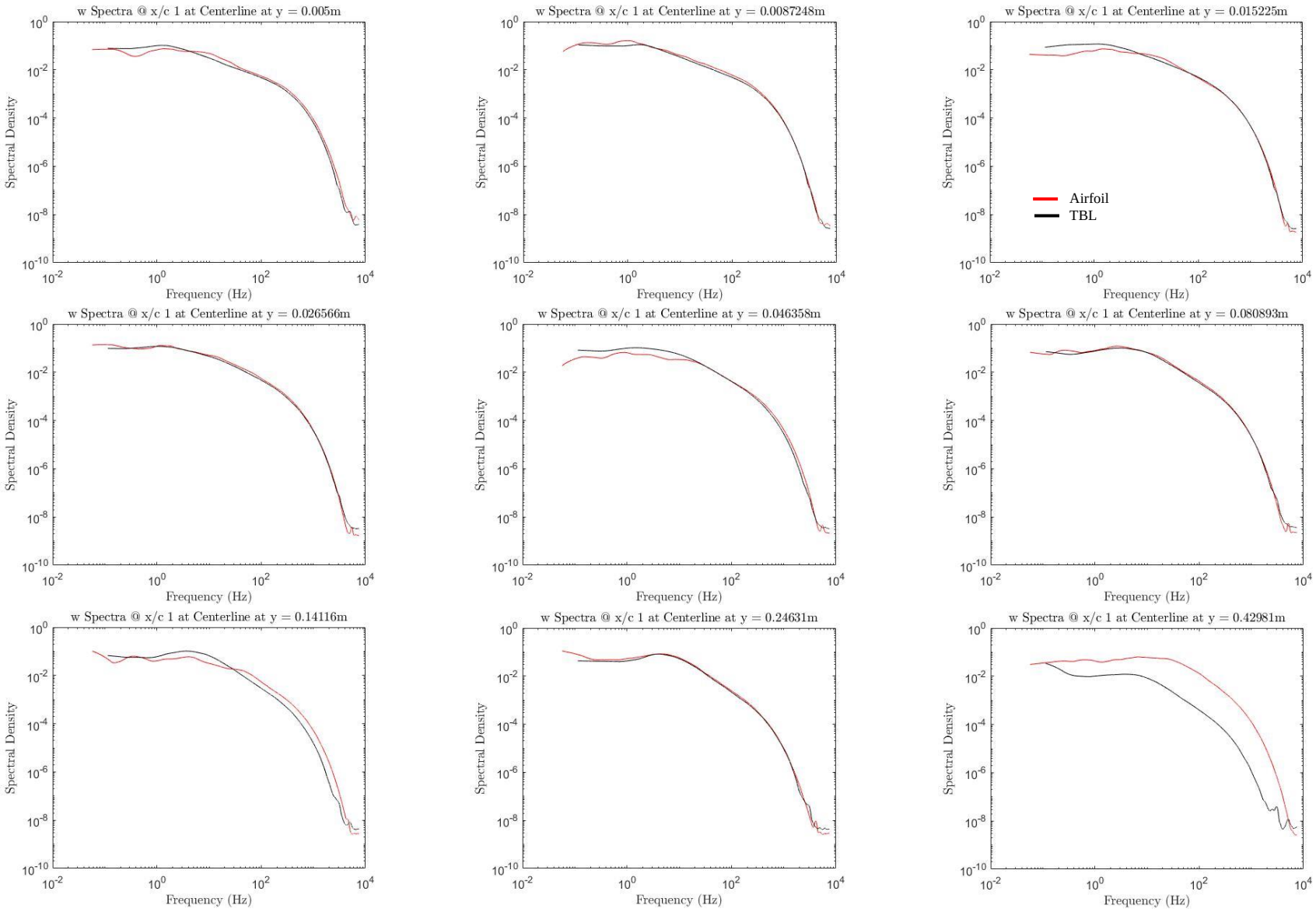

Figure 3.7.7: Spanwise velocity spectra normalized H/u_τ^3 at the centerline at X/C = 1 for airfoil and undisturbed turbulent boundary layer (TBL)

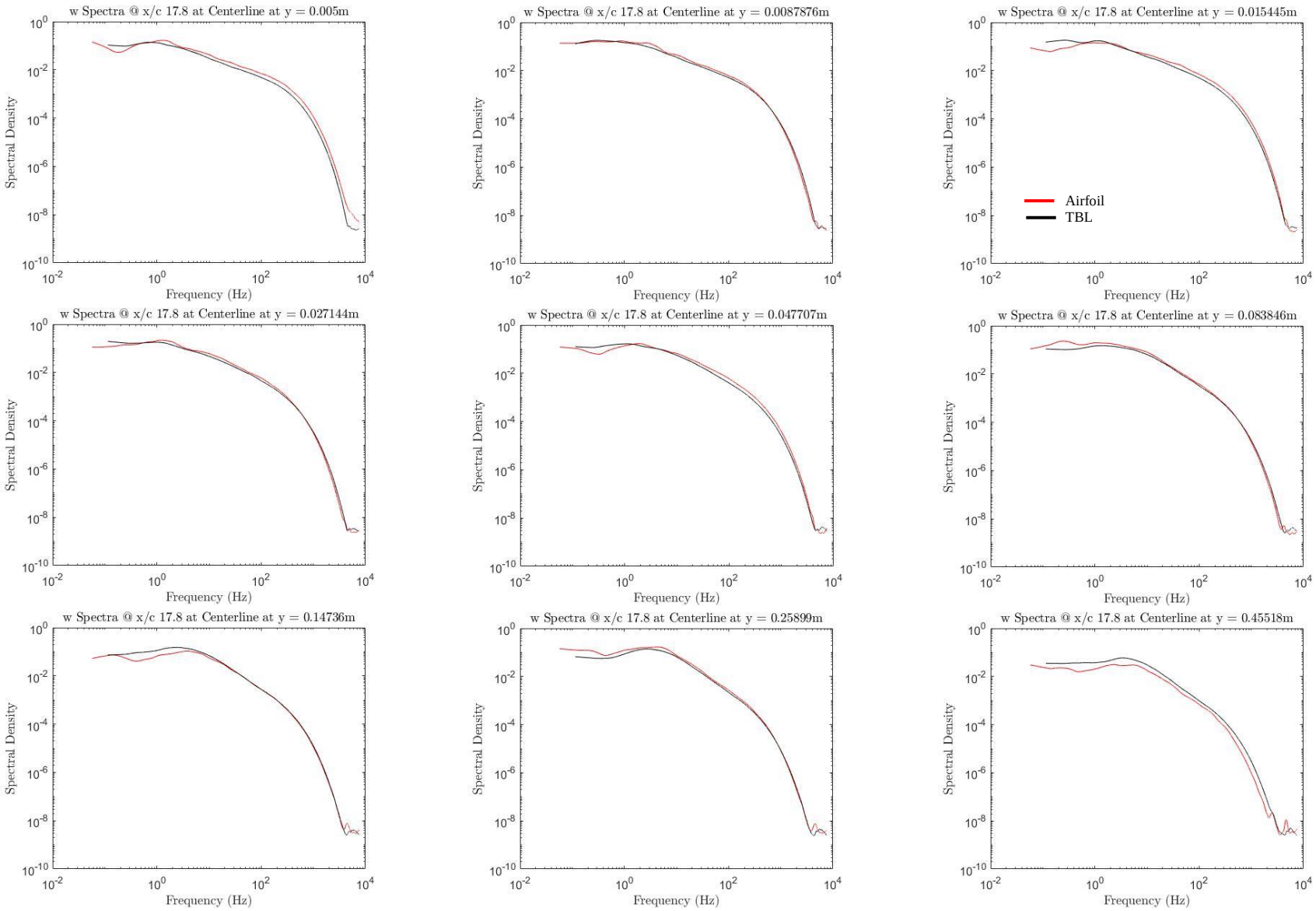

Figure 3.7.8: Spanwise velocity spectra normalized H/u_τ^3 at the centerline at X/C = 17.8 for airfoil and undisturbed turbulent boundary layer (TBL)

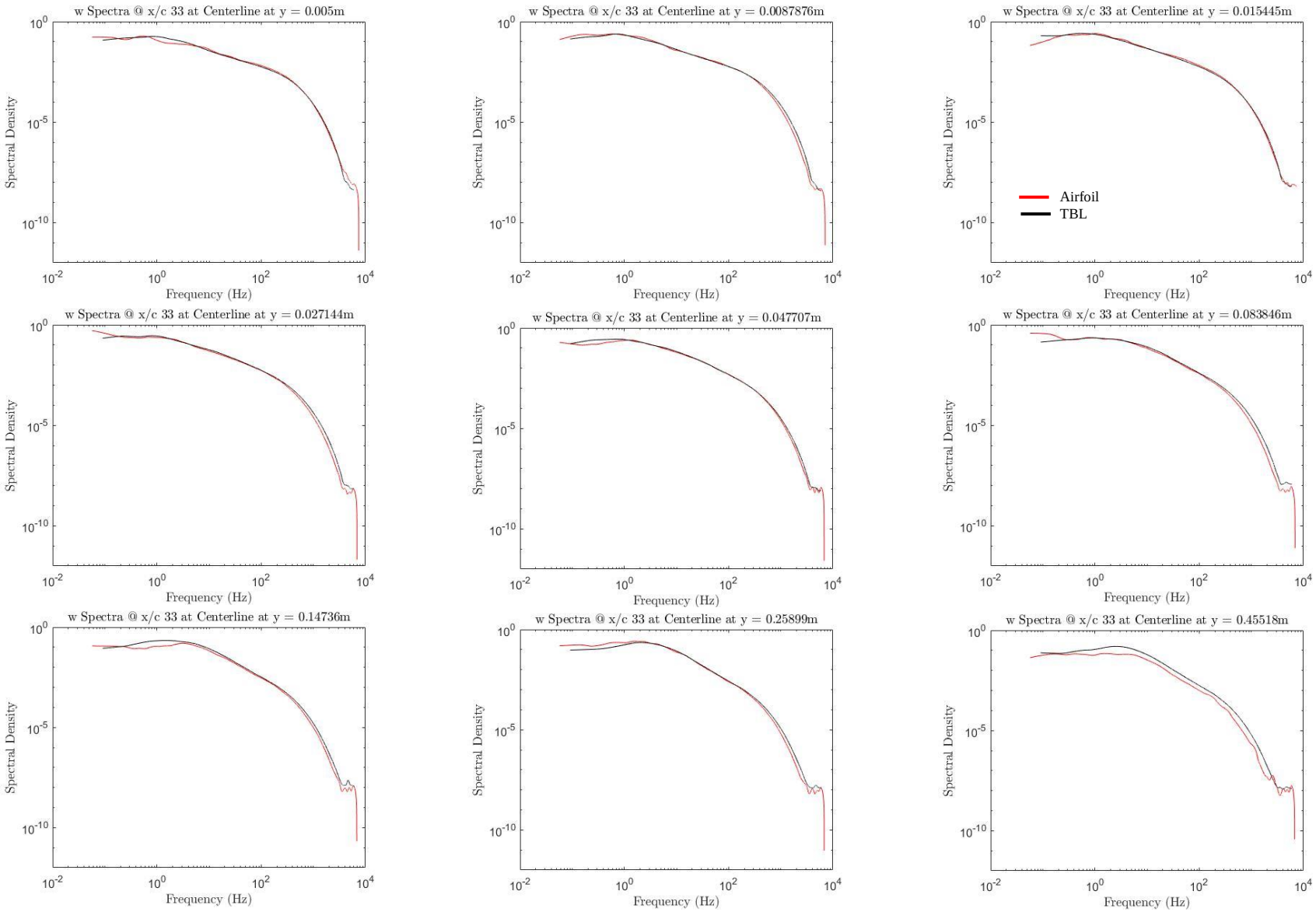

Figure 3.7.9: Spanwise velocity spectra normalized H/u_τ^3 at the centerline at X/C = 33 for airfoil and undisturbed turbulent boundary layer (TBL)

3.8 Fairing Comparison

The same set of experiments were performed with a simple fairing added to the airfoil. The full results of the fairing are given in the appendix with both normalizations by friction velocity and freestream velocity. The differences between the airfoil and the airfoil with the fairing are compared in this section. The comparison is made by plotting the inner normalized fairing data with an asterisk for the fairing case and circles for the non-fairing case. For clarity, only half of the spanwise profiles are plotted together. Therefore, for each statistic, there are even profiles and odd profiles. The even profiles are composed of the even number spanwise location of 2 to 8 while the odd profiles are composed of the odd number spanwise locations of 1 to 7. The even profiles will be used with the odd profiles contained in the appendix.

The streamwise mean velocity profiles are shown in figure 3.8.1. The profiles at X/C = 1 show that the fairing has slightly higher values at locations away from the wall for spanwise profiles $z/T \leq 1.286$. The other spanwise profiles are similar to each other. At X/C = 8.4 the differences are smaller. The profiles at X/C = 17.8 and 33 show very little difference between the two cases except that at X/C = 17.8 the non-fairing case has values that are slightly higher than the fairing. It is worthy of noting that like the non-fairing case at X/C = 17.8 there is a kink in the fairing profiles. The streamwise mean velocity for the fairing tends to be higher at X/C = 1 and 8.4. At X/C = 17.8 the non-fairing case is slightly higher. They become similar at X/C = 33.

The streamwise velocity variance is shown in figure 3.8.2. At X/C = 1 the peak of the non-fairing case is larger. The spanwise profiles at $z/T \geq 2.143$ are similar to each other while the other spanwise profiles for the non-fairing case are larger. At X/C = 8.4 the fairing case is now higher for all spanwise locations. This remains true for the remaining measurement planes.

Unlike the mean streamwise velocity, the streamwise variance is not the same in the final measurement plane.

The wall-normal variance shows similar trends to the streamwise velocity variance. Figure 3.8.3 and figure 3.8.4 show both the odd and even profiles. They are both plotted to show the double peak associated with the wall-normal variance. At X/C = 1 the non-fairing case has larger values for both peaks. At X/C = 8.4 both odd and even profiles show the fairing case is now slightly higher, but very similar to the non-fairing case. The profiles at X/C = 17.8 show the fairing case is larger for all profiles. The profiles at X/C = 33 show that all the profiles are very similar.

The spanwise velocity variance in figure 3.8.5 shows that the non-fairing case is higher than the airfoil case. The profiles between the two cases then become similar to each other at X/C = 8.4. Slight differences are observed at X/C = 17.8 where the non-fairing case is higher at $Y/H \leq 0.1$. Turbulent kinetic energy is shown in figure 3.8.6. The TKE shows qualitatively similar trends to the velocity variances. At X/C = 1 the non-fairing case is higher, but at X/C = 33 the fairing case is slightly higher.

Collectively, the measured profiles show that at X/C = 1 the profiles for the fairing case are generally above the non-fairing case. Then as the flow develops downstream there is a cross-over and, the fairing case becomes slightly larger. At X/C = 33 the mean streamwise velocity is similar, but the velocity variances and TKE still have some slight differences. Thus, inconclusive results are observed. The coarse measurement plane could miss the complete effect from the junction. In either case, the fairing does not prevent leading edge separation or the horseshoe vortex from forming. This supports the primary conclusion of Devenport et al. [10].

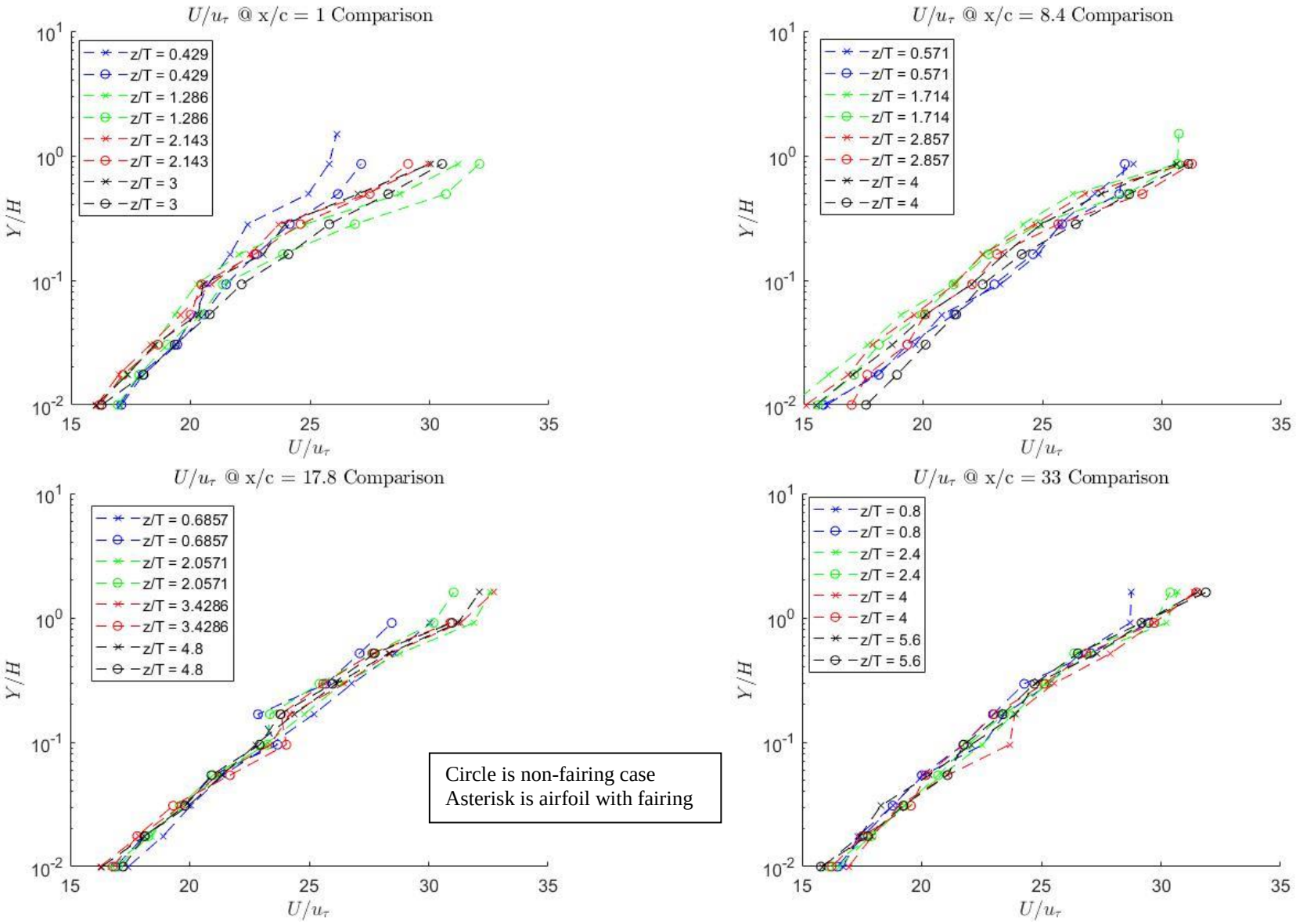

Figure 3.8.1: Fairing and non-fairing streamwise velocity comparison for even spanwise location at (a) X/C = 1 (b) X/C = 8.4 (c) X/C = 17.8 (d) X/C = 33.0

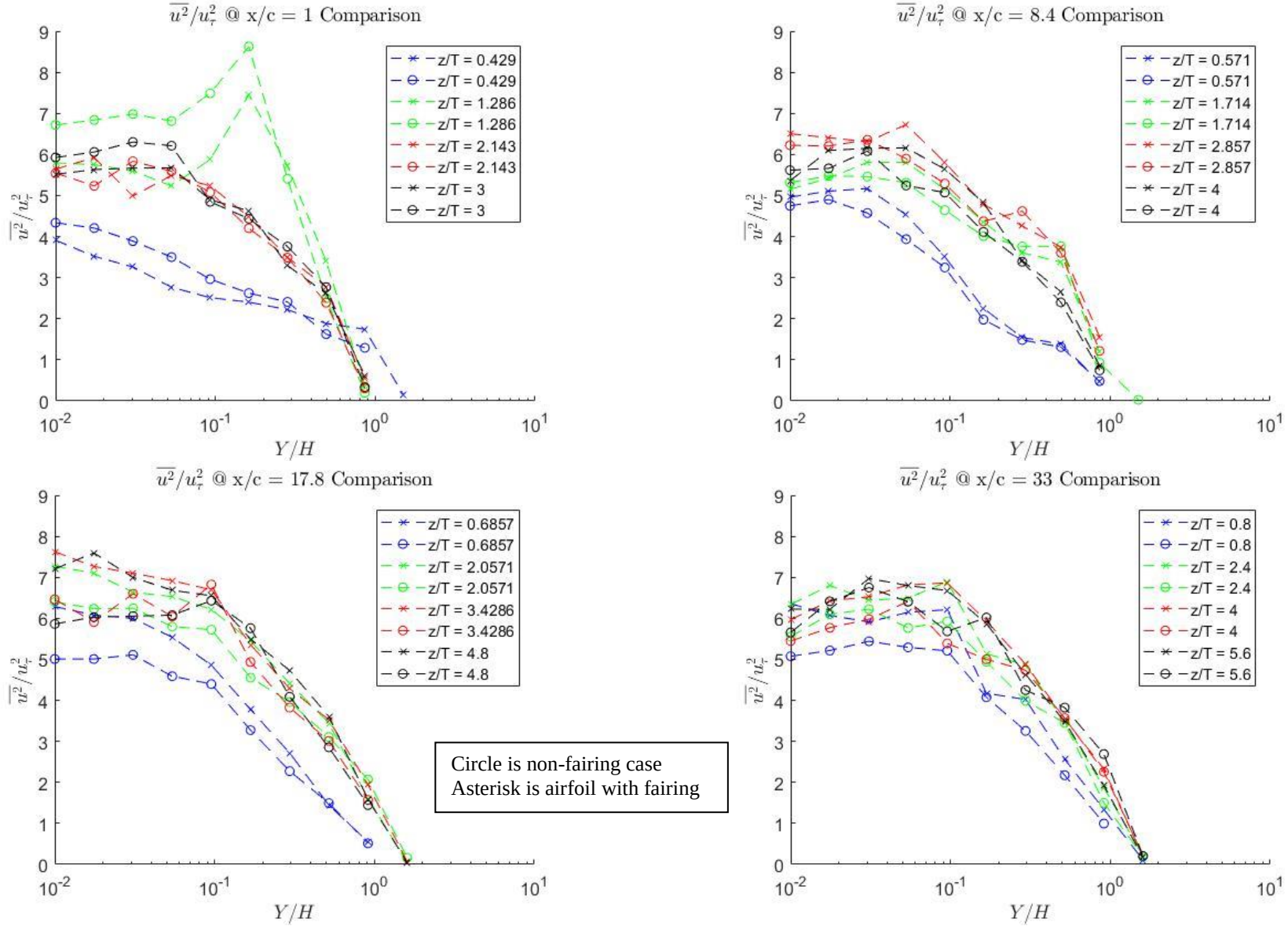

Figure 3.8.2: Fairing and non-fairing streamwise velocity variance comparison for even spanwise location at (a) X/C = 1 (b) X/C = 8.4 (c) X/C = 17.8 (d) X/C = 33.0

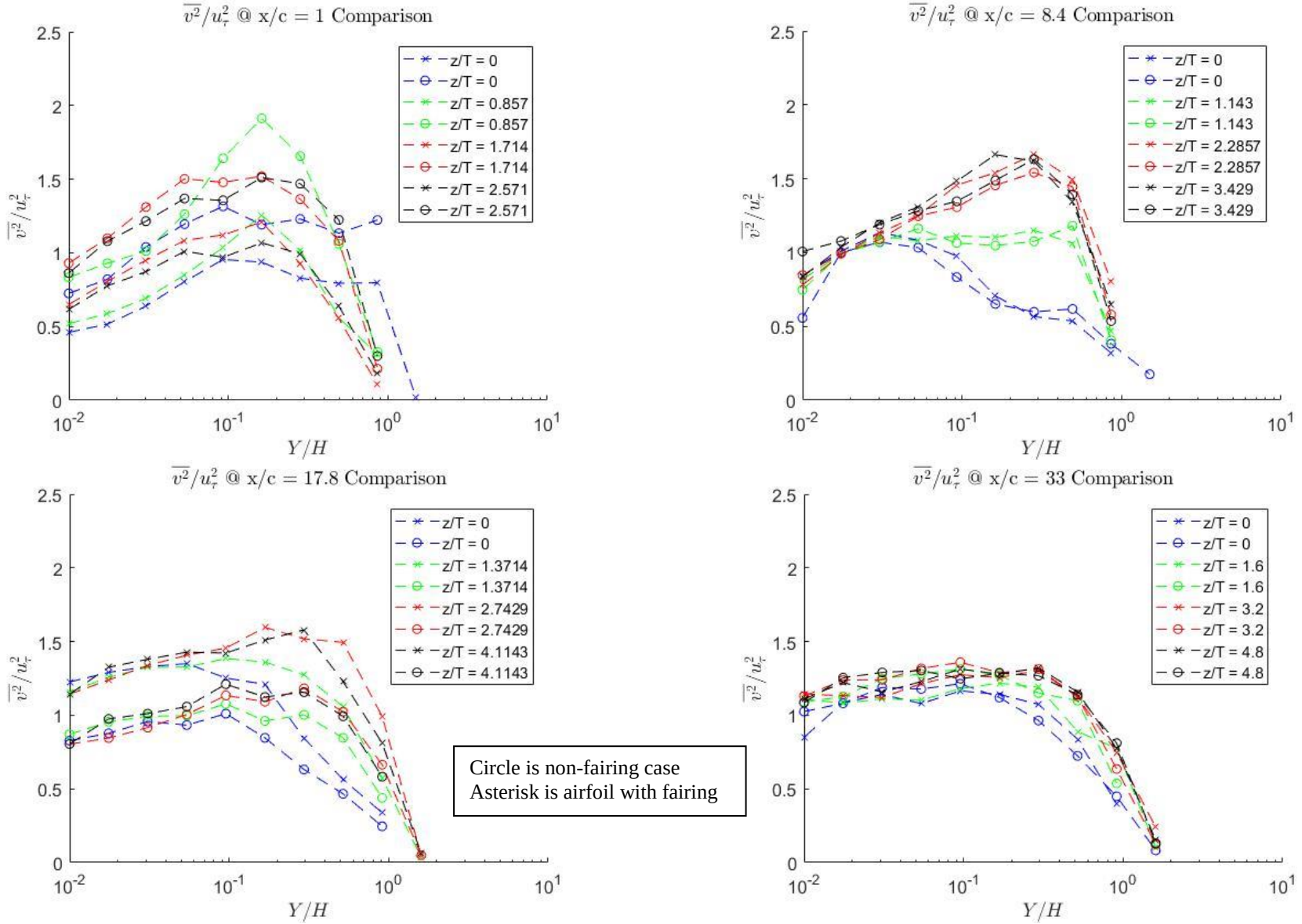

Figure 3.8.3: Fairing and non-fairing wall-normal velocity variance comparison for odd spanwise location at (a) X/C = 1 (b) X/C = 8.4 (c) X/C = 17.8 (d) X/C = 33.0

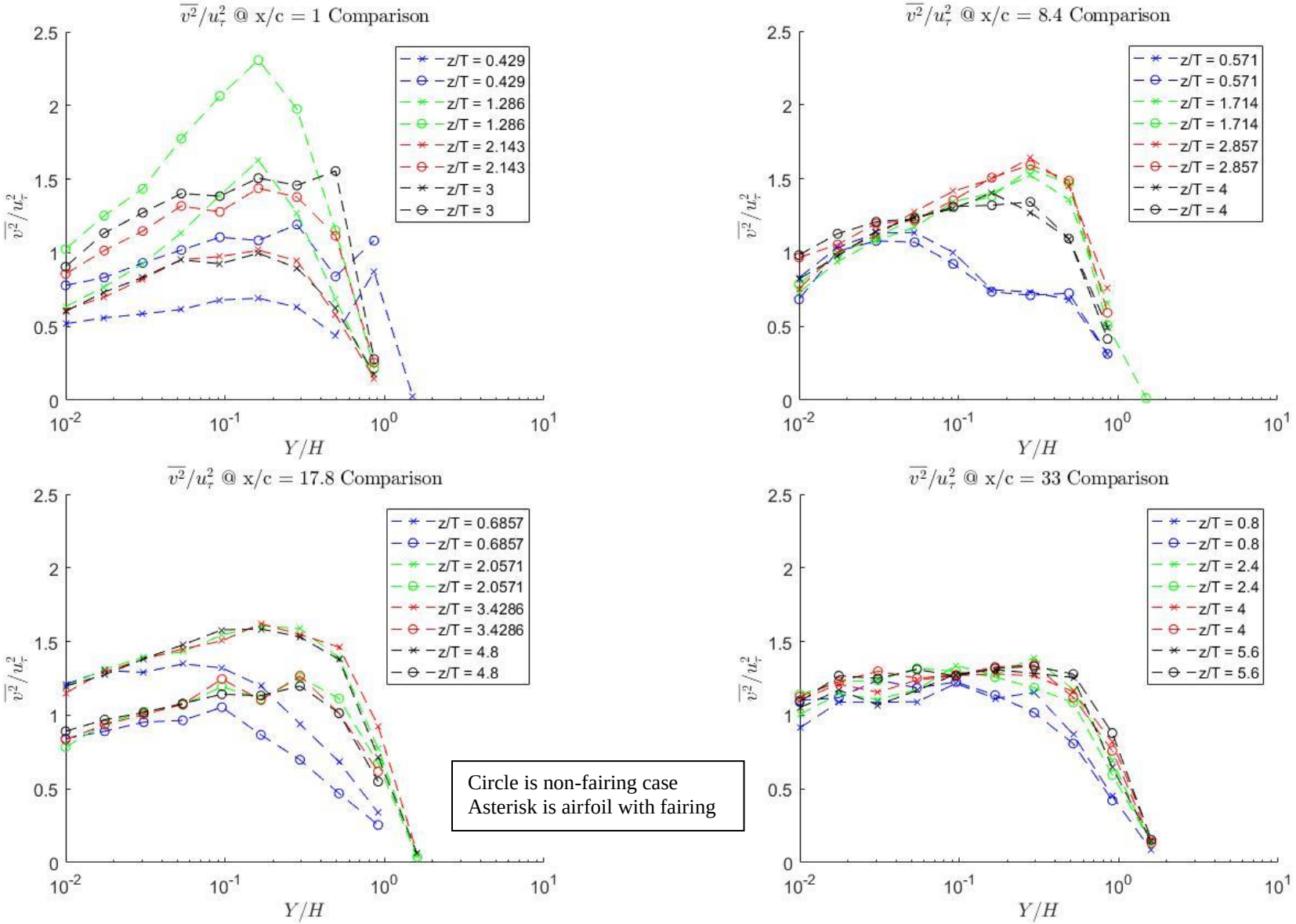

Figure 3.8.4: Fairing and non-fairing wall-normal velocity variance comparison for even spanwise location at (a) X/C = 1 (b) X/C = 8.4 (c) X/C = 17.8 (d) X/C = 33.0

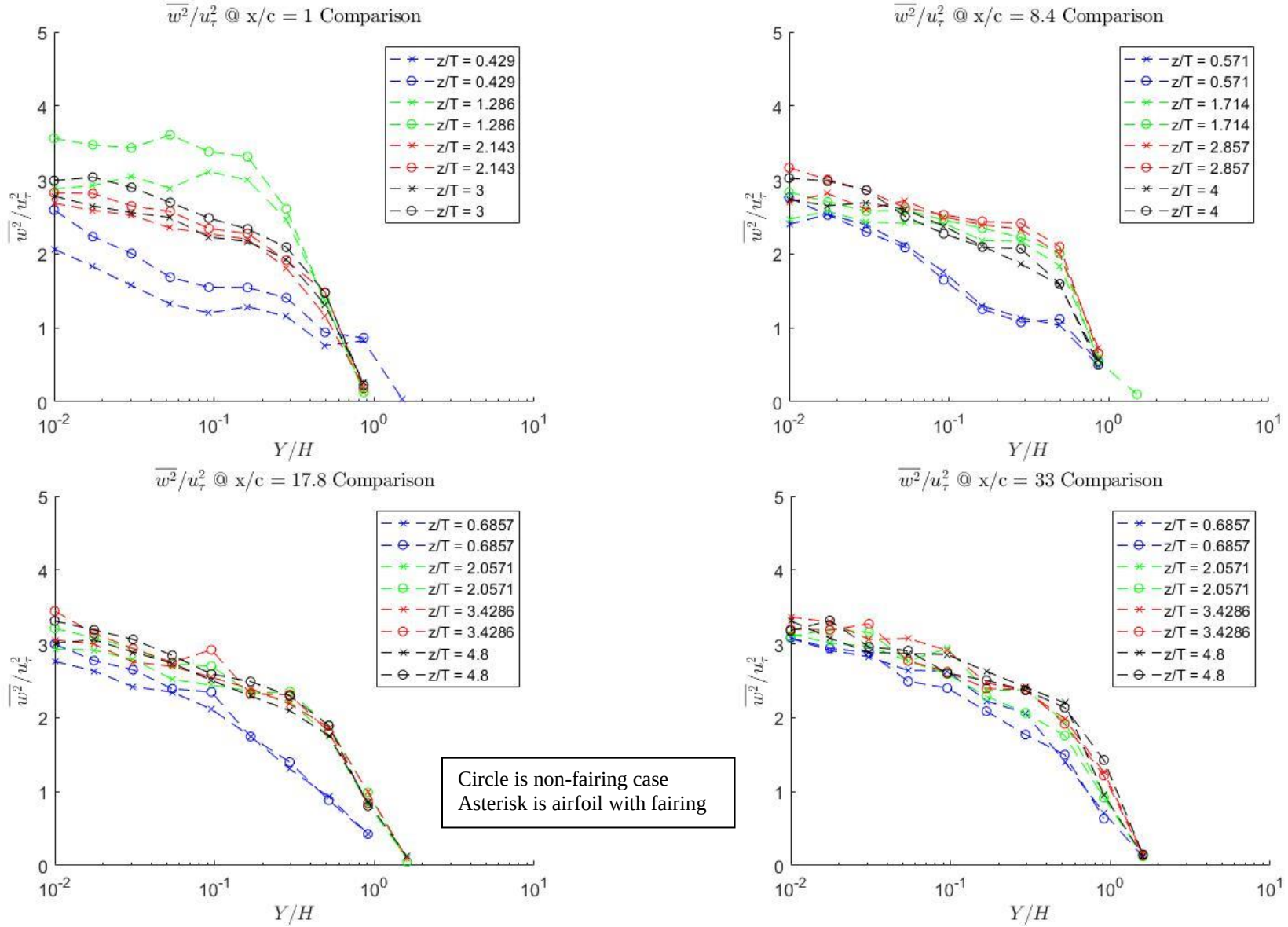

Figure 3.8.5: Fairing and non-fairing spanwise velocity variance comparison for even spanwise location at (a) X/C = 1 (b) X/C = 8.4 (c) X/C = 17.8 (d) X/C = 33.0

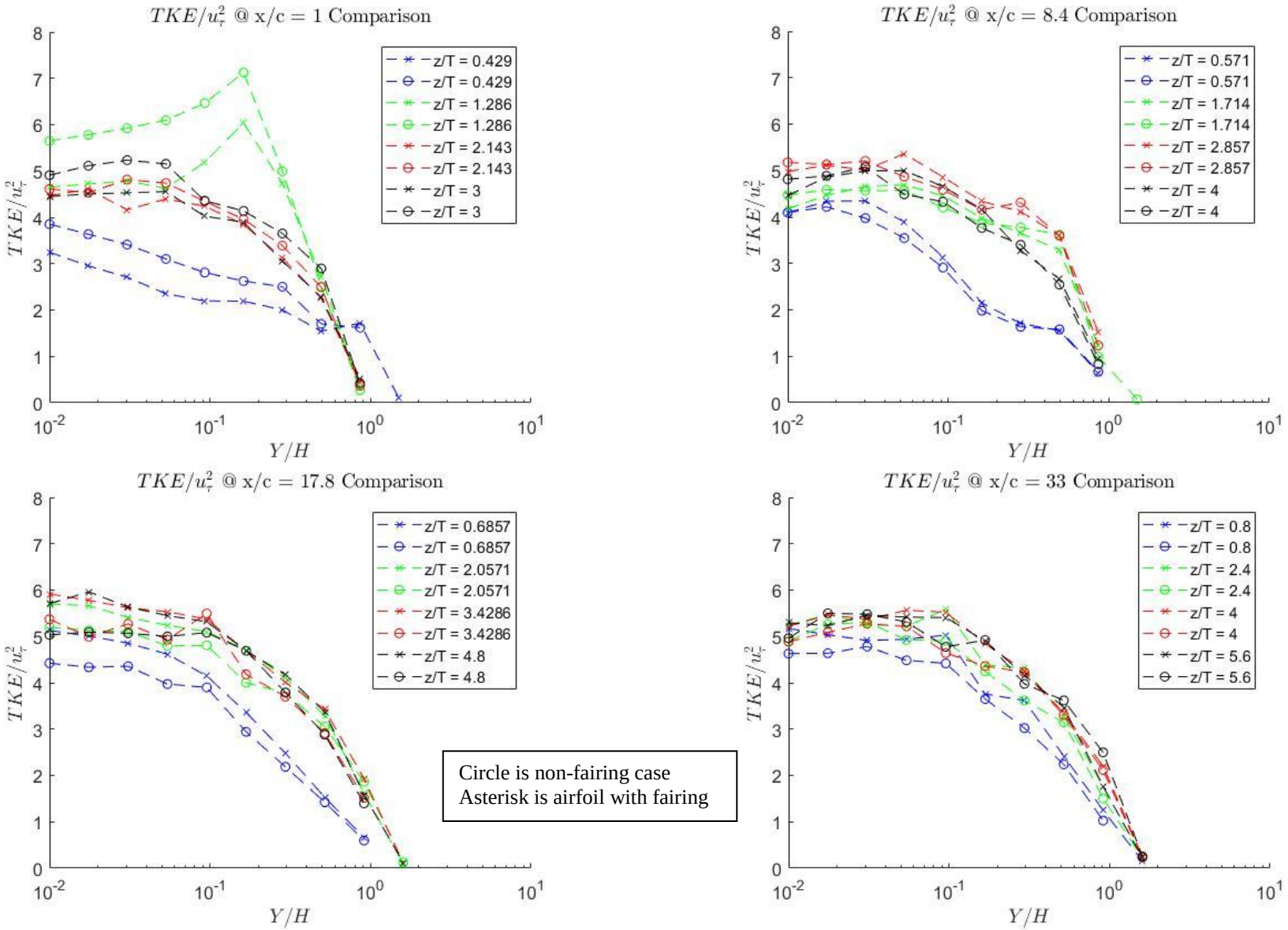

Figure 3.8.6: Fairing and non-fairing turbulent kinetic energy comparison for even spanwise location at (a) X/C = 1 (b) X/C = 8.4 (c) X/C = 17.8 (d) X/C = 33.0

CHAPTER 4: CONCLUSIONS

The present work has enhanced the understanding of the turbulent boundary layer junction flow by quantifying the downstream development of the boundary layer compared to an undisturbed boundary layer. The results at X/C = 1 show a strong influence of the junction flow on the boundary layer dynamics. Specifically, the friction velocity increase indicates a higher skin friction drag. The increase in turbulent kinetic energy and the increase in Reynolds stress indicates an increase in the turbulent transport due to the presence of the airfoil.

In a similar experiment to that performed here, Fleming et al. [7] investigated the downstream development of a junction flow. The present study is at a higher Reynolds number than Fleming and investigates the downstream development over a broader range. The mean streamwise velocity of the flow approximately recovers to the undisturbed case at 33 cord lengths downstream. The turbulent kinetic energy also appears to recover, but its individual components have not necessarily recovered specifically the wall-normal turbulence. The vorticity variance profiles provide evidence that large scale effects are primarily responsible for the non-equilibrium features of the flow. The spectra observations support this conclusion. The friction velocity also tends toward the undisturbed case at X/C = 33 but has not yet fully recovered.

The downstream development of the Reynolds stress showed a surprising result. Specifically, while the turbulent kinetic energy shows almost a complete recovery, the Reynolds

stress profiles continued to deviate from the undisturbed case. This surprising result indicates that the turbulent structure of the flow is very different from the undisturbed case despite the kinetic energy profiles being similar. The flow either needs a longer downstream development to recover, or a new state of equilibrium is being met.

In the present study, the effects of the junction flow are observed far downstream. The difference may be that in the present study the boundary layer height is on the same order as the height of the airfoil, while in previous studies the boundary layer height was only about one-half the airfoil height. Tachie et al. [14] performed a study looking at the recovery length of a forward-facing step. Their conclusions support the estimates in the literature that the recovery process will be completed in 100 length scales of the affected flow region. In their experiment, a 3mm step affected a boundary layer height of roughly 40mm for the affected flow of 0.075 leading to an estimated recovery of 7.5δ. They concluded that recovery was complete at x/h = 100 or 300mm of which 7.5δ = 300. Applying this to the current experiment where the entire boundary layer is affected, the recovered length of 100δ where δ = 0.4m would be 40m. The final measurement plane is 33 cord lengths which is roughly 35m downstream. Thus, seeing an incomplete recovery is reasonable, but the large differences in the Reynolds stress requires additional study.

To further expand on this knowledge, an airfoil with an elliptical nose and tail has been manufactured. The height of the airfoil was doubled to remove wake effects over the top as seen specifically in the vorticity variance and spectra. This will create a perturbation in which the boundary layer would be half the size of the perturbation similar to previous experiments. The wake effects are talked about in Tachie et al. [14] and could be penetrating the boundary layer and affecting how the flow is recovering. In either case, the present study shows interesting

observations to the recovery of the given turbulent boundary junction flow. Further experimentation could help to resolve the questions observed in the present study.

REFERENCES

[1] L. Prandtl, "Über flüssigkeitsbewegung bei sehr kleiner reibung," *in Verhandlungen des Dritten Internationalen Mathematiker-Kongress*, Heidelberg, 1904, A. Krazer, ed., Teubner, Leipzig, 1905;

[2] J. Klewicki, "Reynolds Number Dependence, Scaling and Dynamics of Turbulent Boundary Layers," *Journal Fluids Engineering, Transactions of the ASME,* Vol. 132, No. 9, 2010, doi: 10.1115/1.4002167

[3] Fleming, J. L., Simpson, R.L., Cowling, J.E., Devenport, W.J., "An Experimental Study of a Turbulent Wing-Body Junction and Wake Flow," *Experiments in Fluids,* Vol. 14, No. 5, 1993, pp. 366–378., doi:10.1007/bf00189496.

[4] Simpson, Roger L., "Junction Flows," *Annual Review of Fluid Mechanics,* Vol. 33, No. 1, 2001, pp. 415–443., doi:10.1146/annurev.fluid.33.1.415.

[5] Anderson, John David, "Prandtl's Classical Lifting-Line Theory*," Fundamentals of Aerodynamics,* 3rd ed., McGraw-Hill, New York, 2001, pp. 360-367

[6] Gand, F., Deck, S., Brunet, V., Sagaut, P., "Flow Dynamics Past a Simplified Wing Body Junction." *Physics of Fluids,* Vol. 22, No. 11, 2010, pp. 115111–1 - 115111–16., doi:10.1063/1.3500697.

[7] Fleming, J.L., Simpson, R.L., and Devenport, W.J., "An Experimental Study of a Turbulent Wing-Body Junction and Wake Flow," Virginia Polytechnic and State University, Aerospace and Ocean Engineering Department, Report No. VPI-AOE-179 Blacksburg, VA.. Sept 1991.

[8] Ryu, S., Emory, M., Iaccarino, G., Campos, A., "Large-Eddy Simulation of a Wing Body Junction Flow." *AIAA Journal,* Vol. 54, No. 3, 2016, pp. 793–804., doi:10.2514/1.J054212.

[9] Simpson, Roger L., "Some Observations on the Structure and Modeling of 3-D Turbulent Boundary Layers and Separated Flow." *Proceedings of the 4th International Symposium on Turbulence and Shear Flow Phenomena* (TSFP-4), Williamsburg, VA, Vol. 1, 2005, pp. 1 -10

[10] Devenport, W. J., Agarwal, N.K., Dewitz, M.B., Simpson, R.L., Poddar, K., "Effects of a Fillet on the Flow Past a Wing-Body Junction." *AIAA Journal*, Vol. 28, No. 12, 1990, pp. 2017–2024., doi:10.2514/3.10517.

[11] Vincenti P., Klewicki J., Morrill-Winter C., White C. M., Wosnik M., "Streamwise Velocity Statistics in Turbulent Boundary Layers that Spatially Develop to High Reynolds Number" *Experiments in Fluids*, Vol. 54, No. 1629, 2013, pp. 1629–1641., doi:10.1007/s00348-013-1629-9

[12] Zimmerman, S., Morril-Winter, C., Klewicki, J., "Design and Implementation of a Hot Wire Probe for Simultaneous Velocity and Vorticity Vector Measurements on Boundary Layers" (not yet published)

[13] Patel, V. C., "Calibration of the Preston Tube and Limitations on Its Use in Pressure Gradients," *Journal of Fluid Mechanics*, Vol. 23, No. 1, 1965, pp. 185-208. doi:10.1017/S0022112065001301

[14] Tachie, M. F., Balachandar, R., Bergstrom, D. J., "Open Channel Boundary Layer Relaxation Behind a Forward Facing Step at Low Reynolds Numbers," *Journal Fluids Engineering, Transactions of the ASME*, Vol. 123, No. 3, 2001, doi:10.1115/1.1383971

APPENDIX

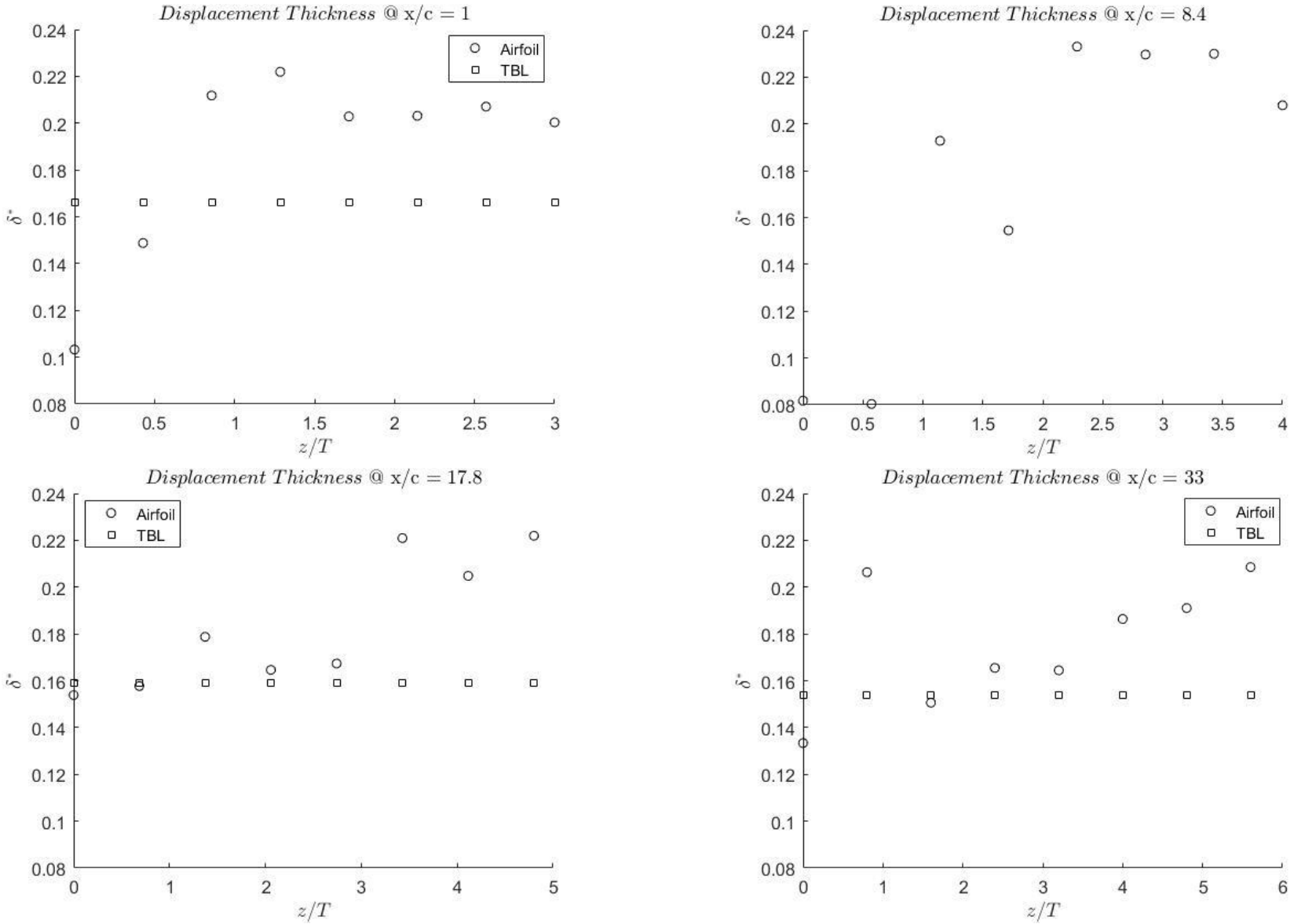

Figure A.A.1: Displacement thickness at (a) X/C = 1 (b) X/C = 8.4 (c) X/C = 17.8 (d) X/C = 33.0 at spanwise locations z/T and undisturbed turbulent boundary layer (TBL)

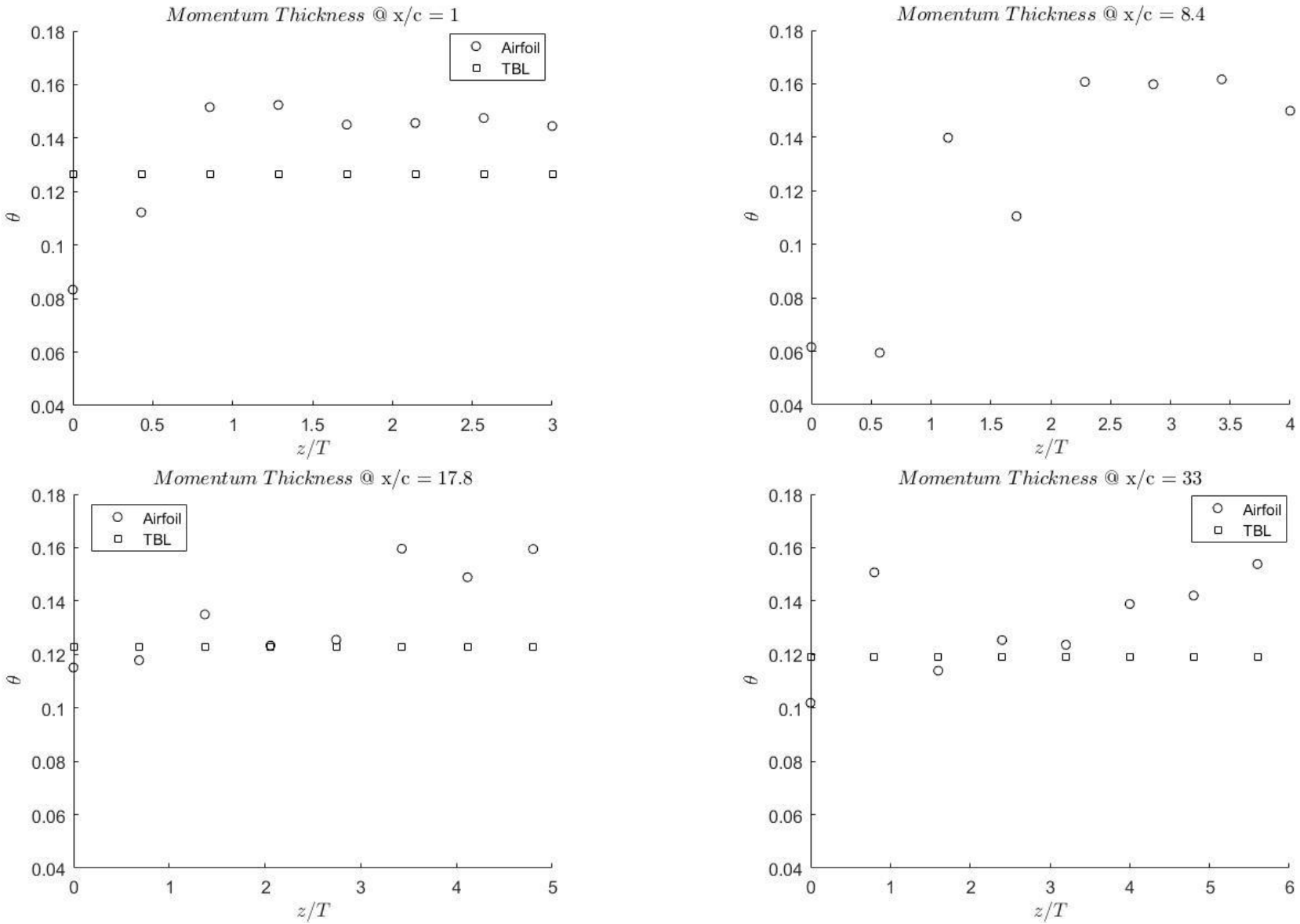

Figure A.A.2: Momentum thickness at (a) X/C = 1 (b) X/C = 8.4 (c) X/C = 17.8 (d) X/C = 33.0 at spanwise locations z/T and undisturbed turbulent boundary layer (TBL)

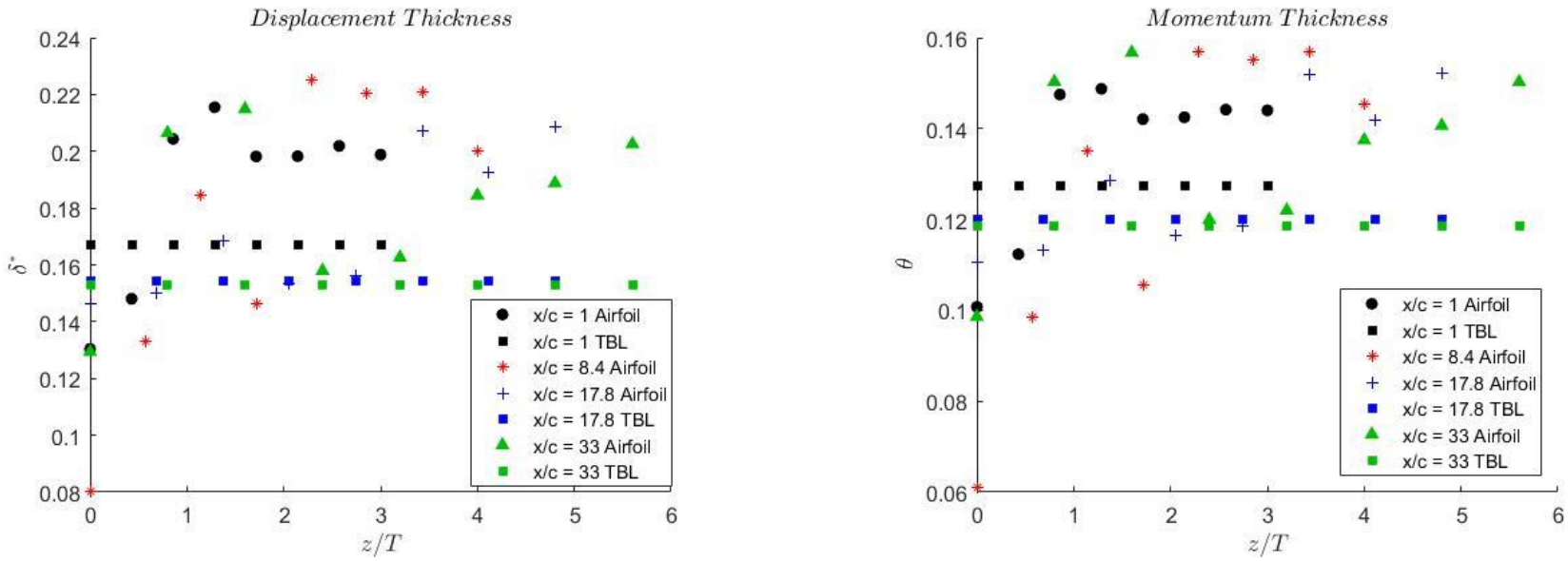

Figure A.A.3: Displacement and momentum thickness at all locations at spanwise locations z/T and undisturbed turbulent boundary layer (TBL)

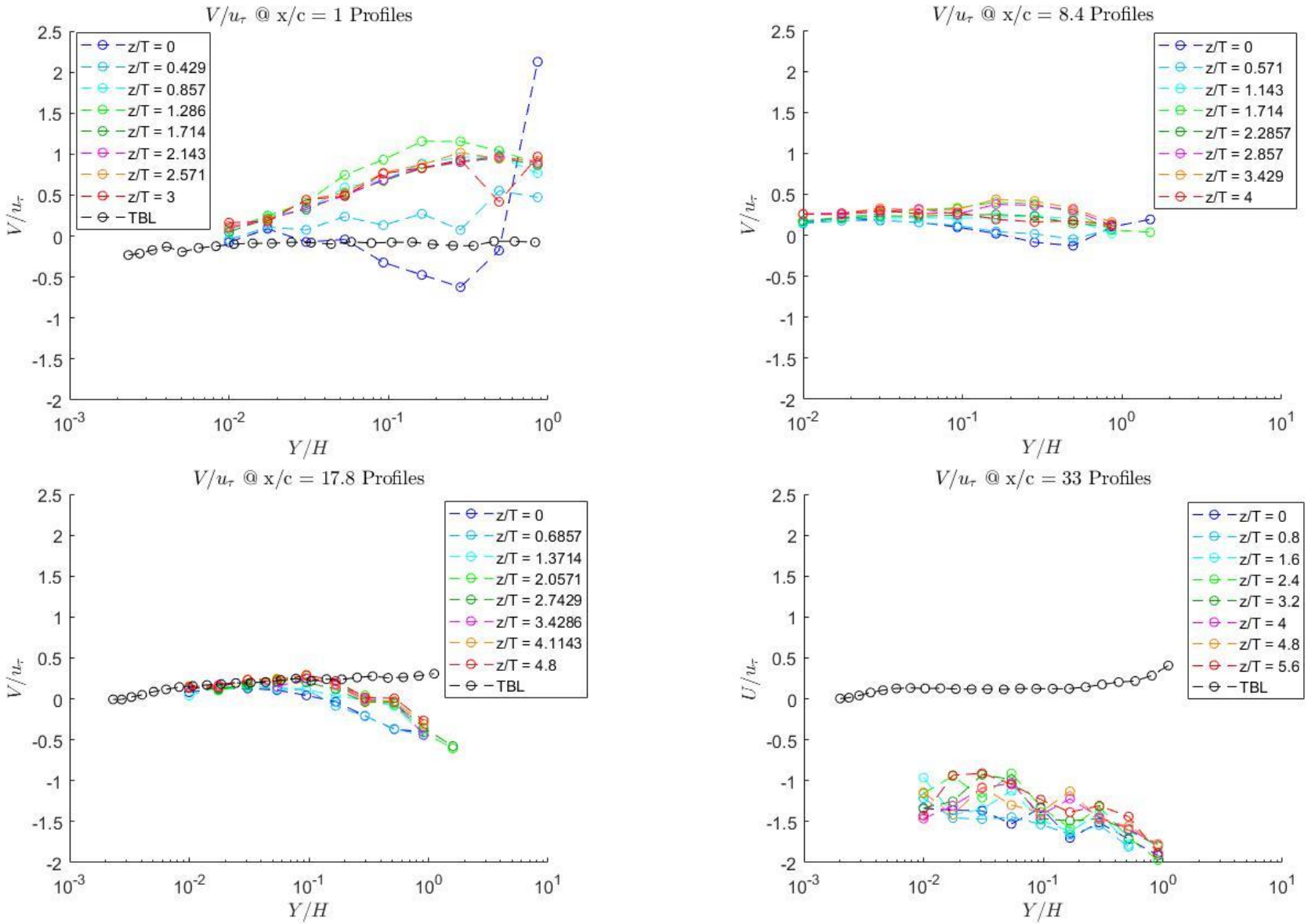

Figure A.A.4: Wall-normal mean velocity profiles normalized by u_τ at (a) X/C = 1 (b) X/C = 8.4 (c) X/C = 17.8 (d) X/C = 33.0 at spanwise locations z/T and undisturbed turbulent boundary layer (TBL)

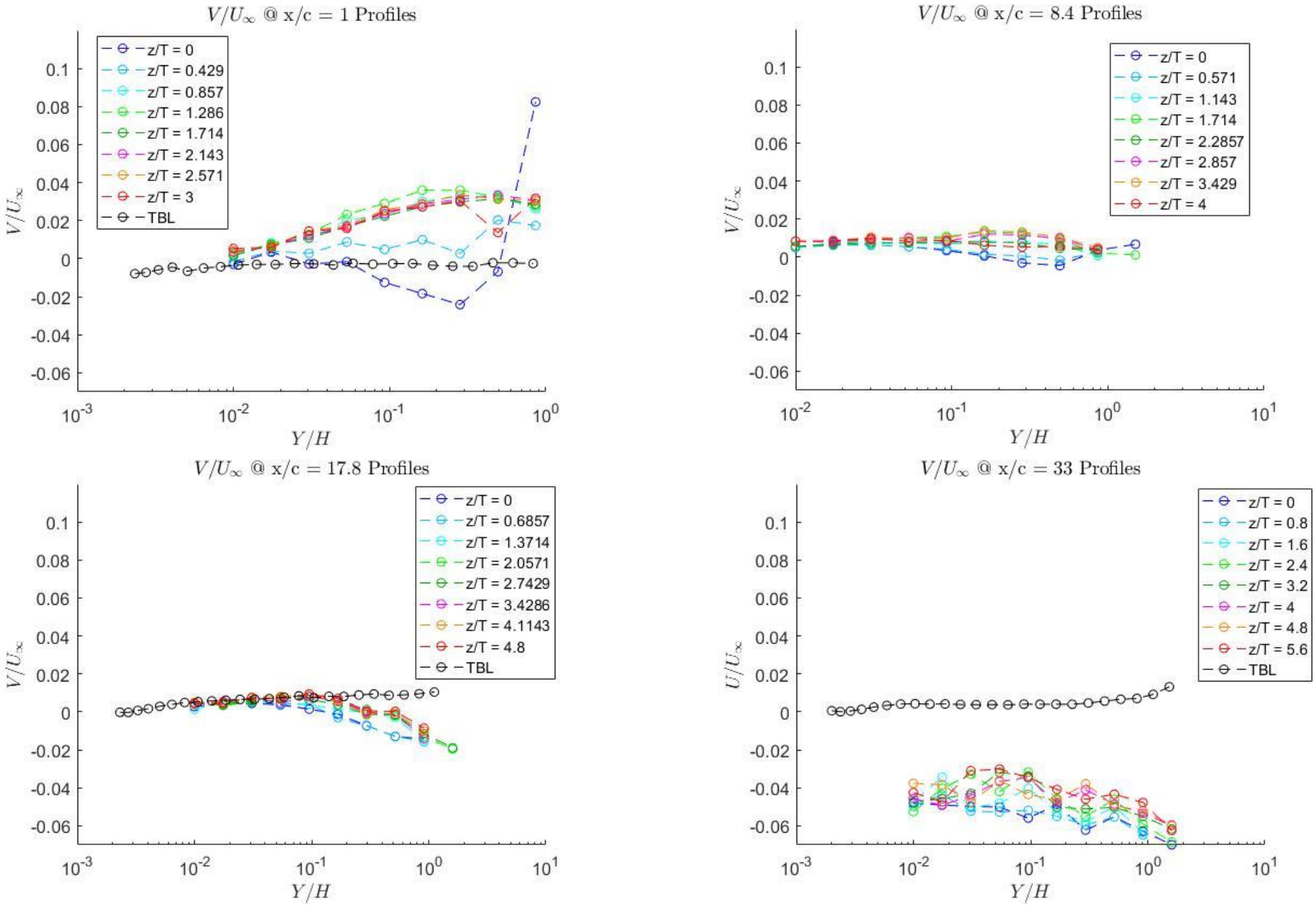

Figure A.A.5: Wall-normal mean velocity profiles normalized by U_∞ at (a) X/C = 1 (b) X/C = 8.4 (c) X/C = 17.8 (d) X/C = 33.0 at spanwise locations z/T and undisturbed turbulent boundary layer (TBL)

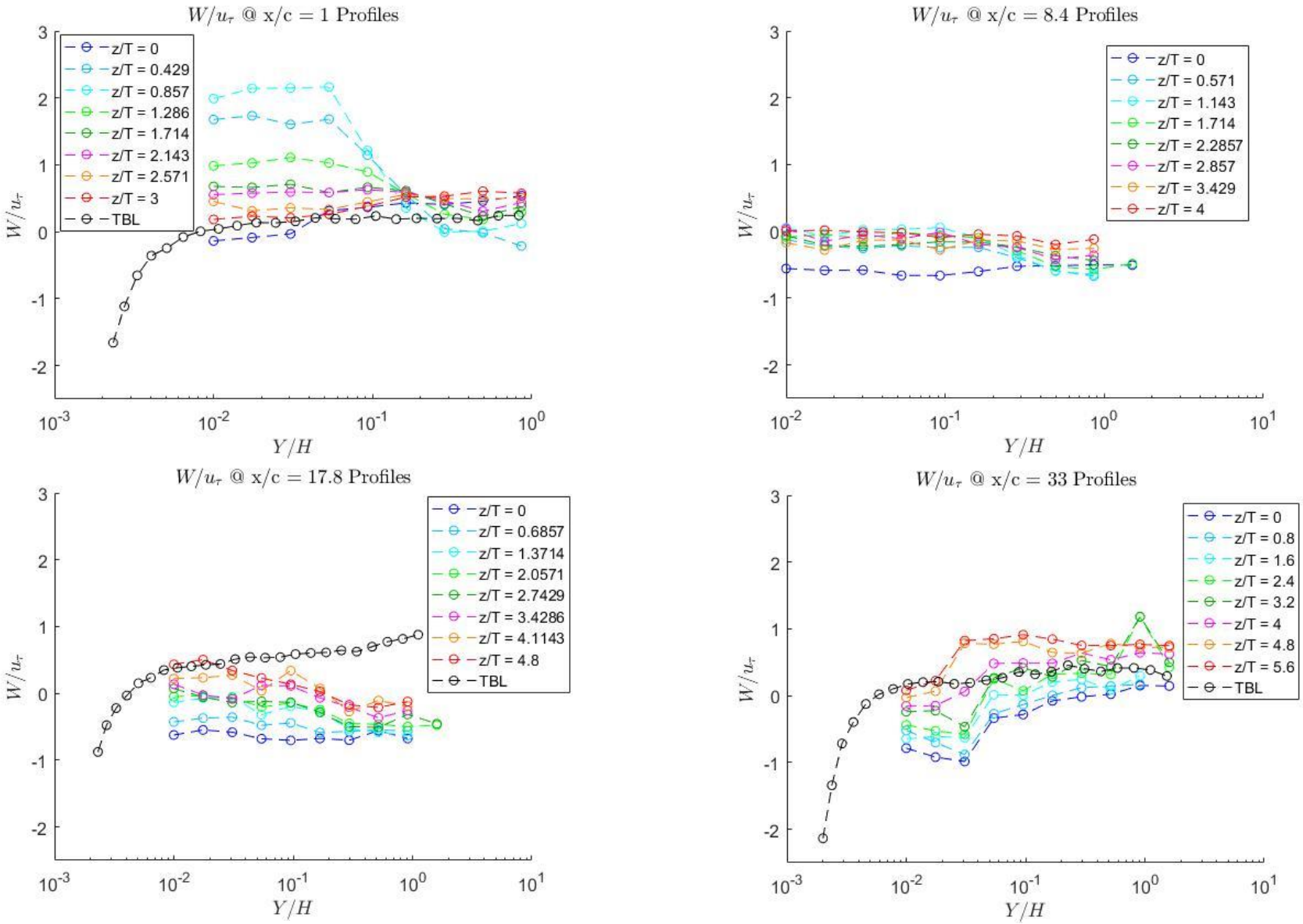

Figure A.A.6: Spanwise mean velocity profiles normalized by u_τ at (a) X/C = 1 (b) X/C = 8.4 (c) X/C = 17.8 (d) X/C = 33.0 at spanwise locations z/T and undisturbed turbulent boundary layer (TBL)

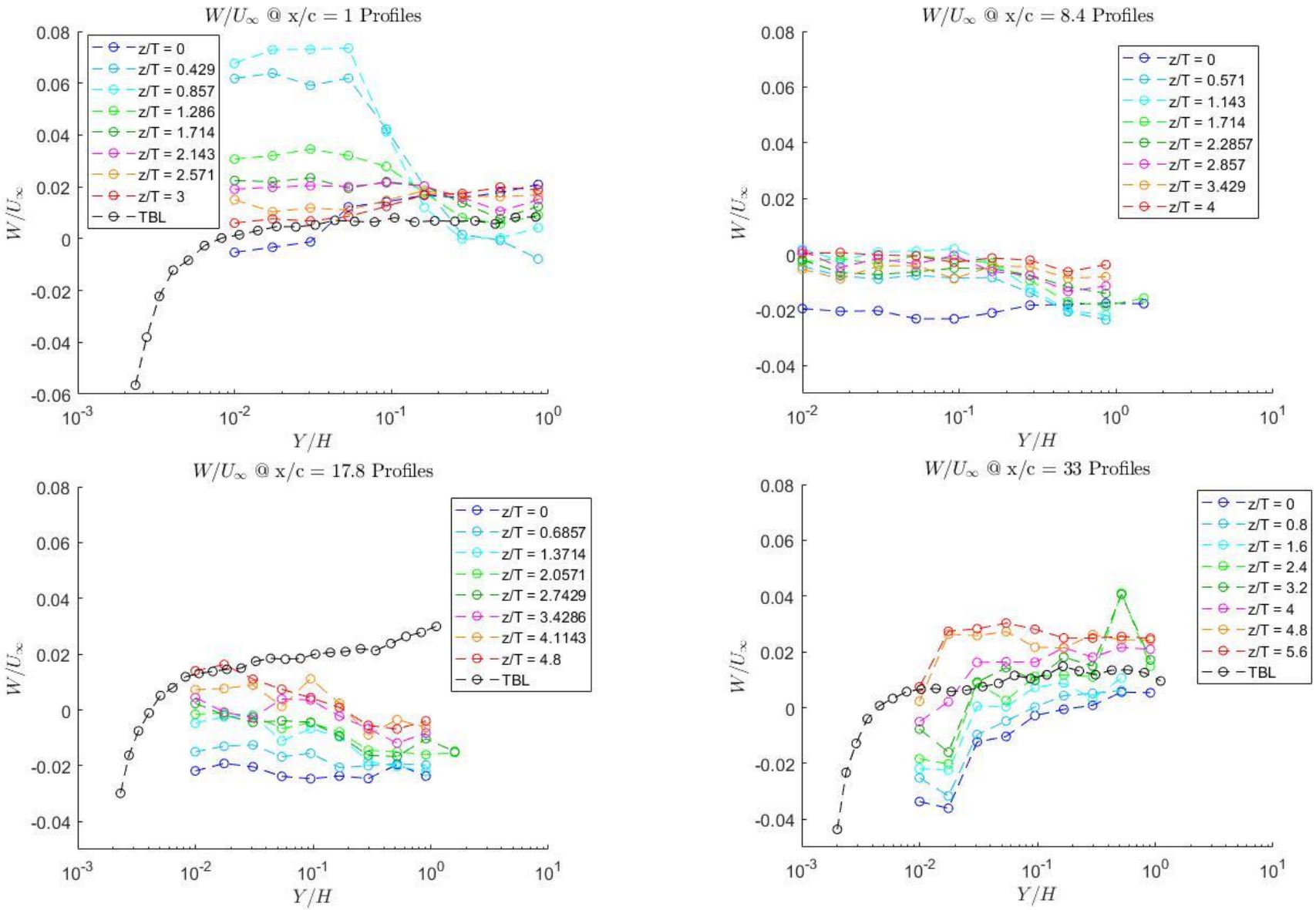

Figure A.A.7: Spanwise velocity profiles normalized by U_∞ at (a) X/C = 1 (b) X/C = 8.4 (c) X/C = 17.8 (d) X/C = 33.0 at spanwise locations z/T and undisturbed turbulent boundary layer (TBL)

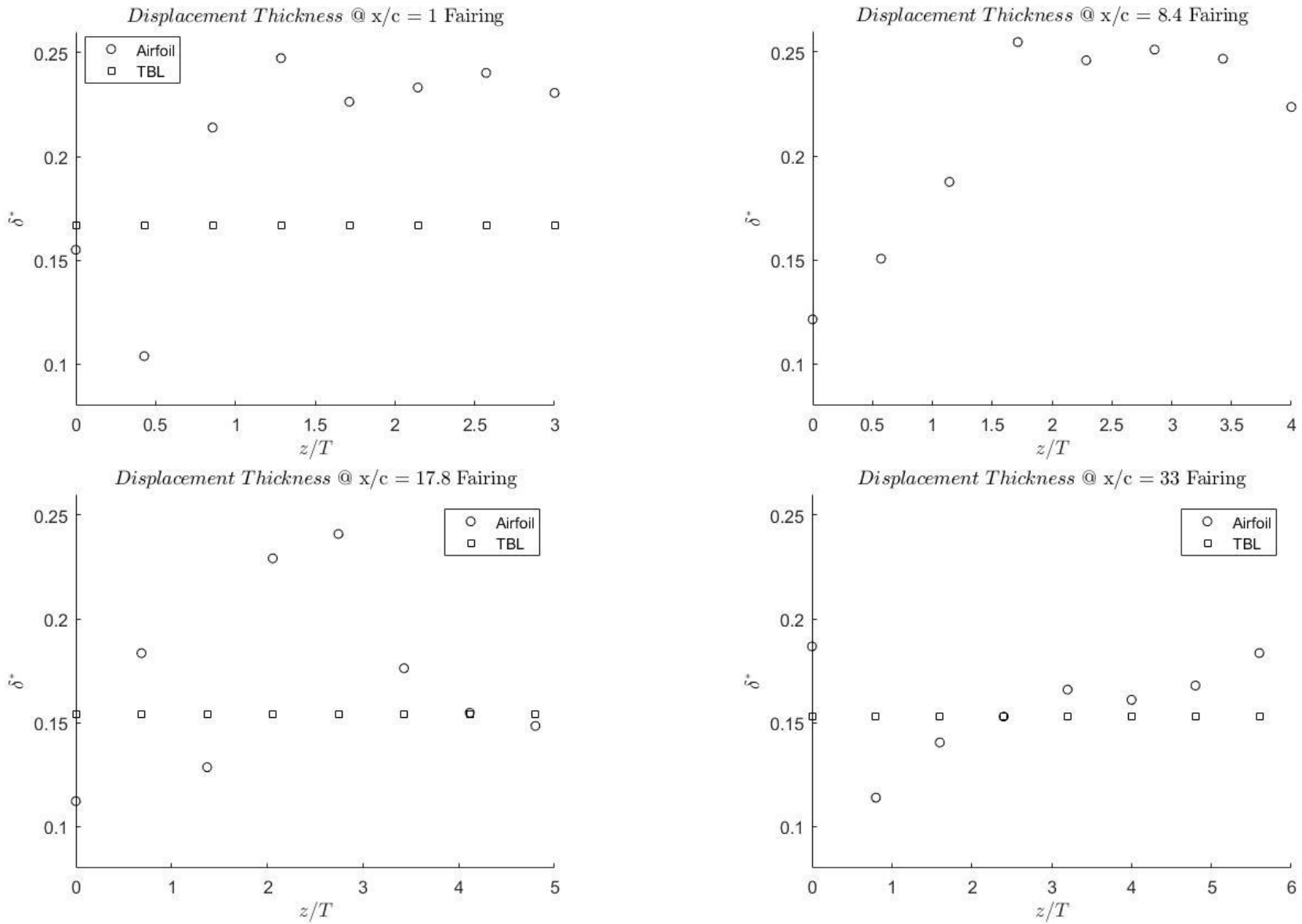

Figure A.F.1: Displacement thickness for airfoil with fairing at (a) X/C = 1 (b) X/C = 8.4 (c) X/C = 17.8 (d) X/C = 33.0 at spanwise locations z/T and undisturbed turbulent boundary layer (TBL)

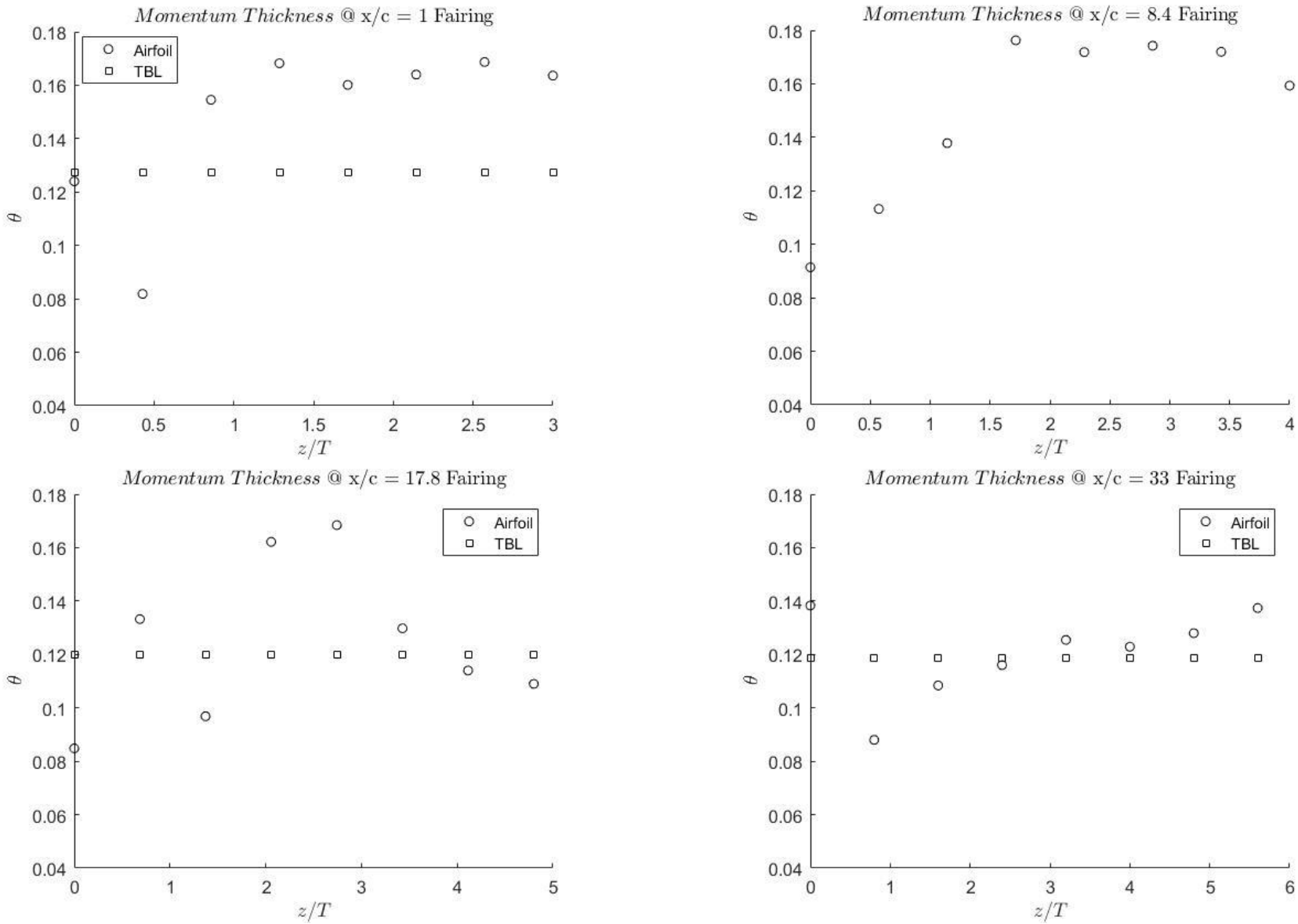

Figure A.F.2: Momentum thickness for Airfoil with fairing at (a) X/C = 1 (b) X/C = 8.4 (c) X/C = 17.8 (d) X/C = 33.0 at spanwise locations z/T and undisturbed turbulent boundary layer (TBL)

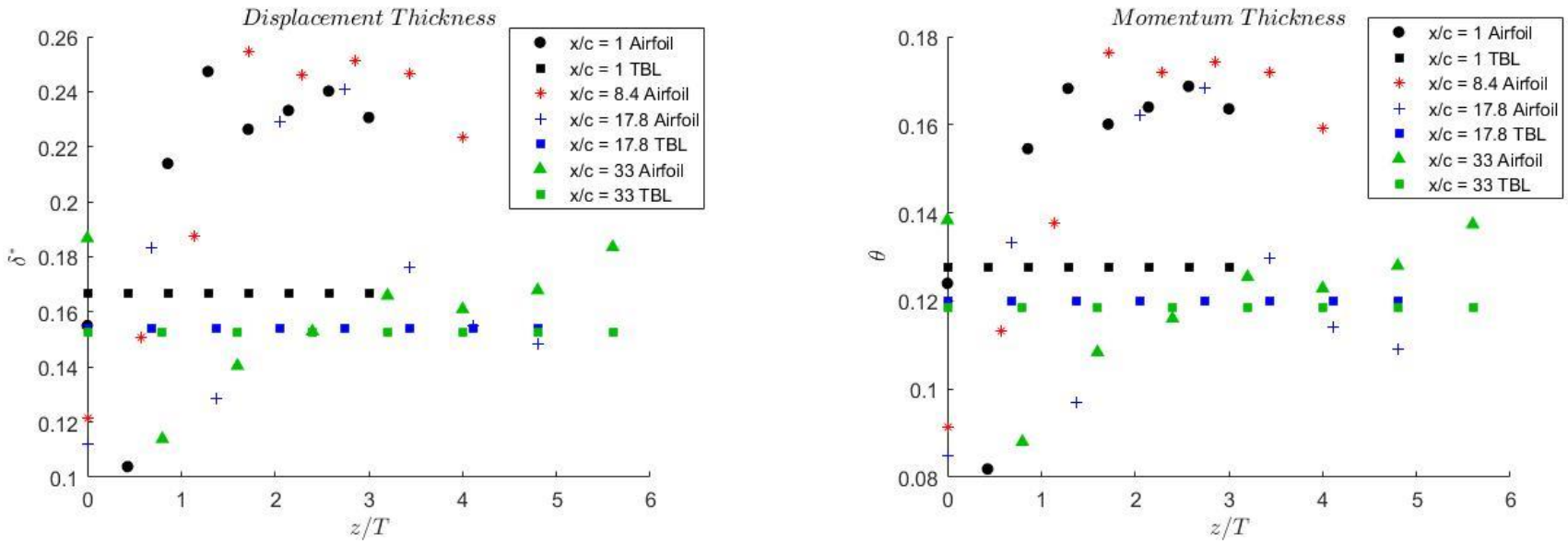

Figure A.F.3: Displacement and momentum thickness at all locations for airfoil with fairing at spanwise locations z/T and undisturbed turbulent boundary layer (TBL)

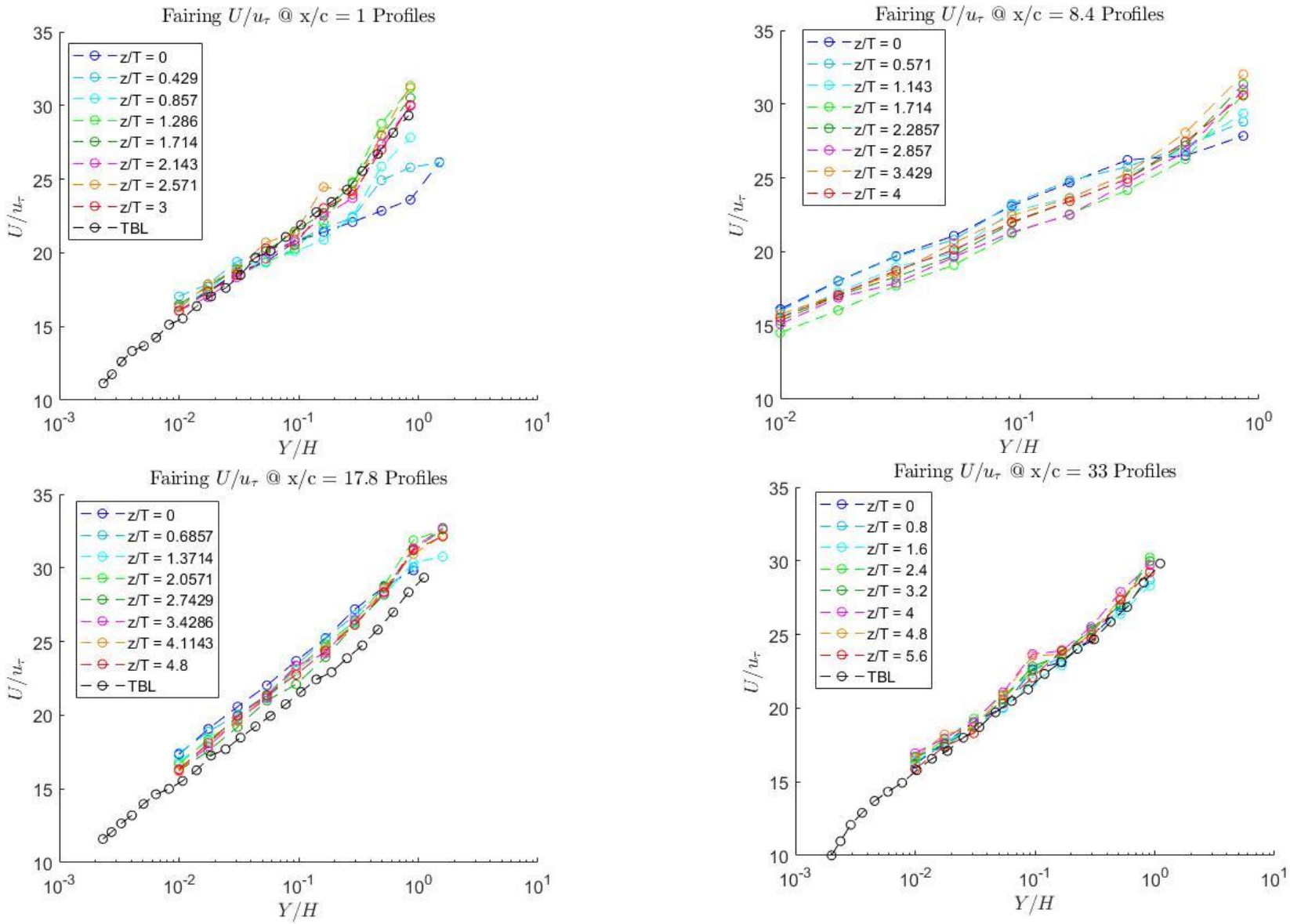

Figure A.F.4: Fairing streamwise mean velocity profiles normalized by u_τ at (a) X/C = 1 (b) X/C = 8.4 (c) X/C = 17.8 (d) X/C = 33.0 at spanwise locations z/T and undisturbed turbulent boundary layer (TBL)

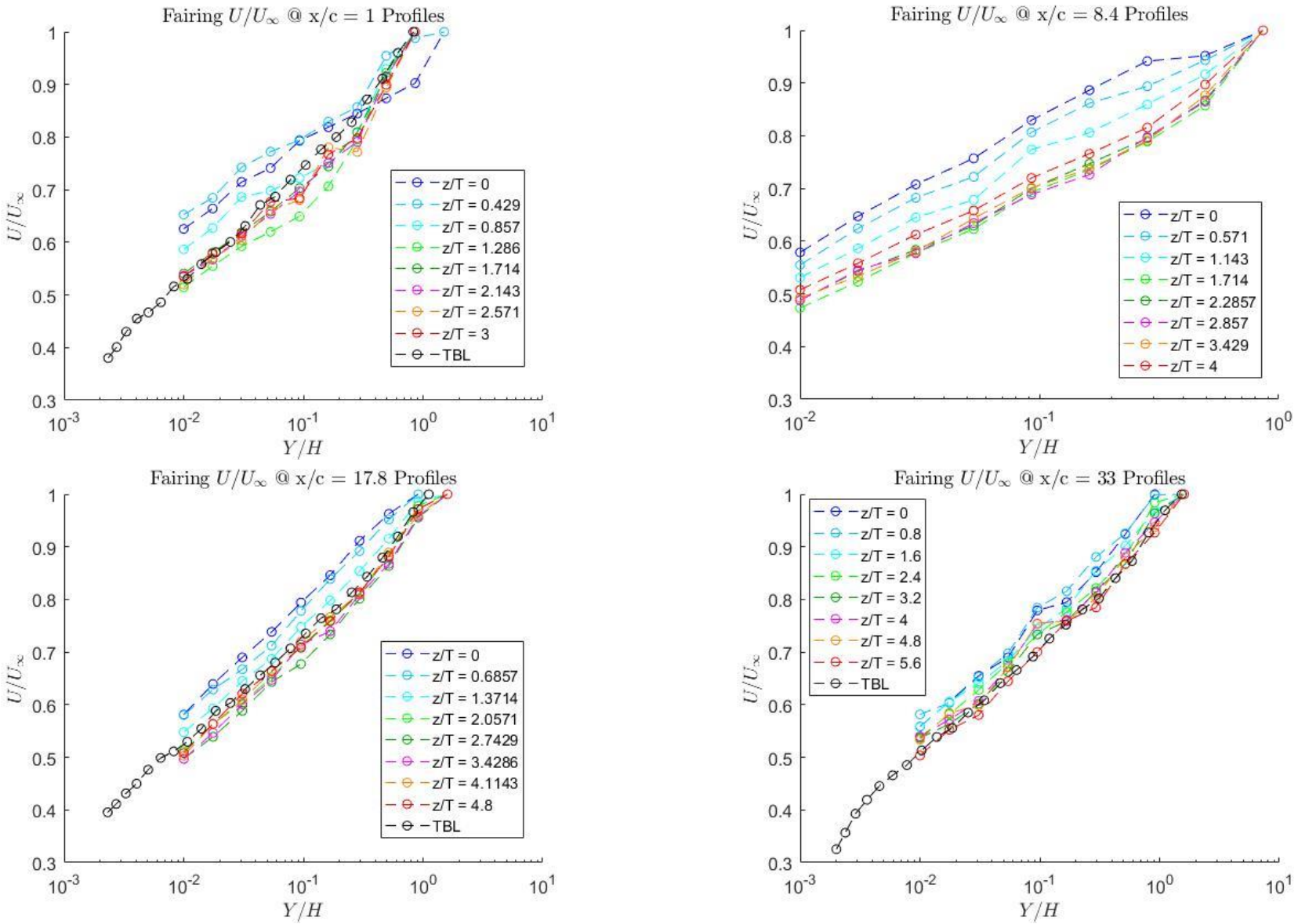

Figure A.F.5: Fairing streamwise mean velocity profiles normalized by U_∞ at (a) X/C = 1 (b) X/C = 8.4 (c) X/C = 17.8 (d) X/C = 33.0 at spanwise locations z/T and undisturbed turbulent boundary layer (TBL)

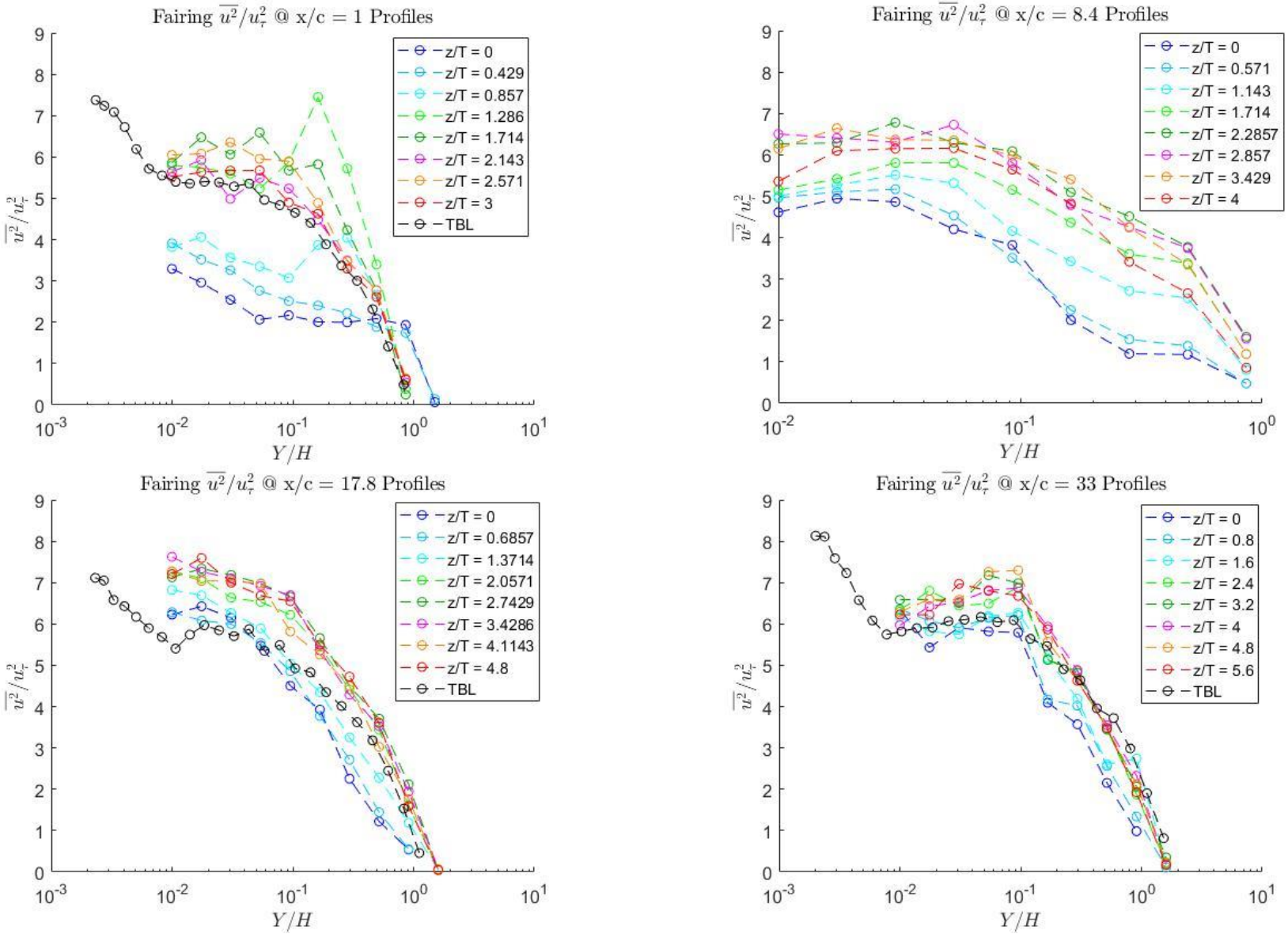

Figure A.F.6: Fairing streamwise velocity variance normalized by u_τ at (a) X/C = 1 (b) X/C = 8.4 (c) X/C = 17.8 (d) X/C = 33.0 at spanwise locations z/T and undisturbed turbulent boundary layer (TBL)

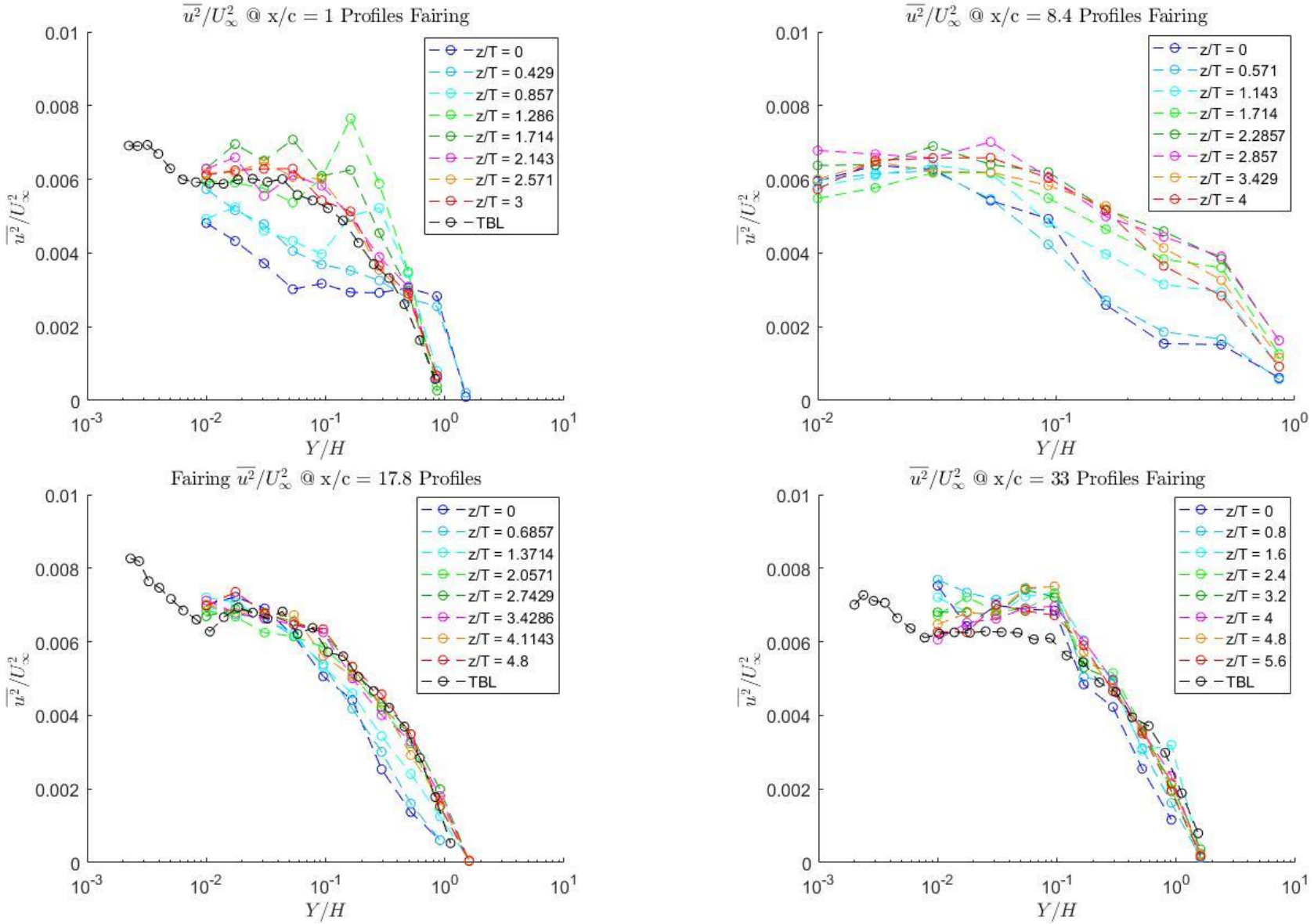

Figure A.F.7: Fairing streamwise velocity variance normalized by U_∞ at (a) X/C = 1 (b) X/C = 8.4 (c) X/C = 17.8 (d) X/C = 33.0 at spanwise locations z/T and undisturbed turbulent boundary layer (TBL)

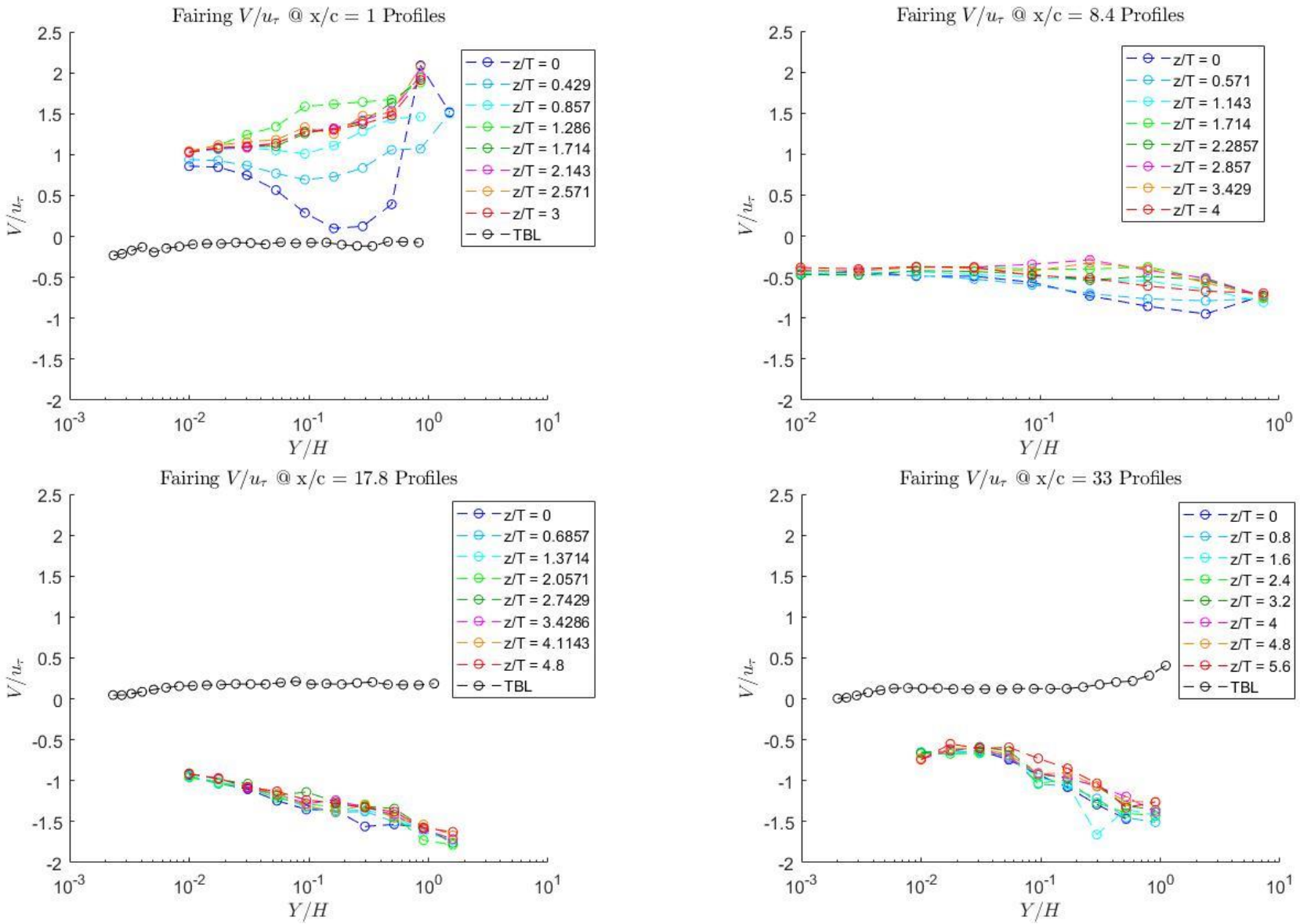

Figure A.F.8: Fairing wall-normal mean velocity profiles normalized by u_τ at (a) X/C = 1 (b) X/C = 8.4 (c) X/C = 17.8 (d) X/C = 33.0 at spanwise locations z/T and undisturbed turbulent boundary layer (TBL)

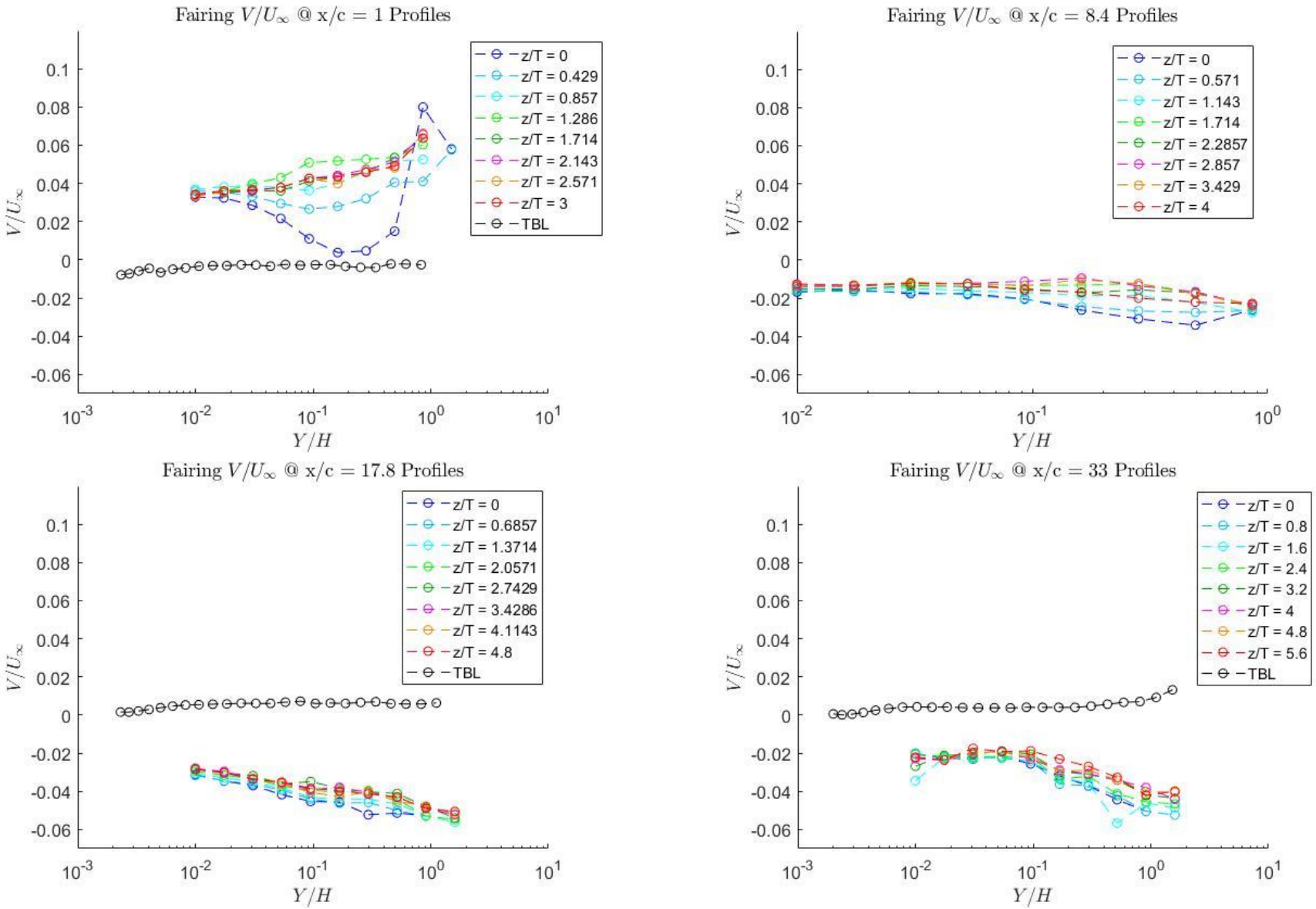

Figure A.F.9: Fairing wall-normal mean velocity profiles normalized by U_∞ at (a) X/C = 1 (b) X/C = 8.4 (c) X/C = 17.8 (d) X/C = 33.0 at spanwise locations z/T and undisturbed turbulent boundary layer (TBL)

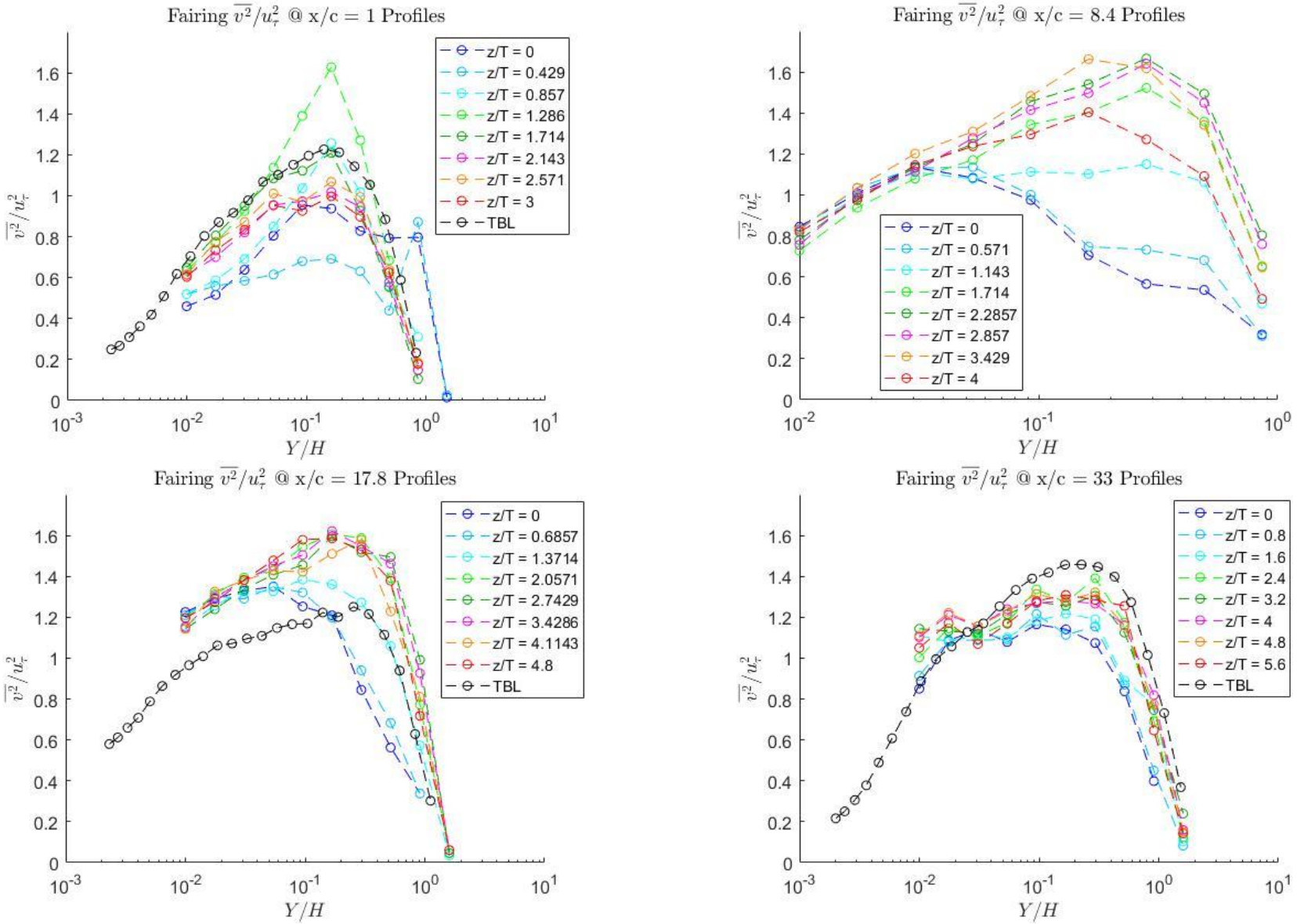

Figure A.F.10: Fairing wall-normal velocity variance normalized by u_τ at (a) X/C = 1 (b) X/C = 8.4 (c) X/C = 17.8 (d) X/C = 33.0 at spanwise locations z/T and undisturbed turbulent boundary layer (TBL)

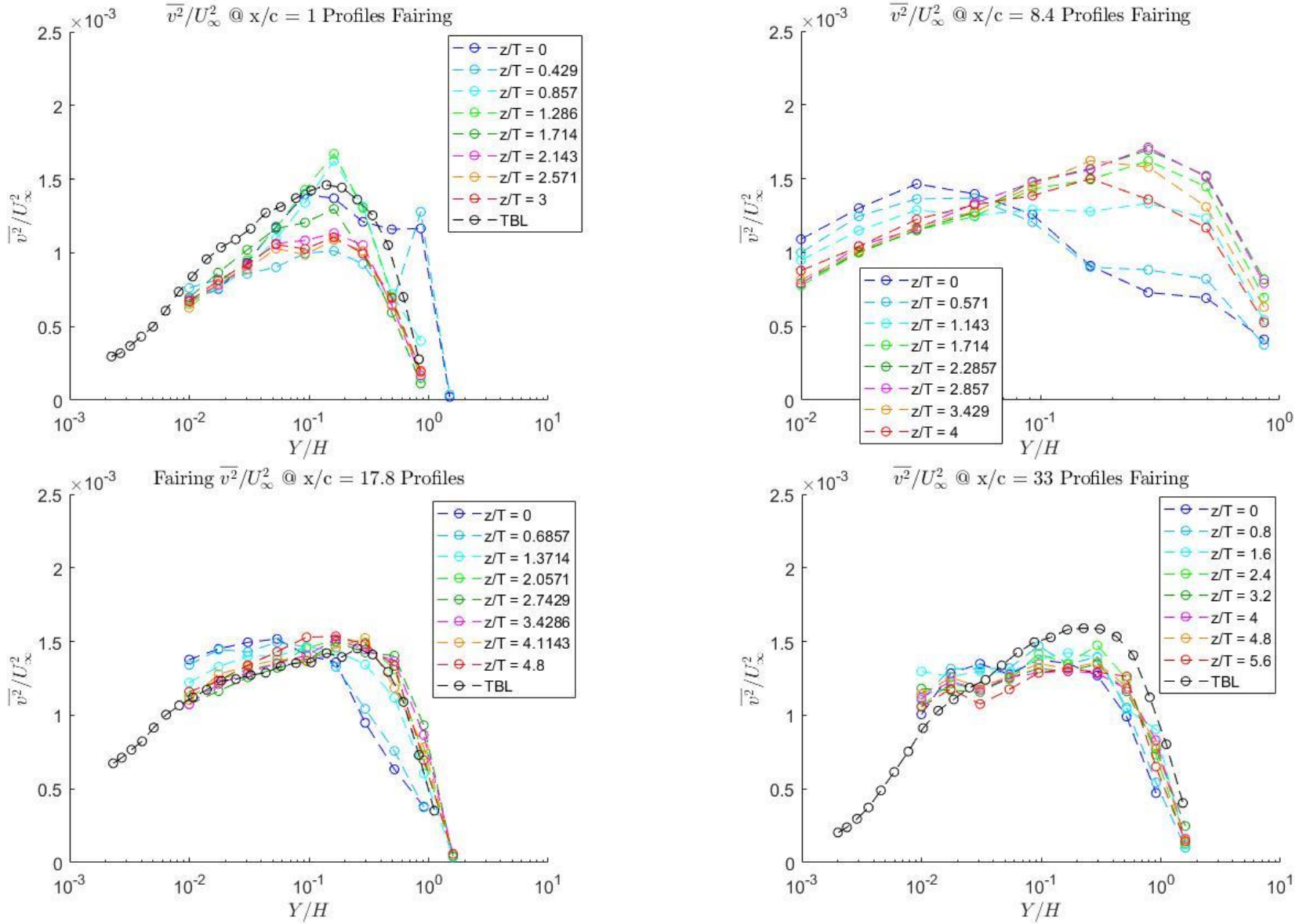

Figure A.F.11: Fairing wall-normal velocity variance normalized by U_∞ at (a) X/C = 1 (b) X/C = 8.4 (c) X/C = 17.8 (d) X/C = 33.0 at spanwise locations z/T and undisturbed turbulent boundary layer (TBL)

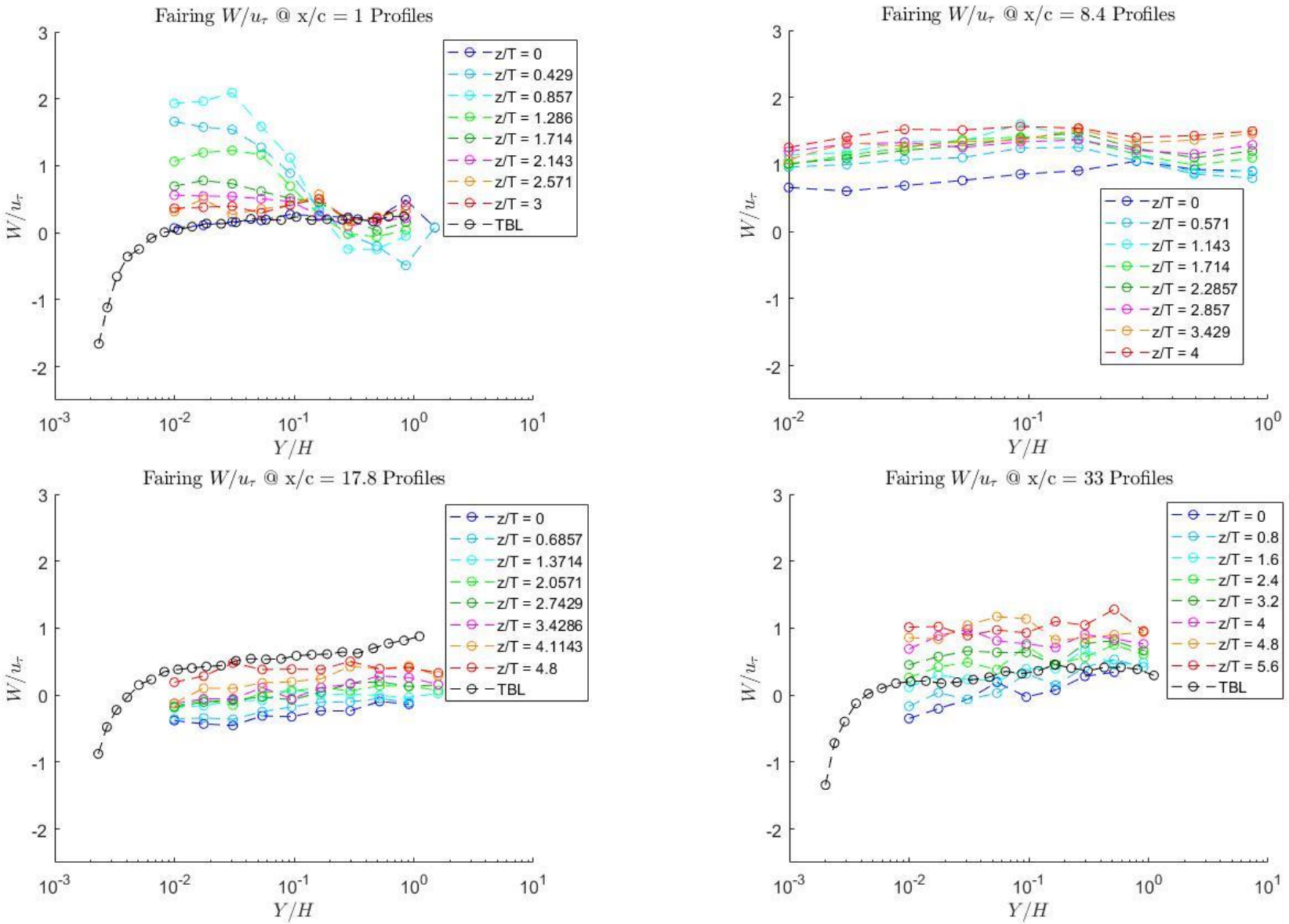

Figure A.F.12: Fairing spanwise mean velocity profiles normalized by u_τ at (a) X/C = 1 (b) X/C = 8.4 (c) X/C = 17.8 (d) X/C = 33.0 at spanwise locations z/T and undisturbed turbulent boundary layer (TBL)

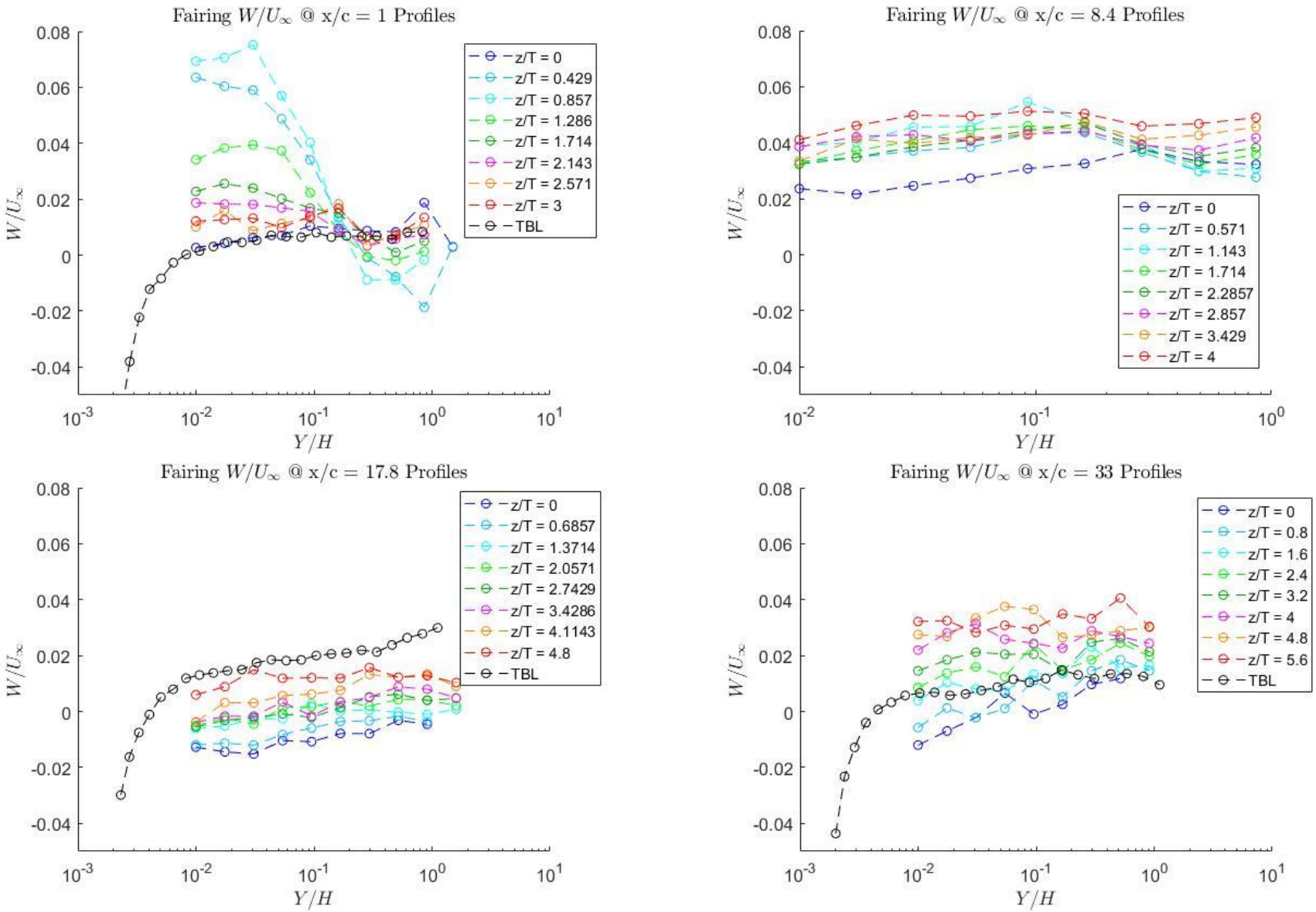

Figure A.F.13: Fairing spanwise mean velocity profiles normalized by U_∞ at (a) X/C = 1 (b) X/C = 8.4 (c) X/C = 17.8 (d) X/C = 33.0 at spanwise locations z/T and undisturbed turbulent boundary layer (TBL)

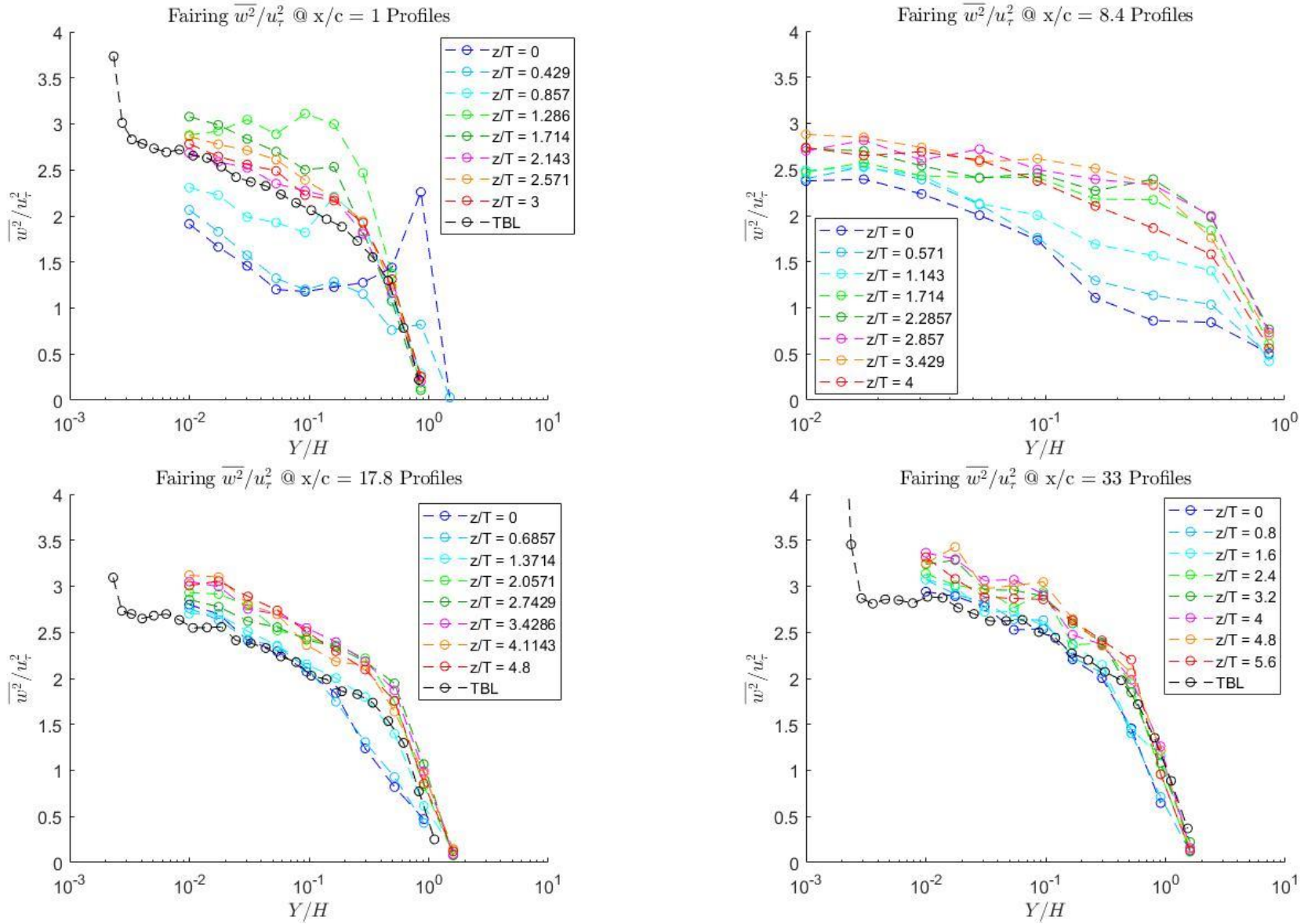

Figure A.F.14: Fairing spanwise velocity variance normalized by u_τ at (a) X/C = 1 (b) X/C = 8.4 (c) X/C = 17.8 (d) X/C = 33.0 at spanwise locations z/T and undisturbed turbulent boundary layer (TBL)

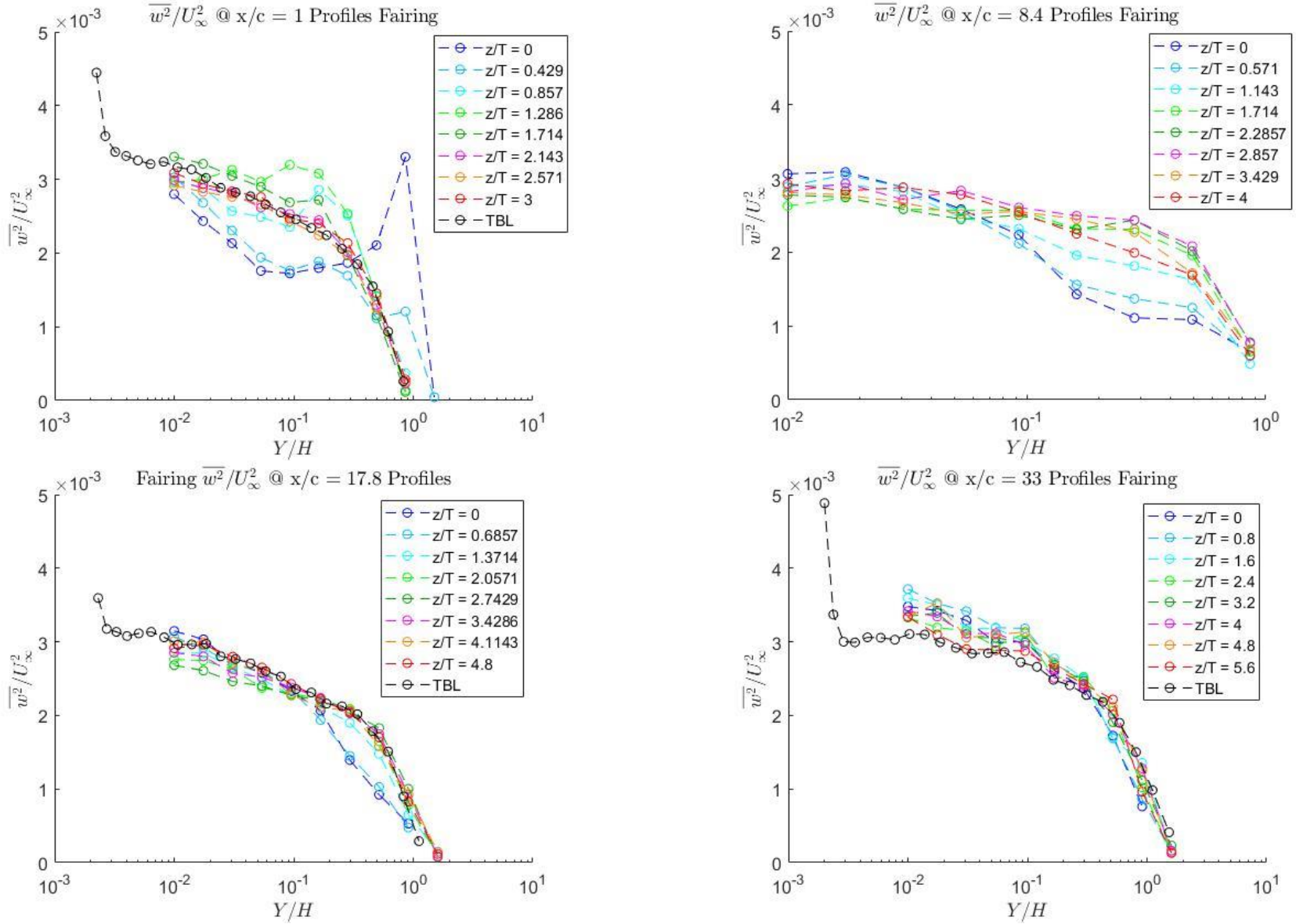

Figure A.F.15: Fairing spanwise velocity variance normalized by U_∞ at (a) X/C = 1 (b) X/C = 8.4 (c) X/C = 17.8 (d) X/C = 33.0 at spanwise locations z/T and undisturbed turbulent boundary layer (TBL)

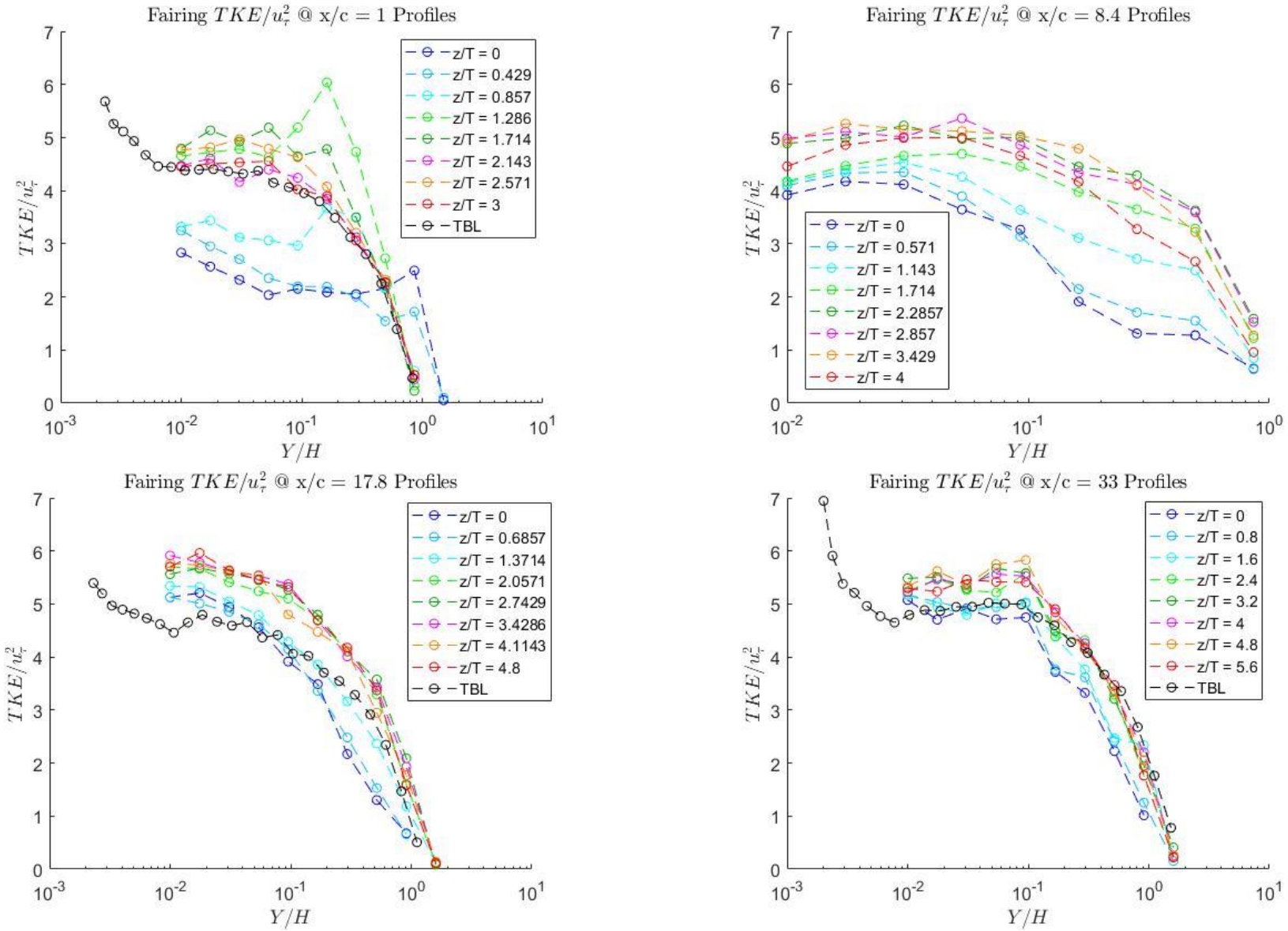

Figure A.F.16: Fairing turbulent kinetic energy profiles normalized by u_τ at (a) X/C = 1 (b) X/C = 8.4 (c) X/C = 17.8 (d) X/C = 33.0 at spanwise locations z/T and undisturbed turbulent boundary layer (TBL)

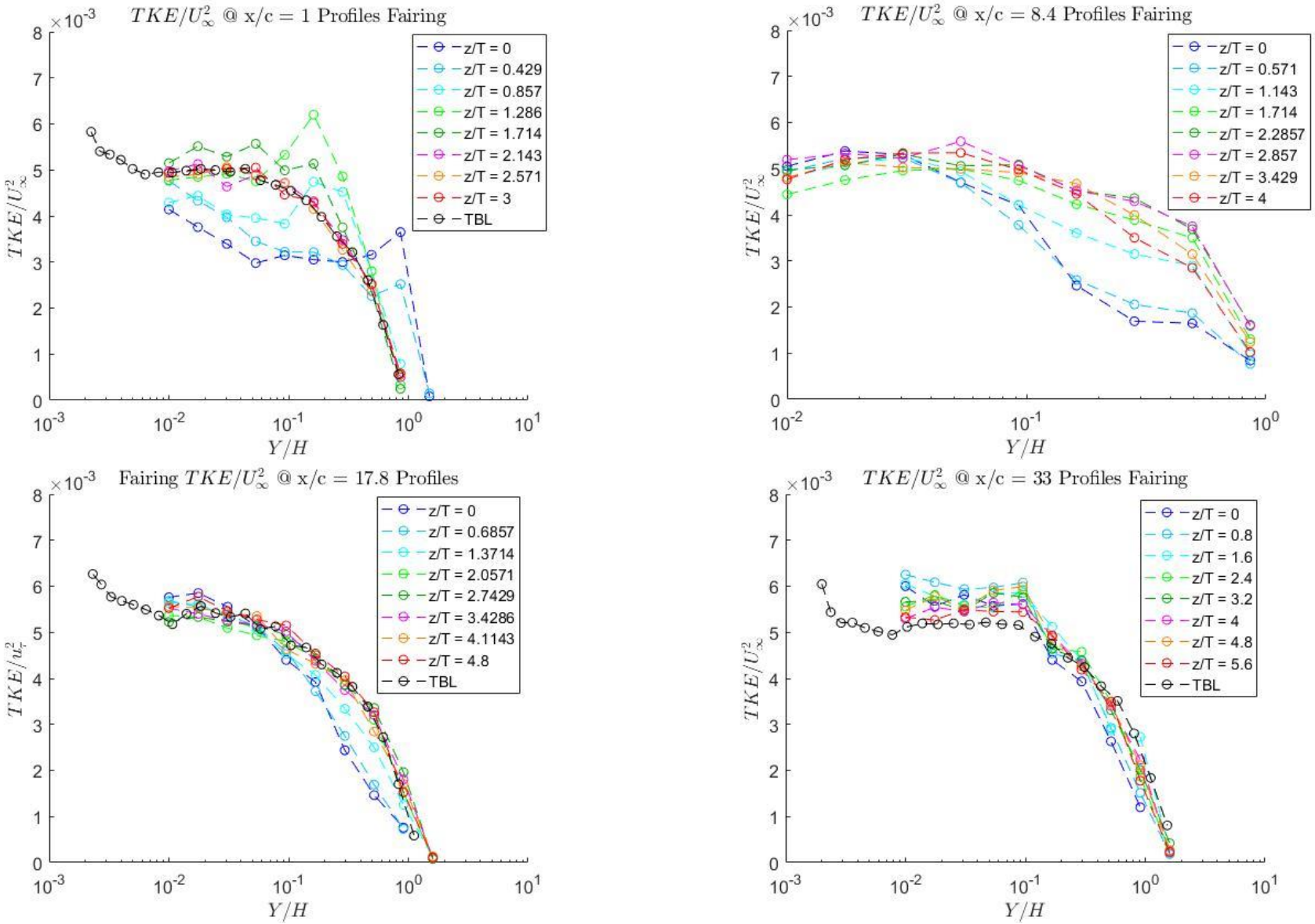

Figure A.F.17: Fairing turbulent kinetic energy profiles normalized by U_∞ at (a) X/C = 1 (b) X/C = 8.4 (c) X/C = 17.8 (d) X/C = 33.0 at spanwise locations z/T and undisturbed turbulent boundary layer (TBL)

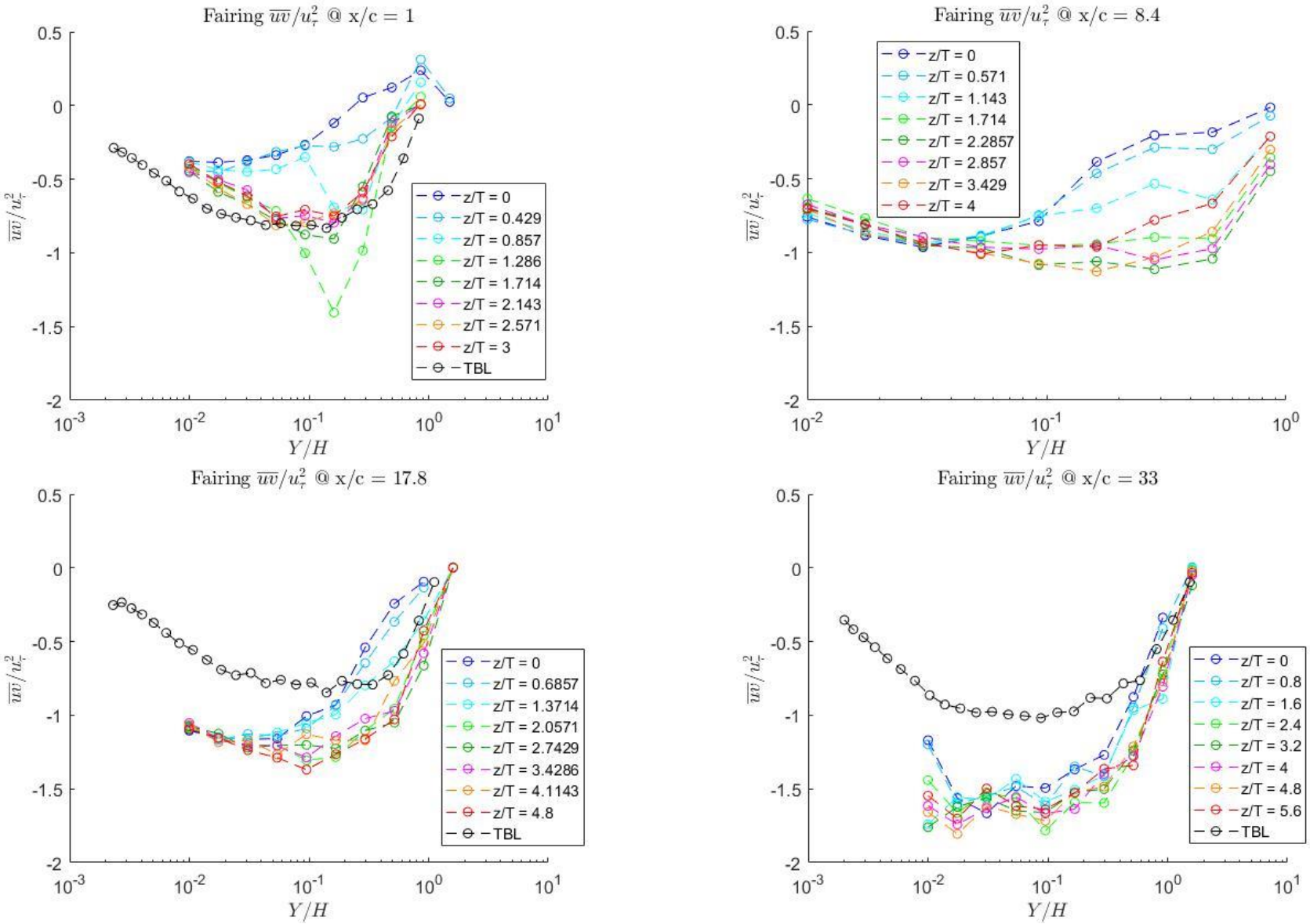

Figure A.F.18: Fairing Reynolds Stress $\overline{uv}$ normalized by u_τ at (a) X/C = 1 (b) X/C = 8.4 (c) X/C = 17.8 (d) X/C = 33.0 at spanwise locations z/T and undisturbed turbulent boundary layer (TBL)

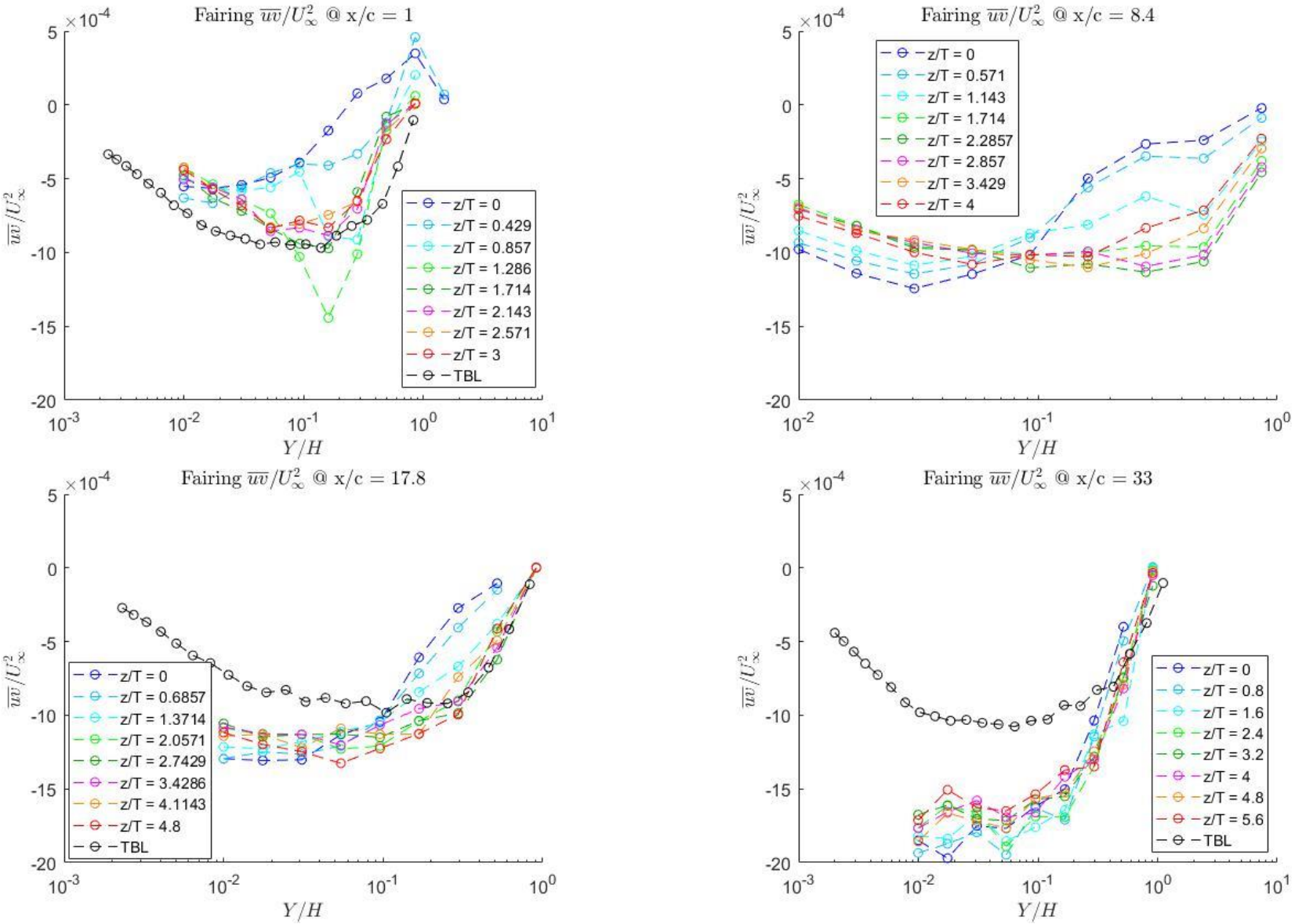

Figure A.F.19: Fairing Reynolds Stress $\overline{uv}$ normalized by U_∞ at (a) X/C = 1 (b) X/C = 8.4 (c) X/C = 17.8 (d) X/C = 33.0 at spanwise locations z/T and undisturbed turbulent boundary layer (TBL)

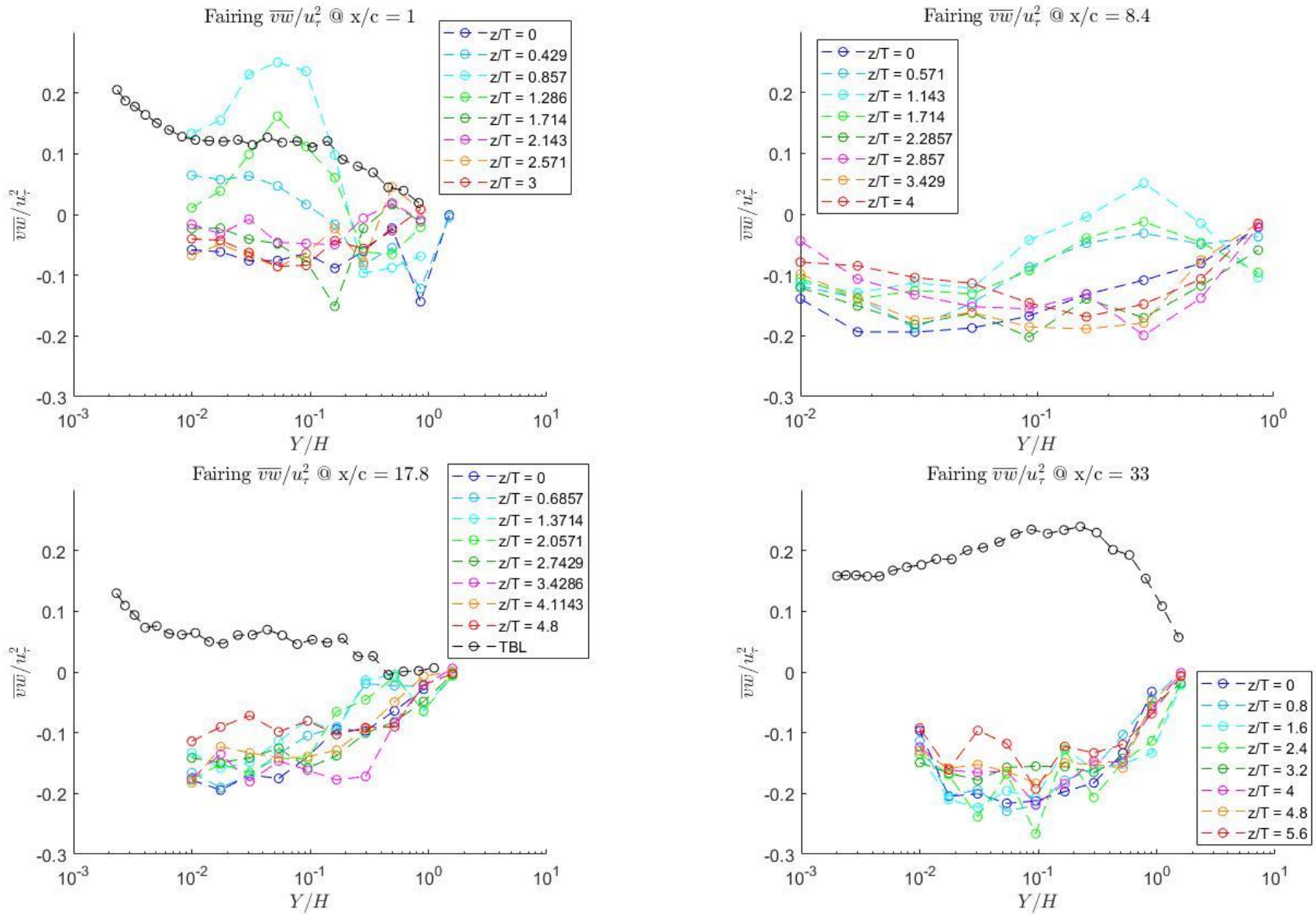

Figure A.F.20: Fairing Reynolds Stress $\overline{vw}$ normalized by u_τ at (a) X/C = 1 (b) X/C = 8.4 (c) X/C = 17.8 (d) X/C = 33.0 at spanwise locations z/T and undisturbed turbulent boundary layer (TBL)

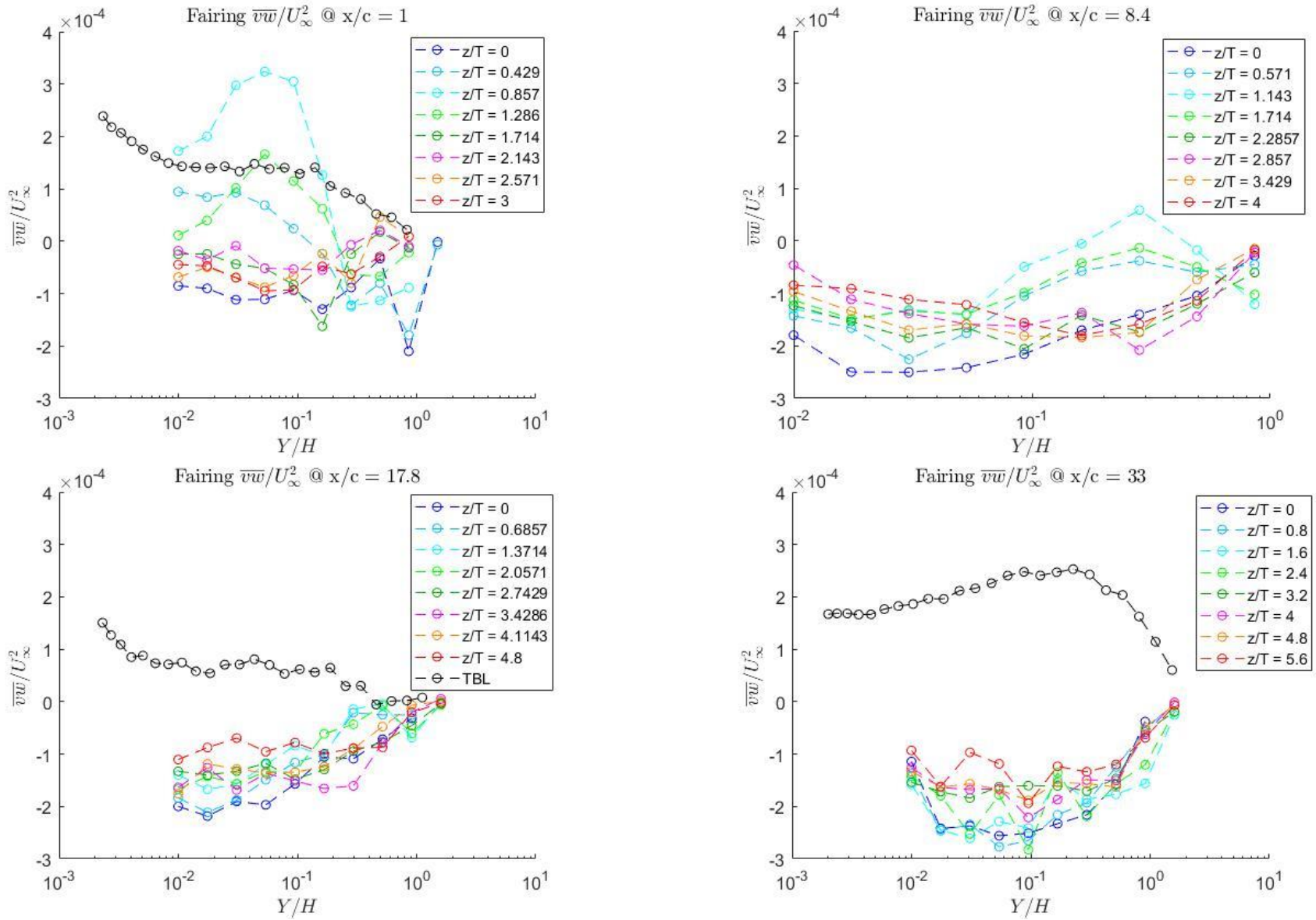

Figure A.F.21: Fairing Reynolds Stress $\overline{vw}$ normalized by U_∞ at (a) X/C = 1 (b) X/C = 8.4 (c) X/C = 17.8 (d) X/C = 33.0 at spanwise locations z/T and undisturbed turbulent boundary layer (TBL)

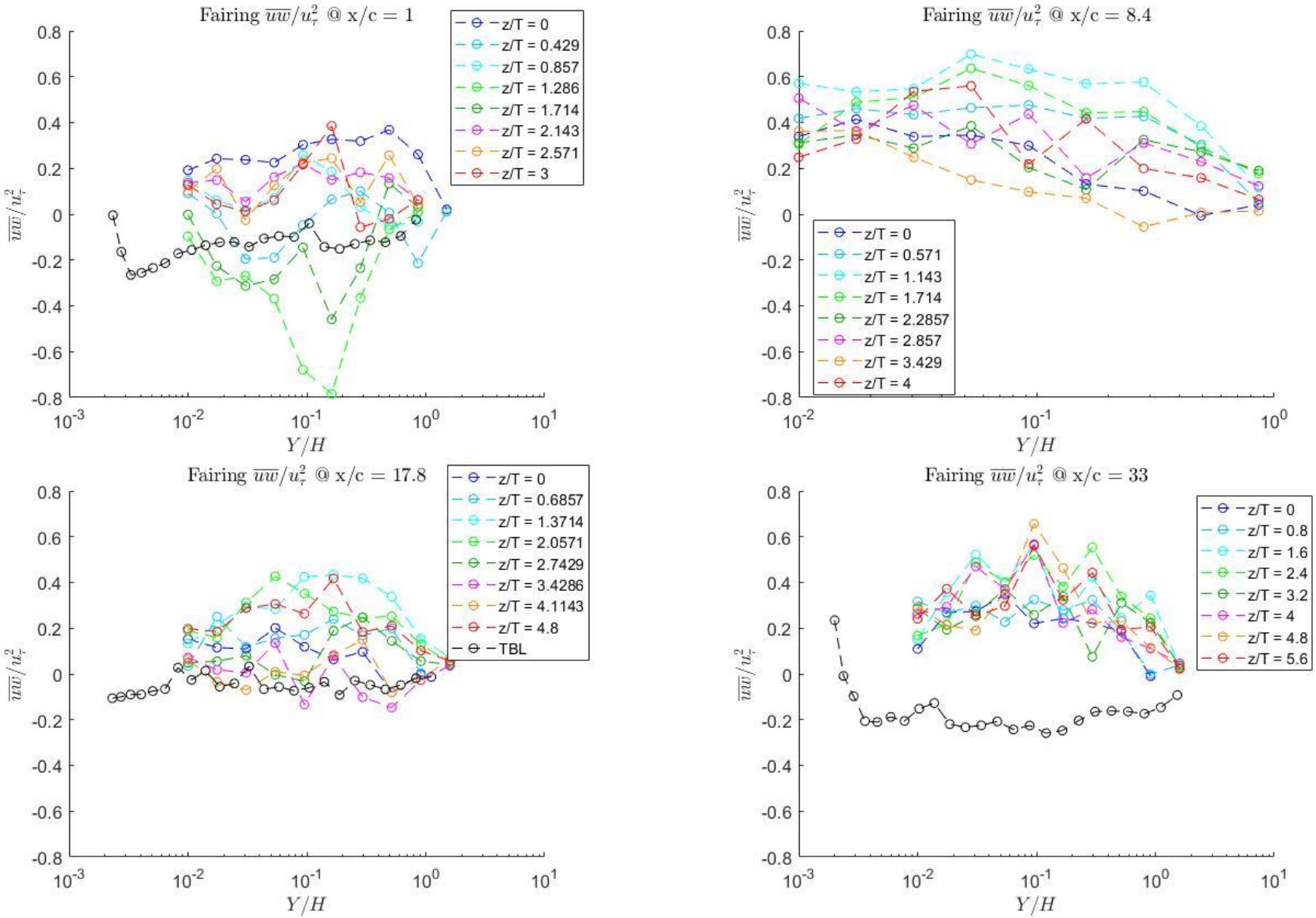

Figure A.F.22: Fairing Reynolds Stress $\overline{uw}$ normalized by u_τ at (a) X/C = 1 (b) X/C = 8.4 (c) X/C = 17.8 (d) X/C = 33.0 at spanwise locations z/T and undisturbed turbulent boundary layer (TBL)

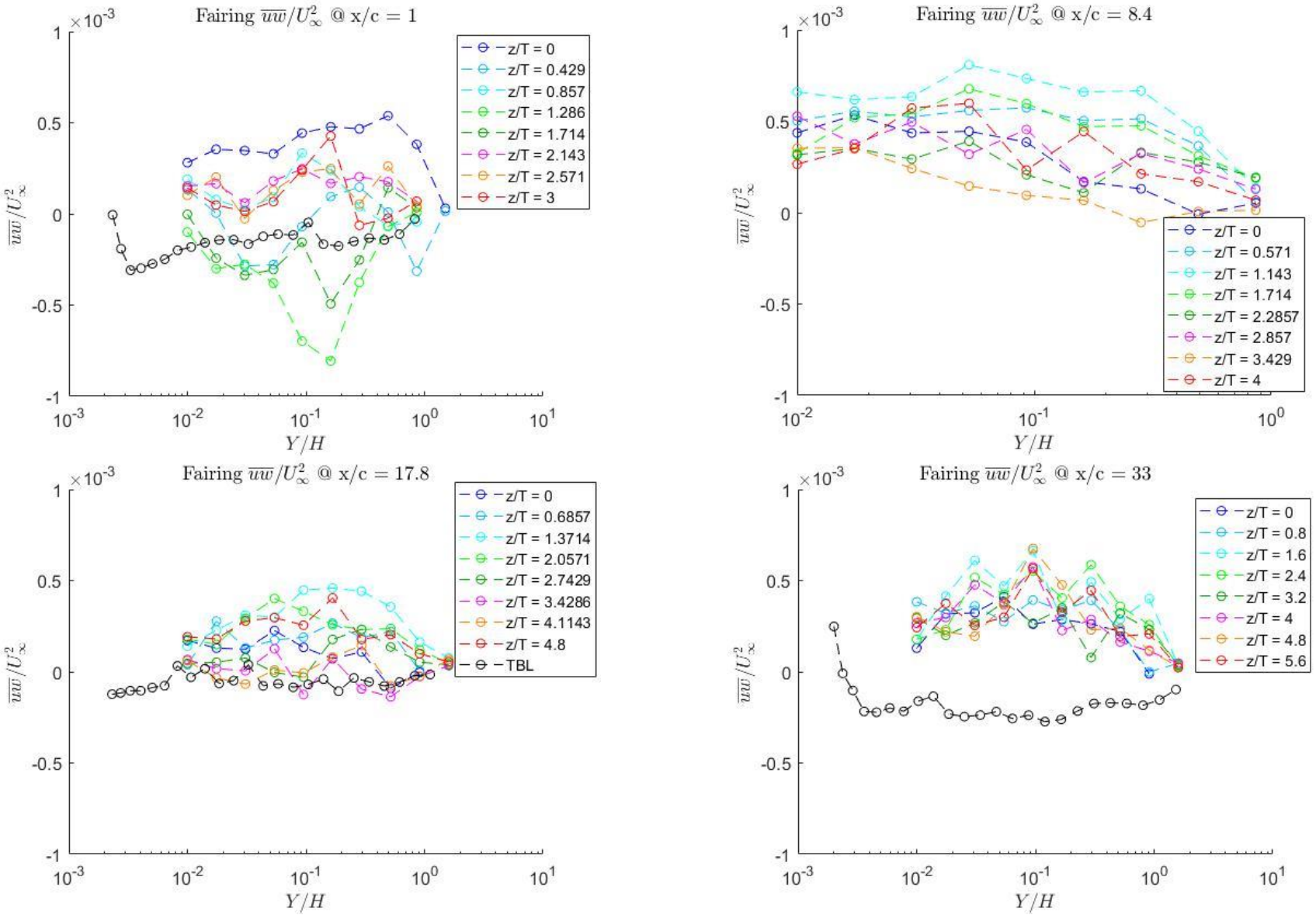

Figure A.F.23: Fairing Reynolds Stress $\overline{uw}$ normalized by U_∞ at (a) X/C = 1 (b) X/C = 8.4 (c) X/C = 17.8 (d) X/C = 33.0 at spanwise locations z/T and undisturbed turbulent boundary layer (TBL)

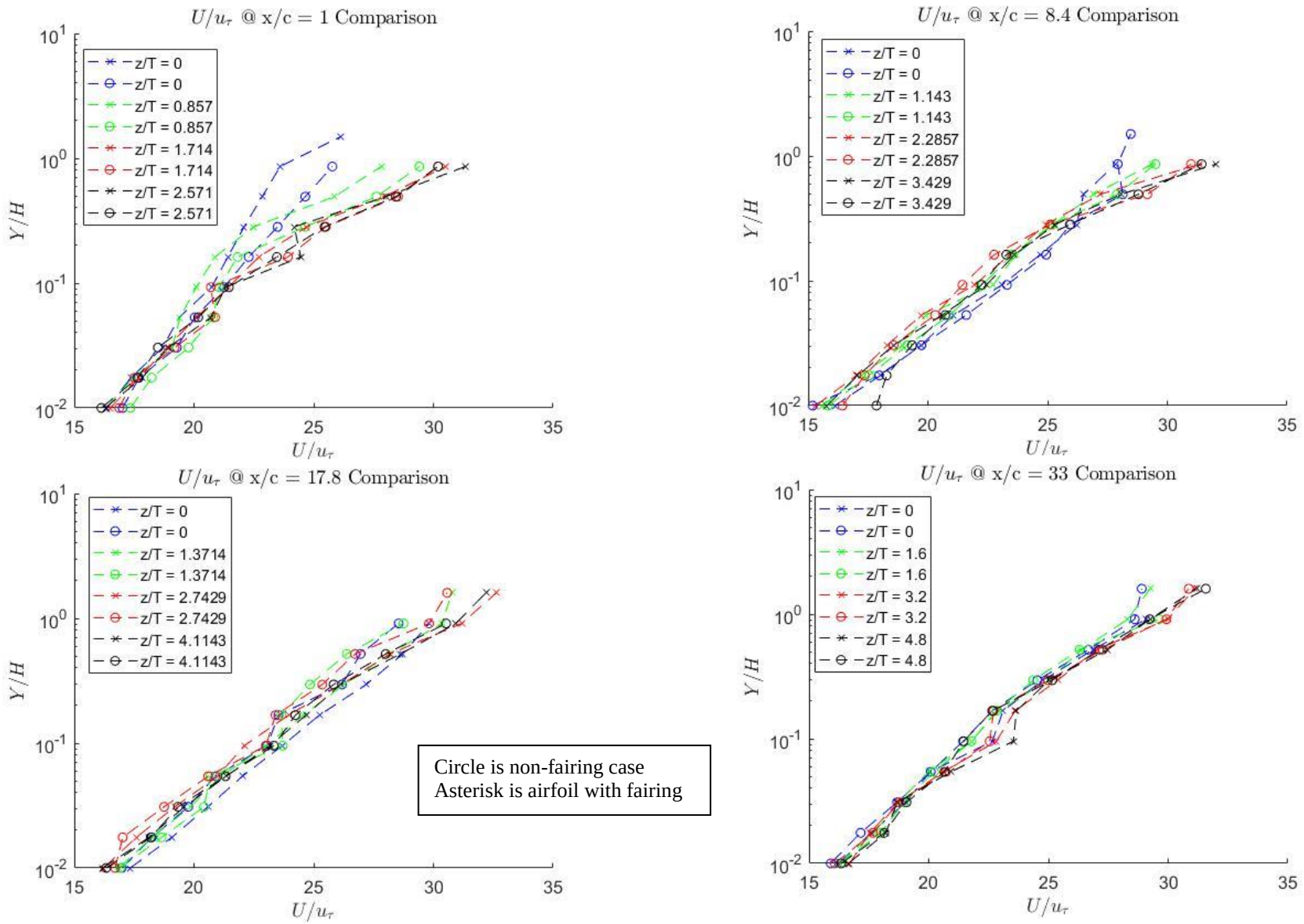

Figure A.C.1: Fairing and non-fairing streamwise mean velocity comparison for odd spanwise locations at (a) X/C = 1 (b) X/C = 8.4 (c) X/C = 17.8 (d) X/C = 33.0

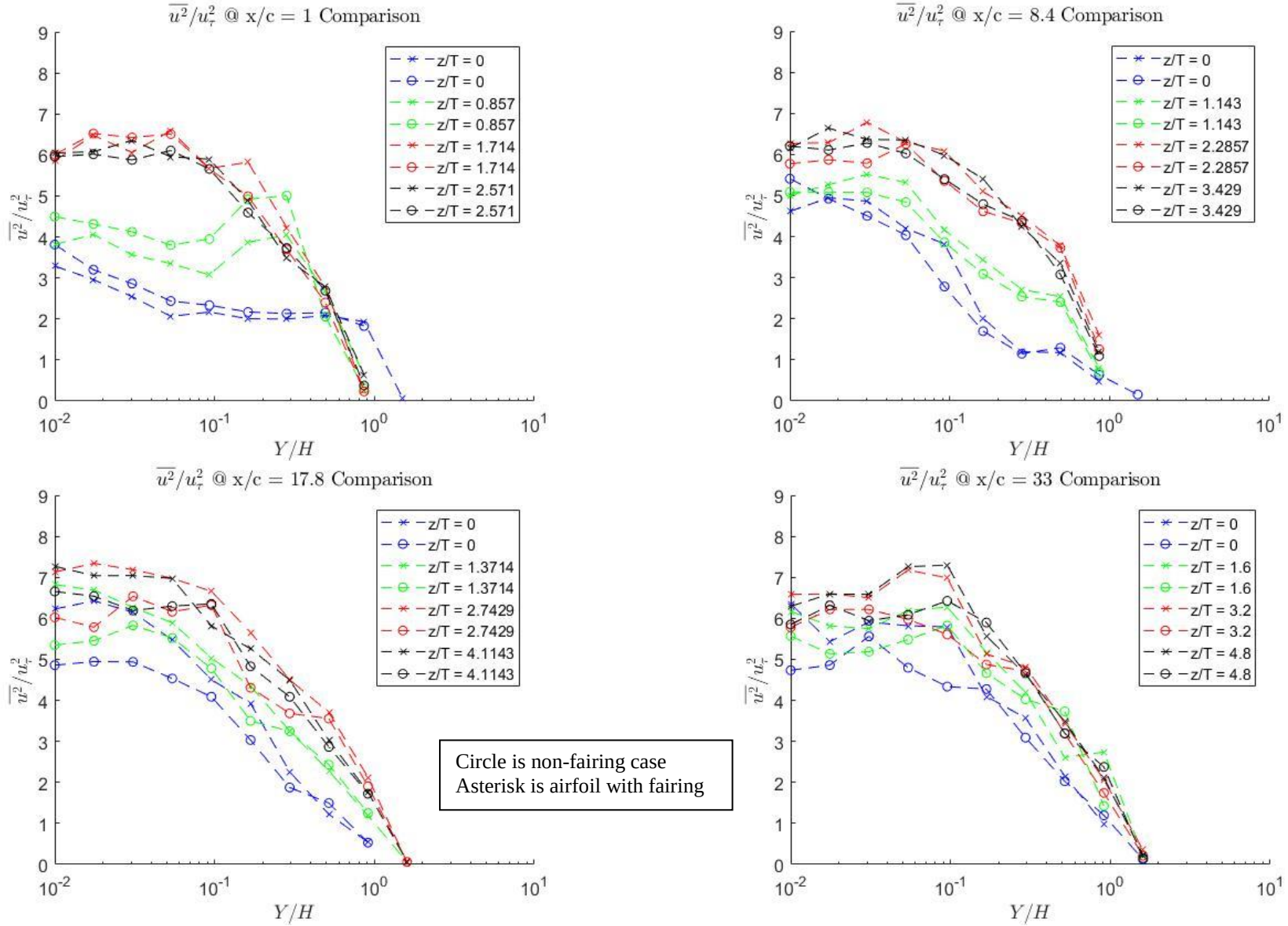

Figure A.C.2: Fairing and non-fairing streamwise velocity variance comparison for odd spanwise locations at (a) X/C = 1 (b) X/C = 8.4 (c) X/C = 17.8 (d) X/C = 33.0

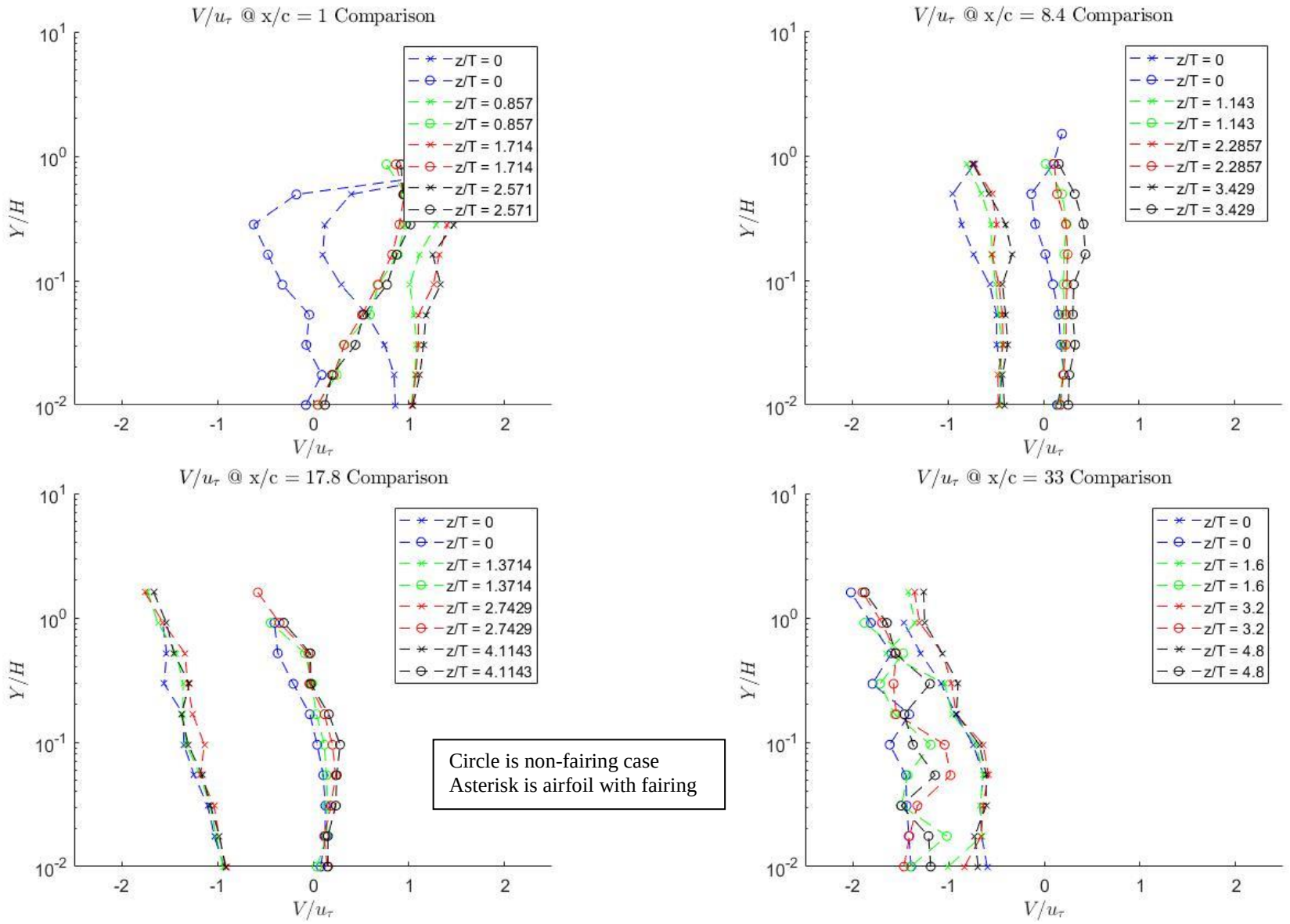

Figure A.C.3: Fairing and non-fairing wall-normal velocity comparison for odd spanwise locations at (a) X/C = 1 (b) X/C = 8.4 (c) X/C = 17.8 (d) X/C = 33.0

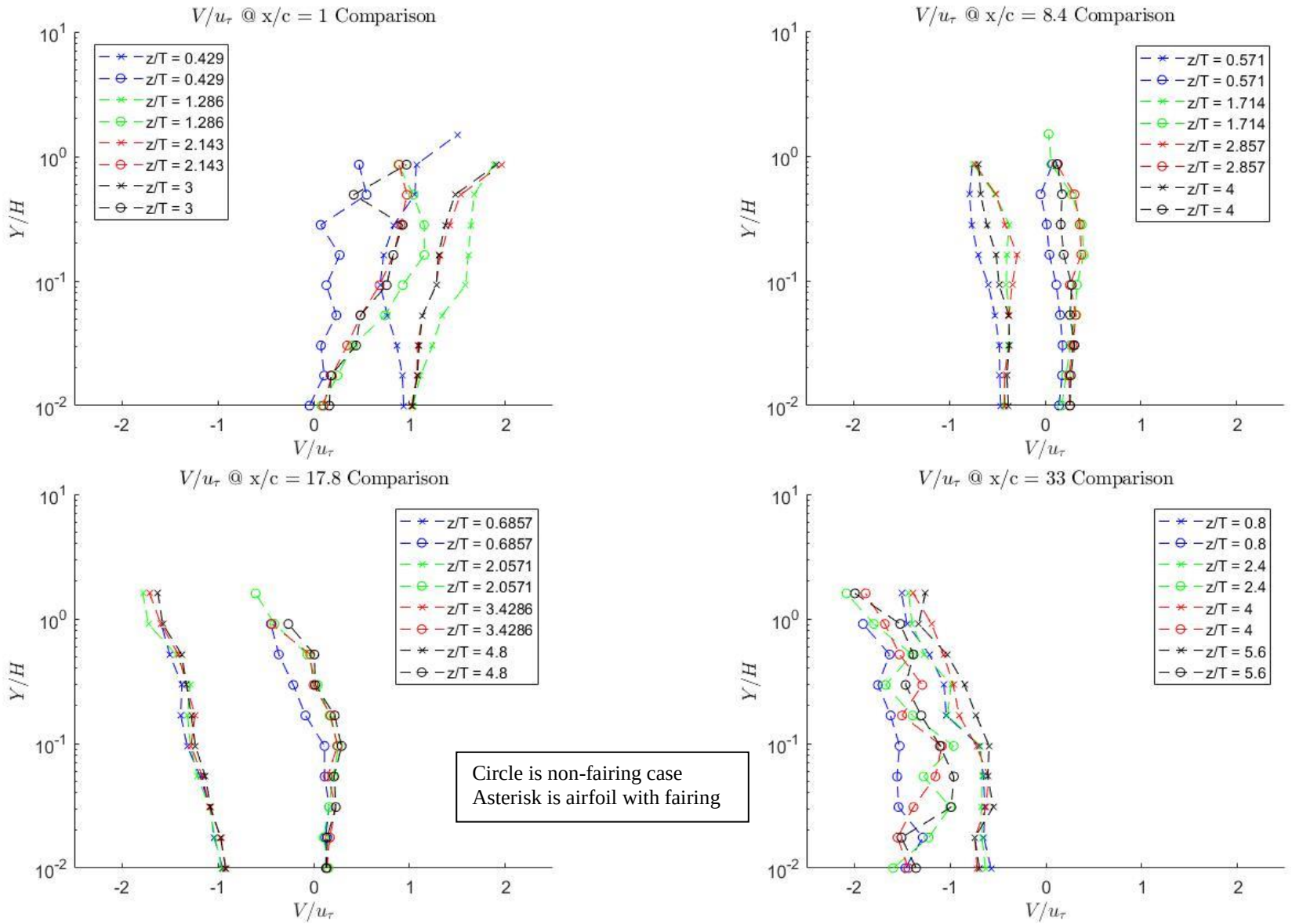

Figure A.C.4: Fairing and non-fairing wall-normal velocity comparison for even spanwise locations at (a) X/C = 1 (b) X/C = 8.4 (c) X/C = 17.8 (d) X/C = 33.0

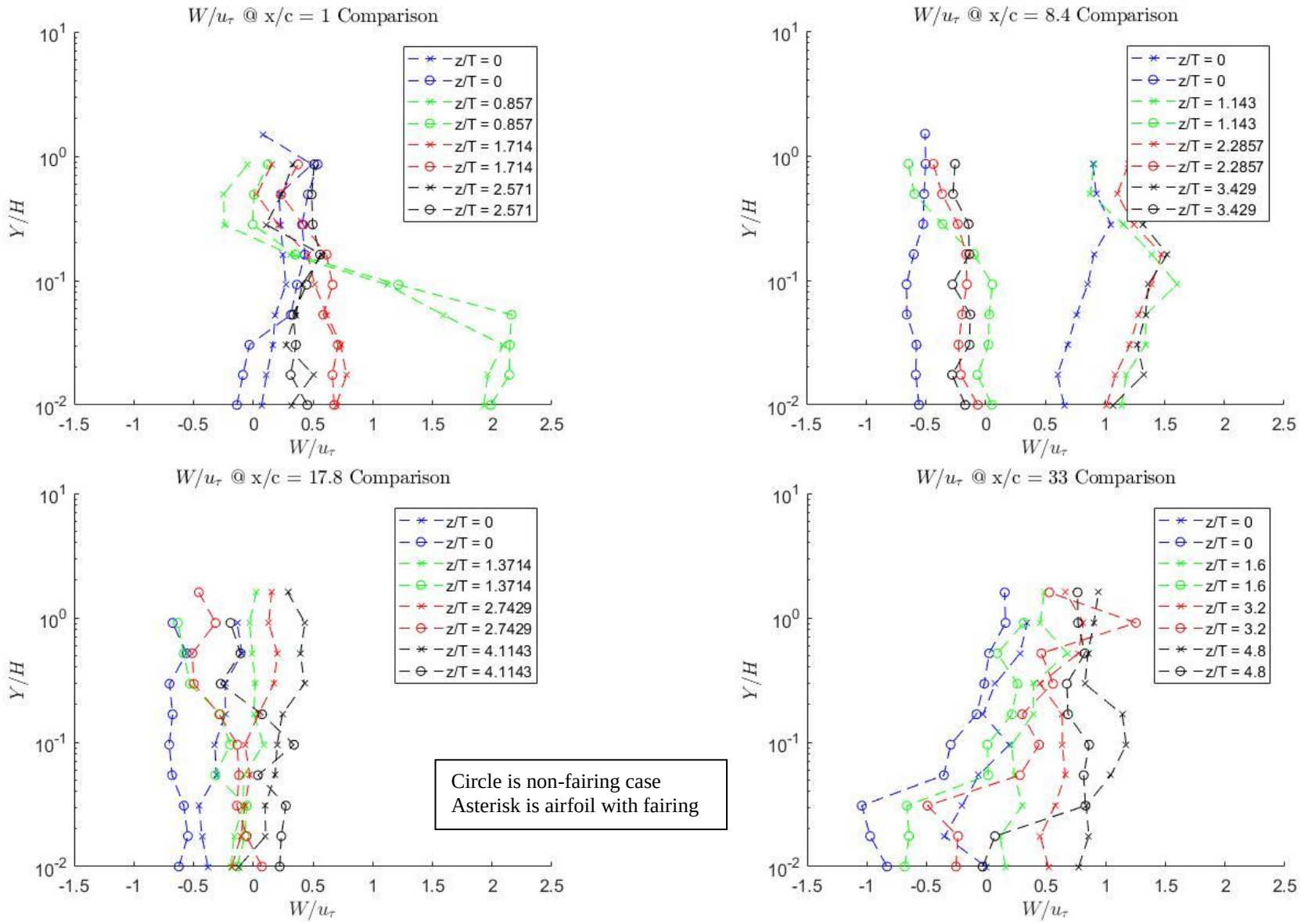

Figure A.C.5: Fairing and non-fairing spanwise velocity comparison for odd spanwise locations at (a) X/C = 1 (b) X/C = 8.4 (c) X/C = 17.8 (d) X/C = 33.0

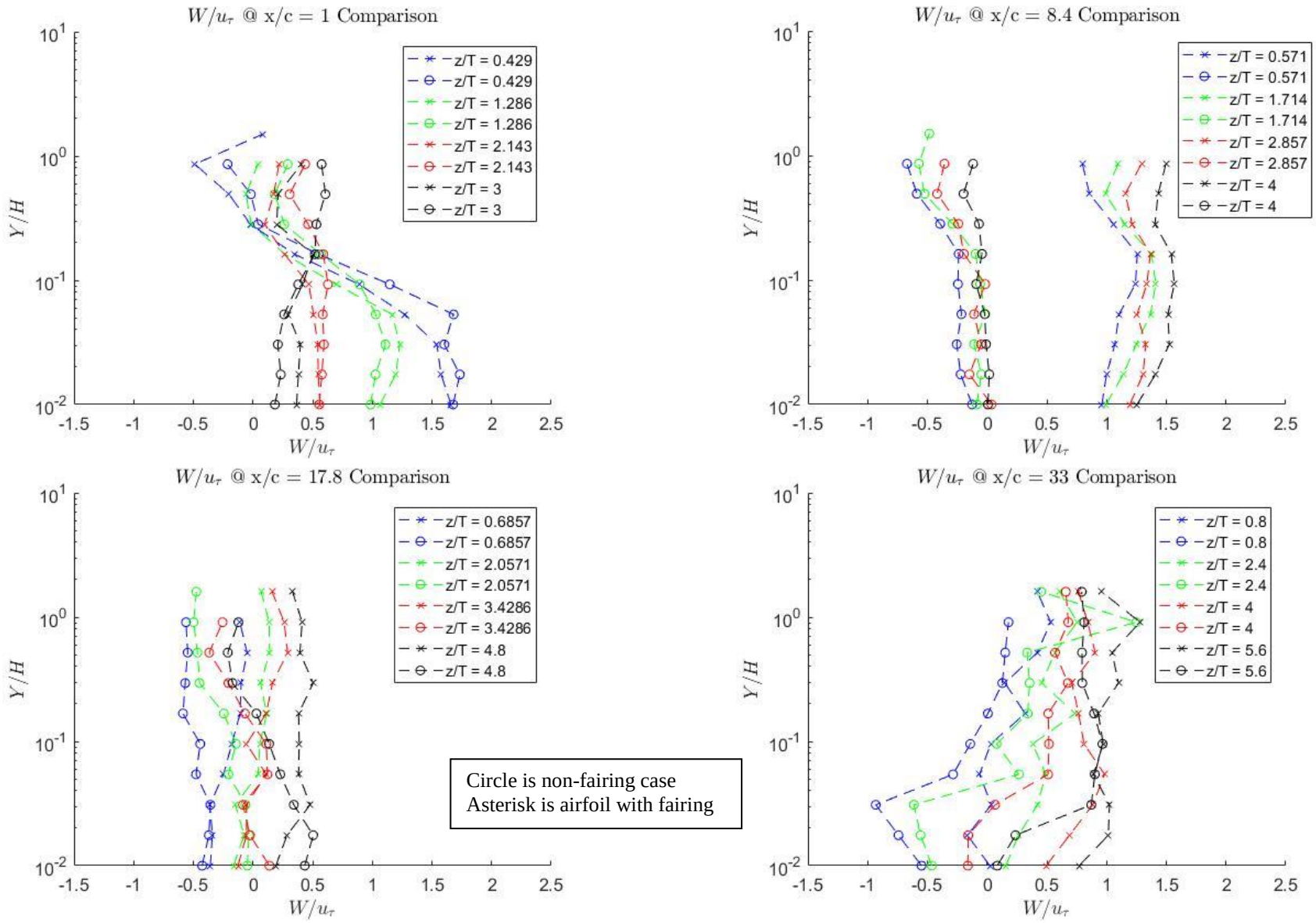

Figure A.C.6: Fairing and non-fairing spanwise velocity comparison for even spanwise locations at (a) X/C = 1 (b) X/C = 8.4 (c) X/C = 17.8 (d) X/C = 33.0

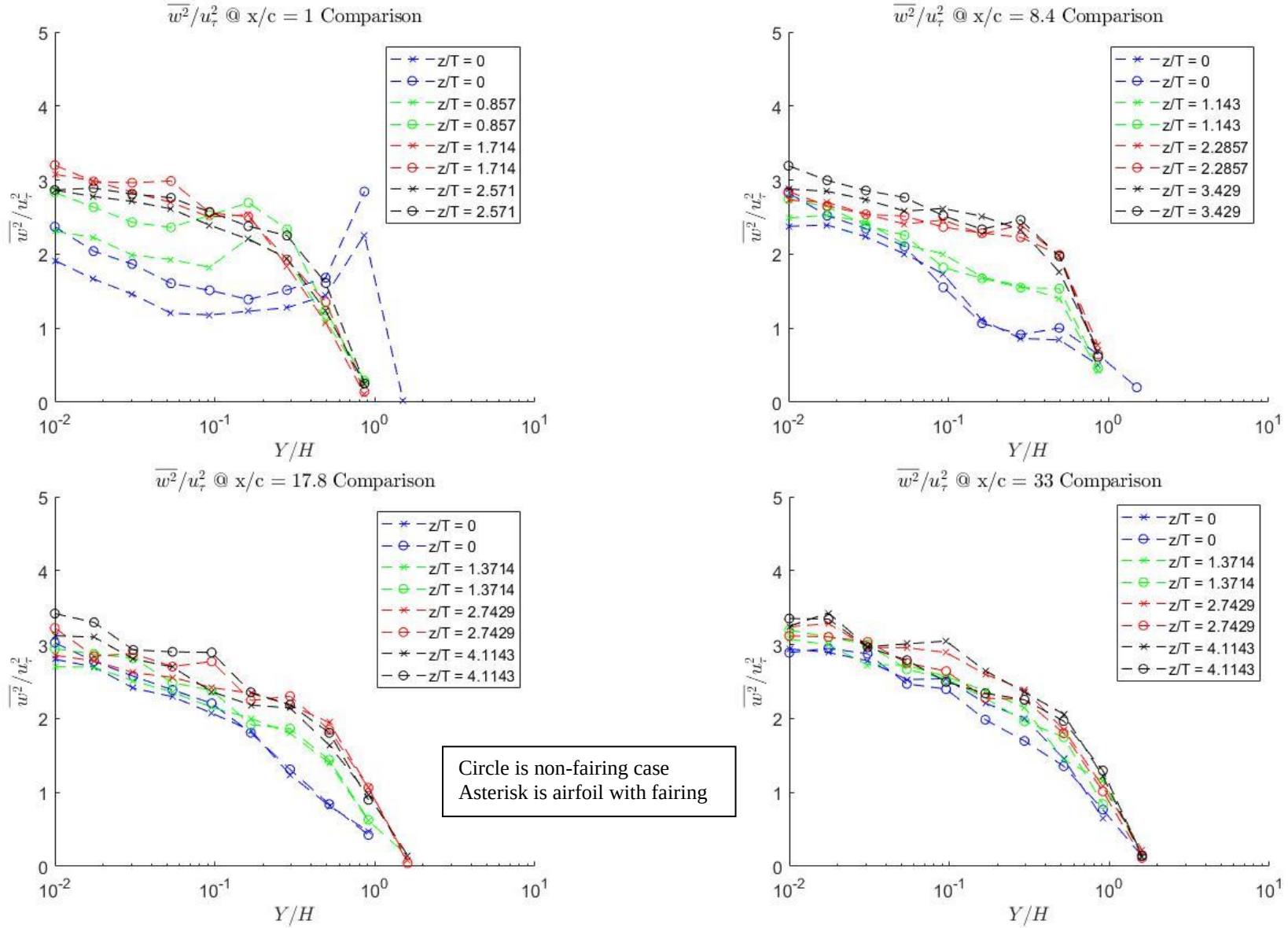

Figure A.C.7: Fairing and non-fairing spanwise velocity variance comparison for odd spanwise locations at (a) X/C = 1 (b) X/C = 8.4 (c) X/C = 17.8 (d) X/C = 33.0

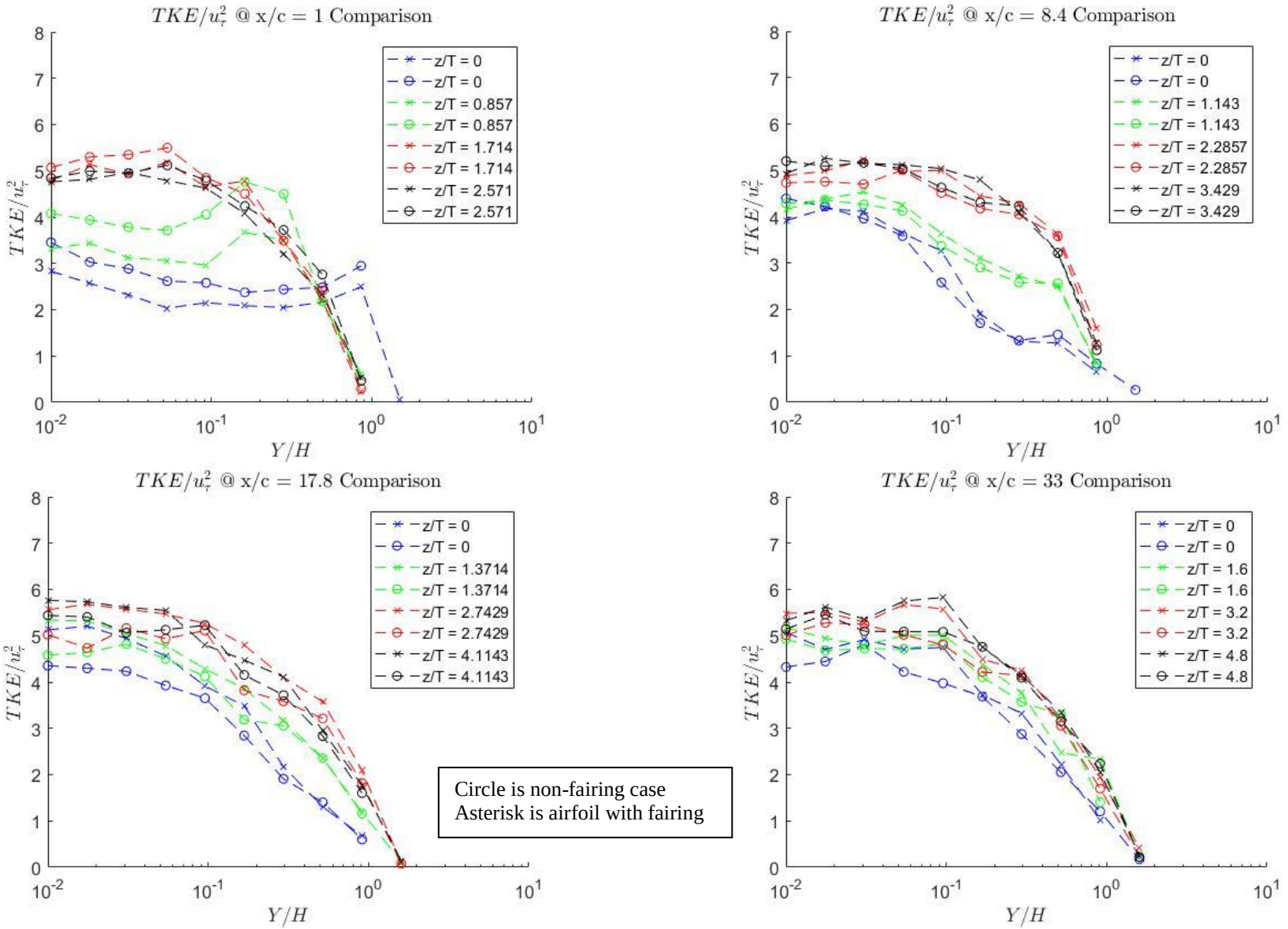

Figure A.C.8: Fairing and non-fairing turbulent kinetic energy comparison for odd spanwise locations at (a) X/C = 1 (b) X/C = 8.4 (c) X/C = 17.8 (d) X/C = 33.0

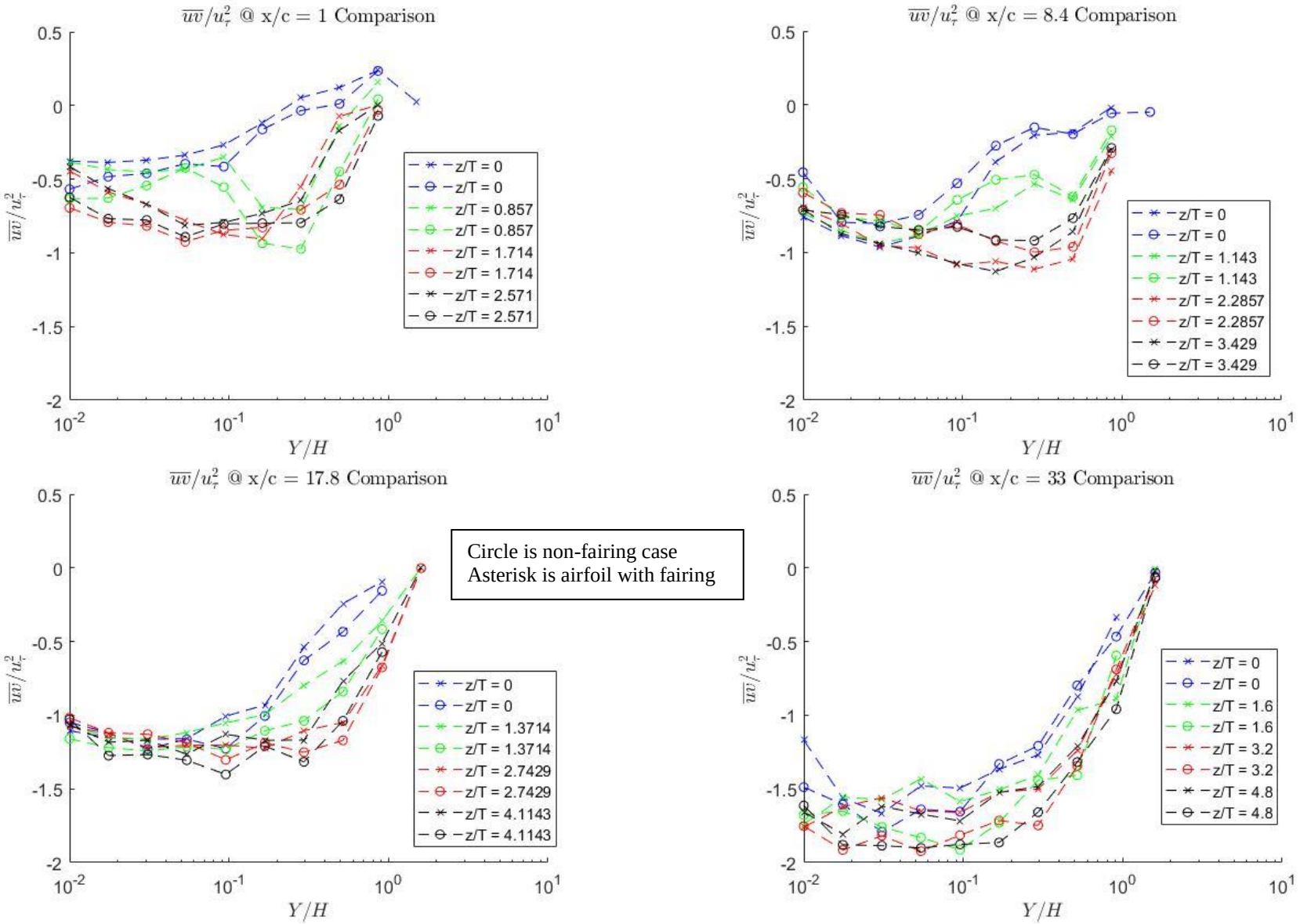

Figure A.C.9: Fairing and non-fairing Reynolds stress $\overline{uv}$ comparison for odd spanwise locations at (a) X/C = 1 (b) X/C = 8.4 (c) X/C = 17.8 (d) X/C = 33.0

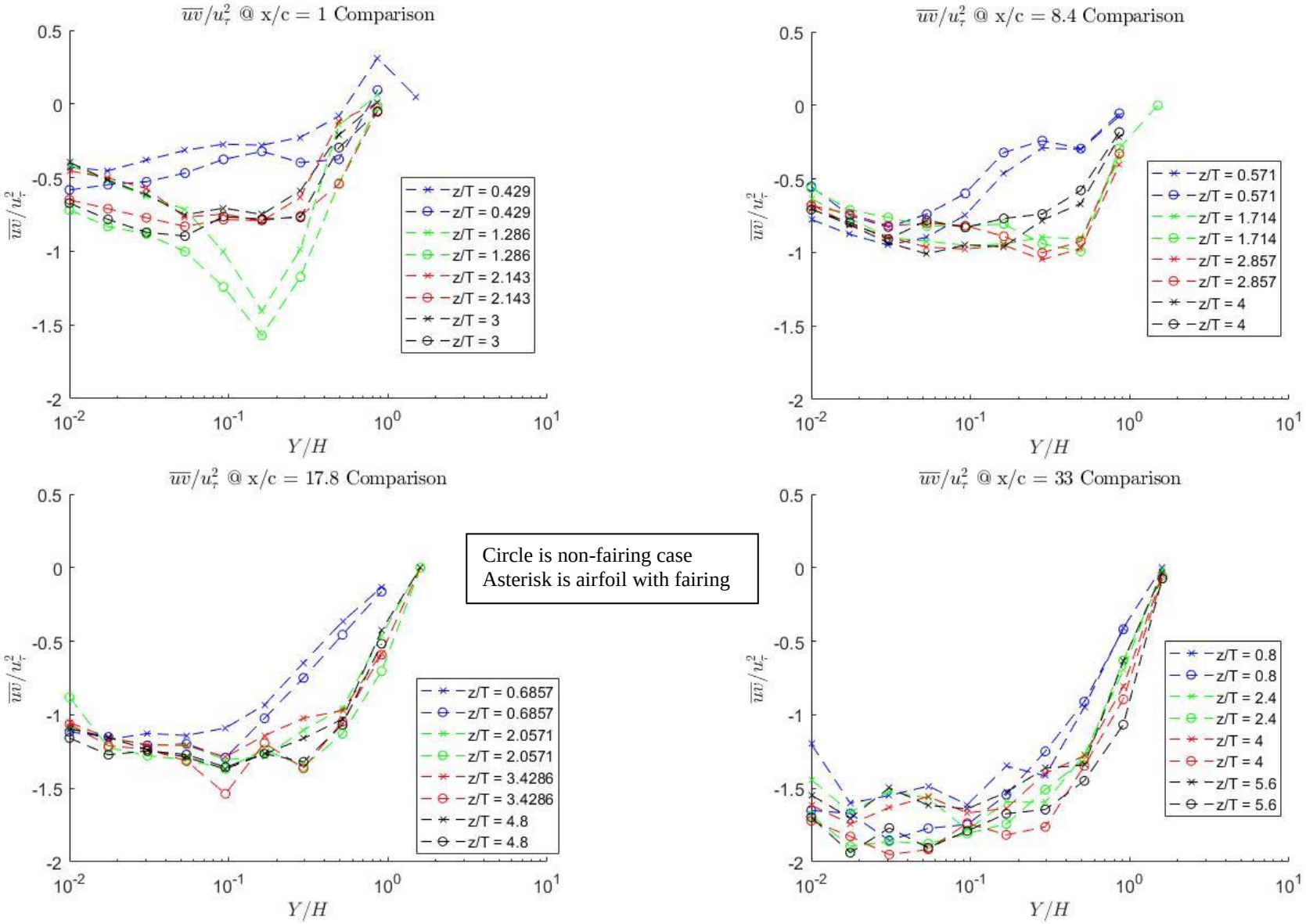

Figure A.C.10: Fairing and non-fairing Reynolds stress $\overline{uv}$ comparison for even spanwise locations at (a) X/C = 1 (b) X/C = 8.4 (c) X/C = 17.8 (d) X/C = 33.0

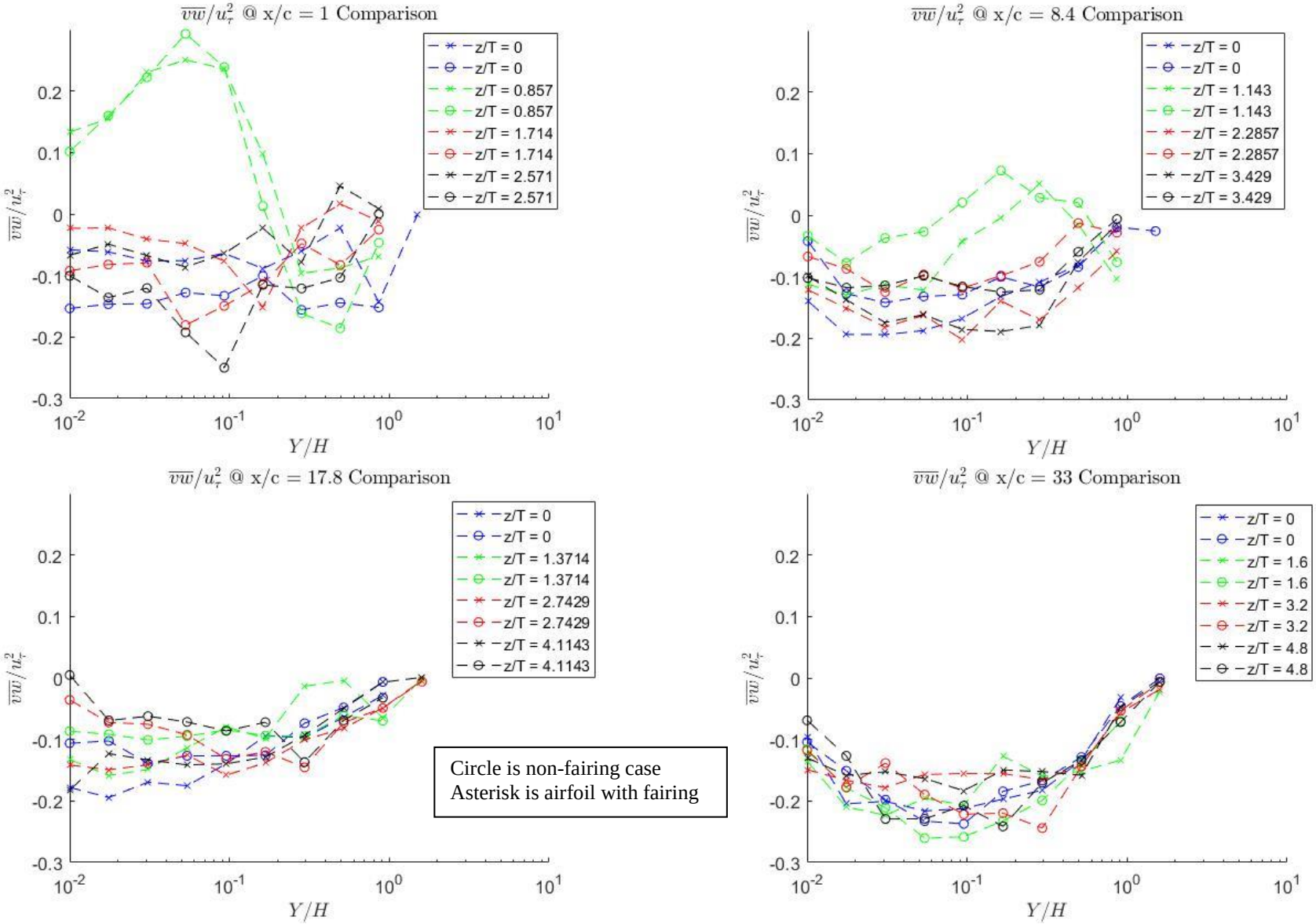

Figure A.C.11: Fairing and non-fairing Reynolds stress $\overline{vw}$ comparison for odd spanwise locations at (a) X/C = 1 (b) X/C = 8.4 (c) X/C = 17.8 (d) X/C = 33.0

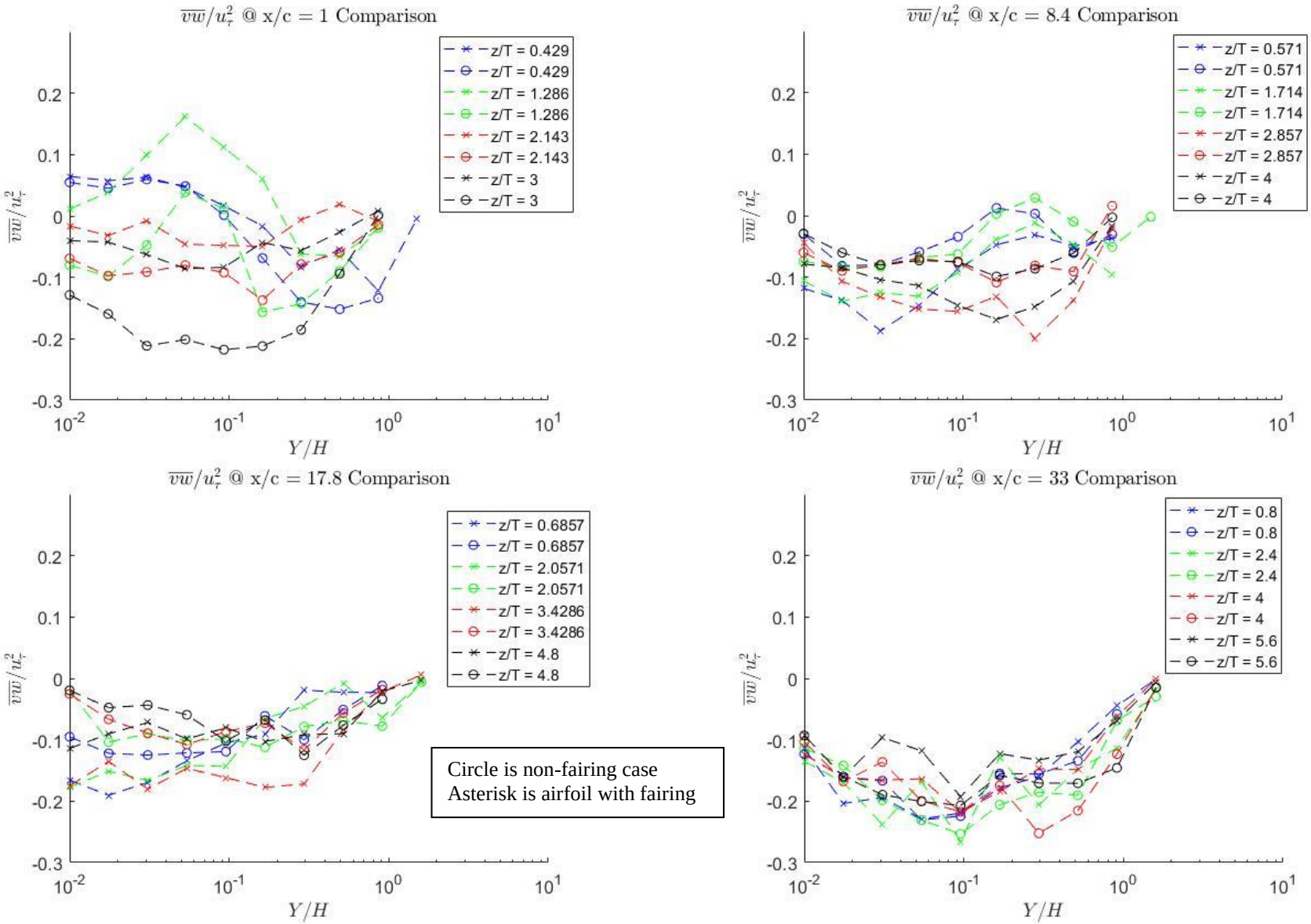

Figure A.C.12: Fairing and non-fairing Reynolds stress $\overline{vw}$ comparison for even spanwise locations at (a) X/C = 1 (b) X/C = 8.4 (c) X/C = 17.8 (d) X/C = 33.0

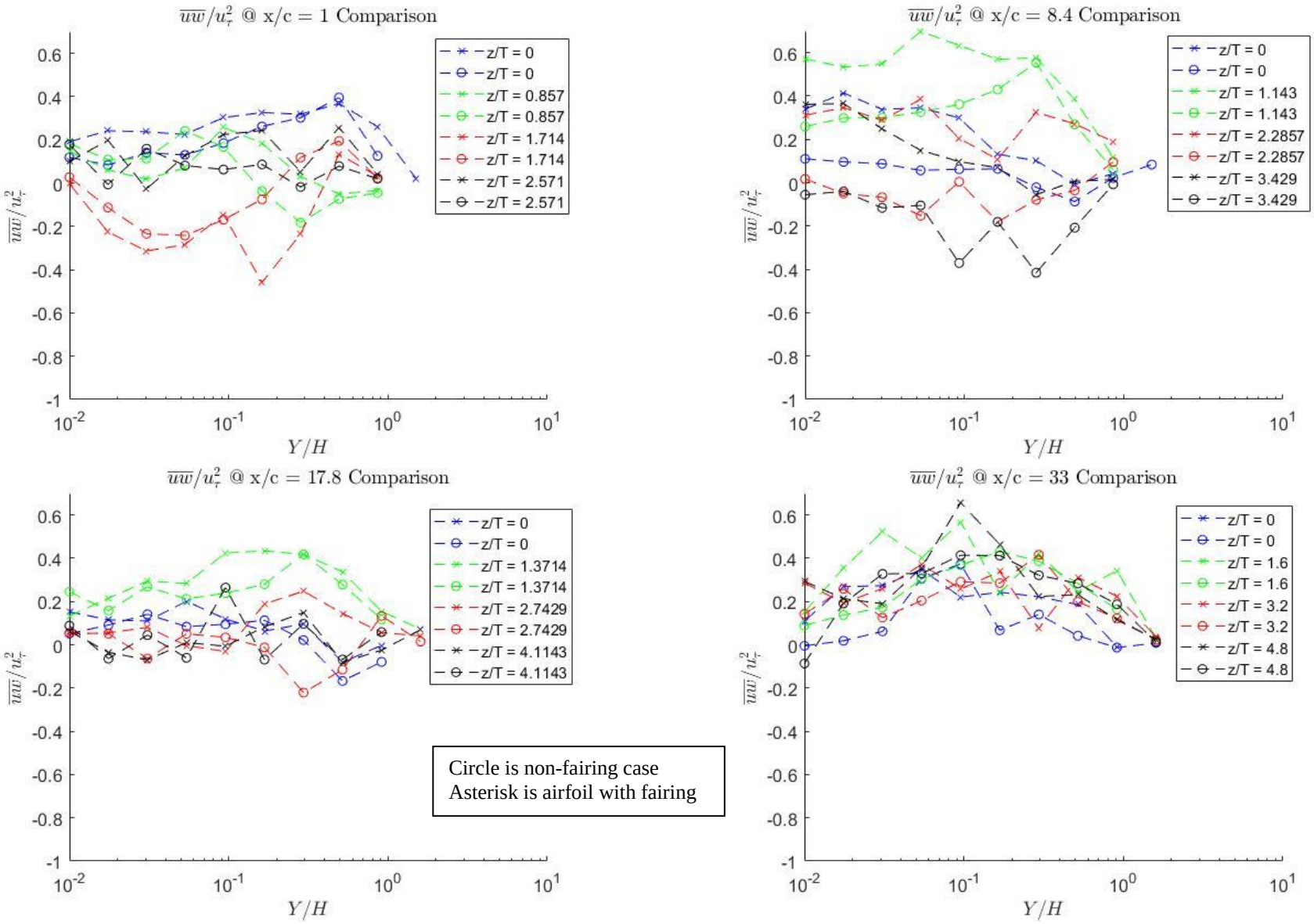

Figure A.C.13: Fairing and non-fairing Reynolds stress $\overline{uw}$ comparison for odd spanwise locations at (a) X/C = 1 (b) X/C = 8.4 (c) X/C = 17.8 (d) X/C = 33.0

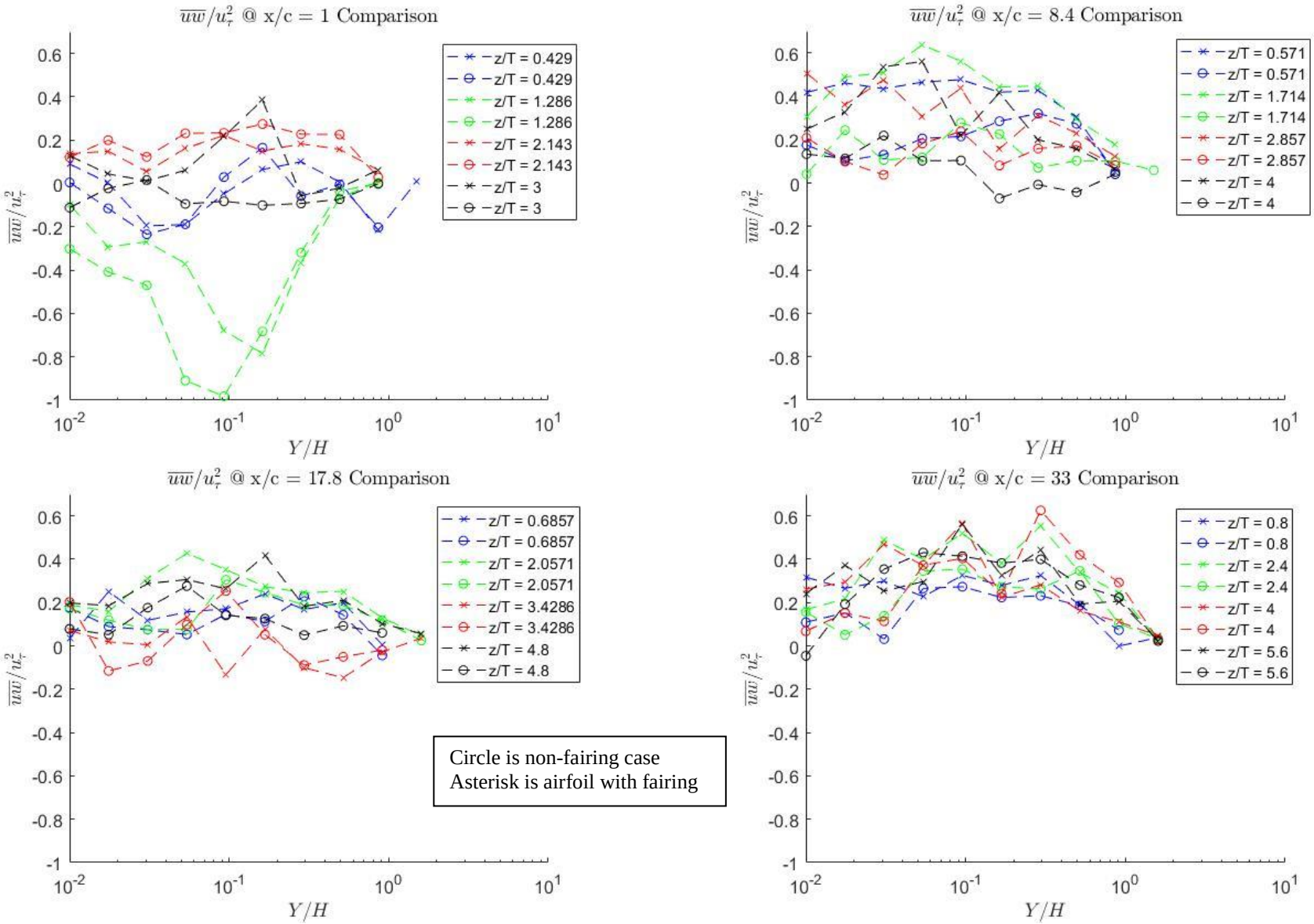

Figure A.C.14: Fairing and non-fairing Reynolds stress $\overline{uw}$ comparison for even spanwise locations at (a) X/C = 1 (b) X/C = 8.4 (c) X/C = 17.8 (d) X/C = 33.0

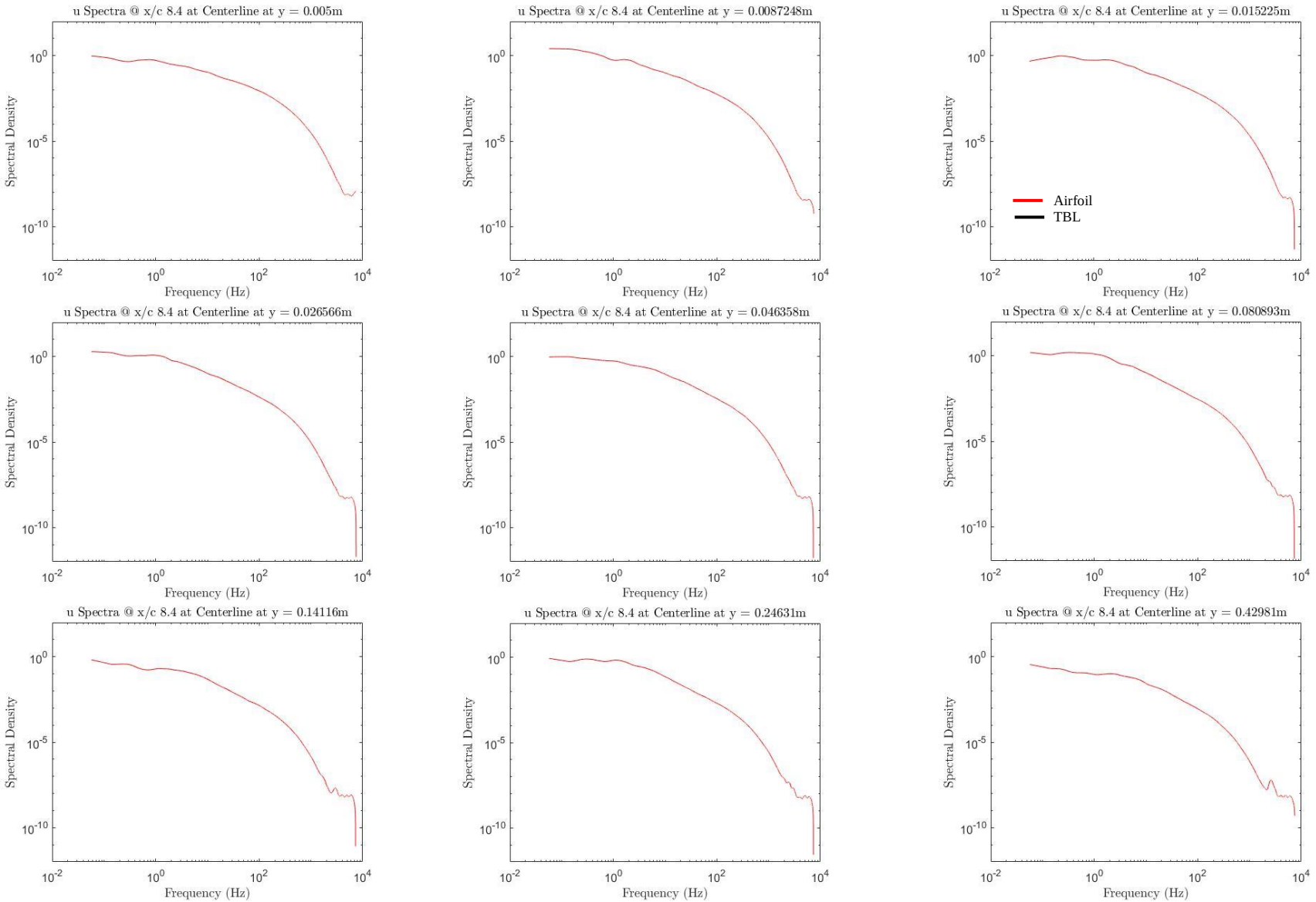

Figure A.S.1: Streamwise Velocity Spectra Normalized H/u_τ^3 at the Centerline at X/C = 8.4 for airfoil

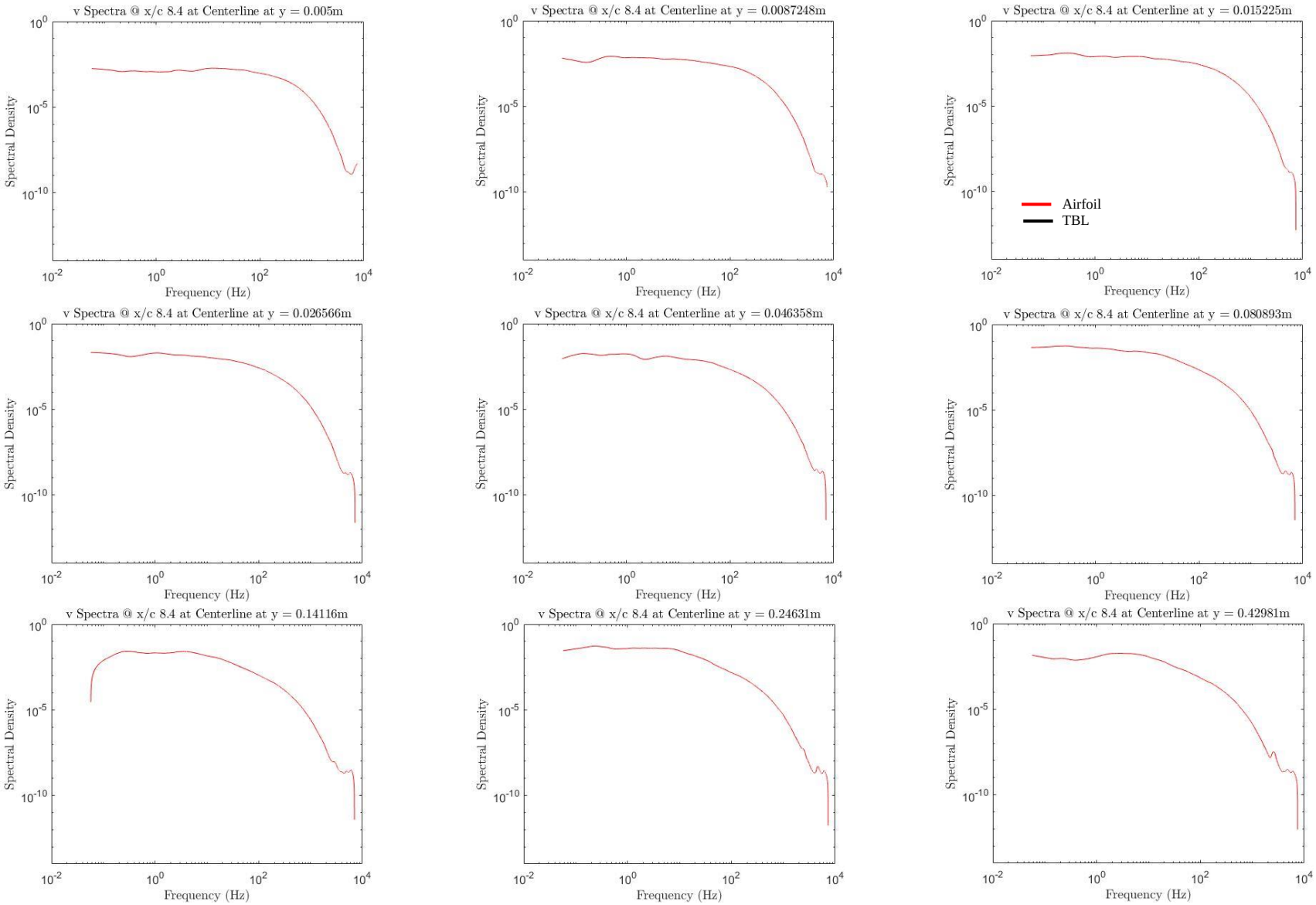

Figure A.S.2: Wall-Normal Velocity Spectra Normalized H/u_τ^3 at the Centerline at X/C = 8.4 for airfoil

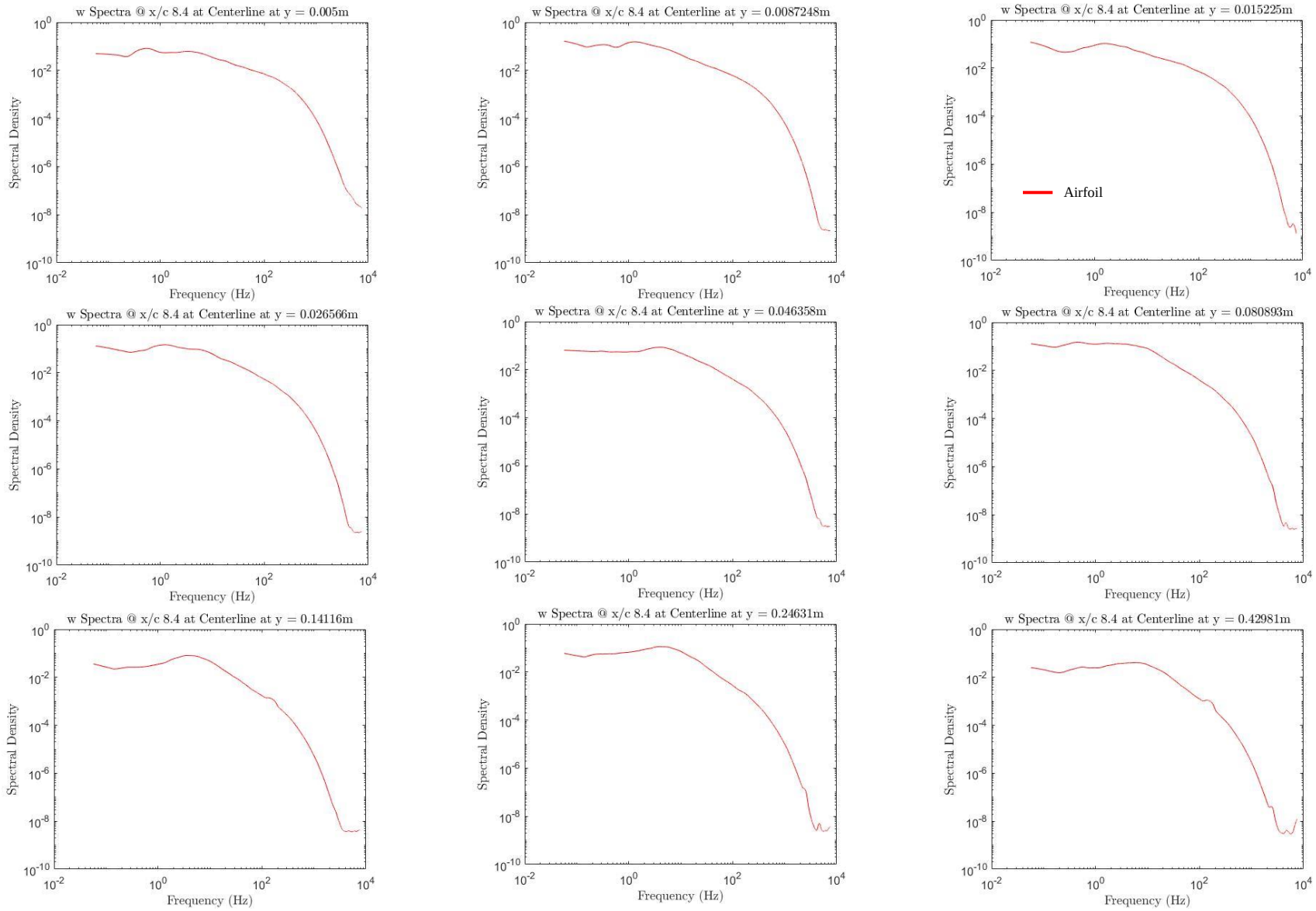

Figure A.S.3: Spanwise Velocity Spectra Normalized H/u_τ^3 at the Centerline at X/C = 8.4 for airfoil